Challenges Hindering Small Molecule Detection with Floating Gate Transistor Biosensors

A Dissertation

SUBMITTED TO THE FACULTY OF

THE UNIVERSITY OF MINNESOTA

BY

Demetra Zackie Adrahtas

IN PARTIAL FULFILLMENT OF THE REQUIREMENTS

FOR THE DEGREE OF

DOCTOR OF PHILISOPHY

Advisers: Prof. Kevin D. Dorfman & Prof. C. Daniel Frisbie

August 2023

Acknowledgements

There are many people that have driven my growth into the scientist and engineer I am now. I'd like to start with thanking my advisers, Prof. Daniel Frisbie and Prof. Kevin Dorfman, for their support and advising throughout my PhD. Another thank you to Prof. Christy Haynes who acted as a third advisor for the latter half of my PhD. Thank you to my mentors, Dr. Mathew Thomas, Dr. Jiayi He, and Dr. Fazel Zare Bidoky, who trained me and offered additional advising during the early stages of the projects involving the floating gate transistor. Thank you to Dr. Yan Wang, Dr. Krystopher Jochem, Dr. Quyen Nguyen, Dr. Zuoti Xie, Dr. Abel Demissie, Dr. Scott White, Dr. Motao Cao, Jonathon Nguyen, and Amber Walton for discussions on approaching new experiments, instrument training and troubleshooting, and encouragement throughout my various projects. Thank you to Clare Froehlich for collaborating with me on the FGT sensor projects, particularly measuring the binding affinity of the capture agents. Thank you to Dr. Ming Tzia-Onn and Dr. Kyrungryul Oh for collaboration on our ion gel catalytic condenser work. Thank you Dr. Kyung Gook Cho and Prof. Keun Hyung Lee for collaboration on our polythiophene-based EGT work. Thank you to Dr. Andre Mkhoyan for serving as my faculty mentor and for the thoughtful and encouraging discussions. Thank you to my mentees, Anna Campbell-Sowden and Claire Mihalko, for teaching me how to be a better mentor.

Thank you to the Minnesota Nanofabrication Center (MNC) and Characterization Facility at the University of Minnesota for their resources, the funding that supports them, and their staff members for instrument training and troubleshooting. I acknowledge the gracious funding from the Michael H. Baker Family Foundation, IPRIME at the University of Minnesota, and the NIH

Biotechnology Training Grant. Thank you to my committee members, Prof. Christy Haynes, Prof. Alon McCormick, and Prof. Natalie Boehnke, for their time in assessing my thesis and defense.

Lastly, I am incredibly thankful for the support from my parents, John and Nitsa, and my brothers, Ari and Alex. Thank you to my partner, Keaton Krueger, for your willingness to review and critique my work, for mentally and emotionally supporting me throughout this PhD, and for grounding me.

Abstract

As made evident by the COVID-19 pandemic, biological sensing enables a means of widespread monitoring of an analyte of interest. Here, a simple “yes or no” qualitative biosensor (e.g. Abbott’s BinaxNOW) provided an on-site test for people, lightening the workload and relieving wait times at testing clinics using advanced analytical instruments (e.g. PCR). The floating gate transistor (FGT) was introduced as an electrochemical platform to achieve a similar goal, with the added benefit of a quantitative response for end-use applications where concentrations are meaningful. The FGT biosensor utilizes a low voltage, high amplification signal transducer, the electrolyte-gated transistor (EGT). A floating gate electronically couples the EGT to a sensing medium while maintaining physical separation. This patent-protected technology, invented at the University of Minnesota, has been able to detect large biomolecules, including DNA and proteins.

The first study aims to challenge our understanding of the FGT architecture in order to optimize the design of FGT biosensors for quasi-static sensing. Initially, FGTs were fabricated on both SiO_2/Si and fused silica glass wafers to observe if charge loss experienced by the EGT was a result of parasitic capacitance between the electrodes and the p-type silicon. Our findings suggest no difference in the operation of the two types of FGTs. Alternatively, we rather attribute the perceived charge loss experienced from the sensing medium to the EGT as an uncertainty of specific capacitance values of relevant interfaces. This insight enabled predictive FGT models to be constructed without the consideration of charge loss. Further, measurement conditions were investigated along with the short and long term stability of the EGT.

The second study utilizes the predictive FGT models to design a charge-based FGT sensor for detection of glyphosate with an antibody-functionalized device. As opposed to past work with the FGT sensor, extensive characterization of the surface functionalization was carried out to guarantee antibody conjugation to gold, setting groundwork for future antibody-based devices. The resulting glyphosate FGT biosensor did not have a sufficient response to a high concentration glyphosate dosing compared to the negative controls. This was attributed to Debye length limitations from the electrolyte and perhaps poor binding affinity of the glyphosate antibody.

The third study, in turn, utilizes structure-shifting aptamers for the detection of the small molecule, serotonin. Again, the surface functionalization was characterized to guarantee aptamer immobilization on gold. The serotonin FGT biosensor responded to serotonin down to 2 μM, having dose-dependent responses; however, negative controls revealed nonspecific interactions between serotonin and the sensing surface, eliciting responses for glyphosate aptamer and MCH-only functionalized FGTs. More so, the serotonin FGT biosensor responded to a cocktail of control analytes, further revealing nonspecific small molecule-SAM interactions can elicit FGT responses. XPS characterization after stabilization in 1X PBS and serotonin sensing measurements revealed desorption of thiols from the sensing surface, indicating electrochemical instabilities.

The final study considers the electrochemical potential window as a parameter for stable FGT biosensors. Cyclic voltammetry was used to mimic the quasi-static potential windows that interrogate the sensing surface in the presence of electrolyte. Windows were applied within ±1 V for various functionalized surfaces, including the surfaces of chapter 4 and chapter 5. Stability of individual thiols contributed to the stability of the mixed monolayer, as revealed for the aptamer/MCH system. Antibody-functionalized surfaces exhibited greater stability in 1X PBS compared to aptamer/MCH-functionalized surfaces which was attributed to changes in the density

and thickness of the layer. These windows can be translated to the FGT biosensor to roughly set stable operating bounds. Faster sweep rates, or less time exposed to electrochemical potentials, decreased the effective destabilization per sweep.

Although detection with an FGT biosensor has been achieved with large and charged biological molecules, it is clear the platform is stunted by additional parameters for stable and sensitive detection, especially toward small molecule analytes. Aside from parameters included in FGT models, we consider how electrochemical interrogation and the surface composition prevent or conflate signals, informing future studies to mitigate losses and enhance signals.

Table of Contents

Acknowledgements i
Abstract iii
Table of Contents vi
List of Figures viii
List of Tables xi
Abbreviations xii
Statements of Authors' Contribution xiv
Chapter 1. Background & Introduction 1
1.1 Basics of Biosensors 2
1.2 Bio/chemical Sensing with Electrolyte-Gated Transistors 3
1.3 The Floating Gate Transistor Biosensor 7
1.4 Electrochemical Aptamer-based Sensors and Monolayer Stability 10
1.5 Small Molecule Detection: Existing Methods and Considerations for FGT Sensing 13
Chapter 2. Materials & Methods 16
2.1 Materials for FGT Fabrication 16
2.2 Materials for Antibody Conjugation and Sensing 16
2.3 Materials for Aptamer Conjugation and Sensing 17
2.4 Electrode Patterning of FGTs 17
2.5 Aerosol Jet Printing of EGTs 18
2.6 FGT Cleaning and Functionalization 19
2.7 X-ray Photoelectron Spectroscopy (XPS) 21
2.8 Reflection-Absorption Infrared Spectroscopy (RAIRS) 21
2.9 Epifluorescence Microscopy 22
2.10 Cyclic Voltammetry (CV) 22
Chapter 3. Reconsidering Parasitic Capacitance in FGTs and Optimizing EGT Operation* 23
3.1 Introduction and Motivation 23
3.2 Experiments 24

3.3 Results and Discussion 26
3.4 Optimizing the EGT as a Signal Transducer 32
3.5 Conclusion 37
Chapter 4. Designing an Antibody-based FGT Toward Small Molecule Detection 39
4.1 Introduction and Motivation 39
4.2 Experiments 41
4.3 Surface Characterization 45
4.4 Sensor Results and Discussion 55
4.5 Conclusions 61
Chapter 5: Designing an Aptamer-based FGT Toward Small Molecule Detection 62
5.1 Introduction & Motivation 62
5.2 Experiments 64
5.3 Surface Characterization 67
5.4 Sensor Results and Discussion 69
5.5 Conclusions 78
Chapter 6: Electrochemical Interrogation of Functionalized Surfaces 80
6.1 Introduction and Motivation 80
6.2 Experiments 82
6.3 Results and Discussion 83
6.4 Conclusions 97
Chapter 7: Final Remarks and Outlooks 99
7.1 Summary 99
7.2 Exploring the Limits of Interfacial Charge Sensing 103
7.3 Tailoring Surface Composition for Enhanced and Stable FGT Sensing 107
Bibliography 111
Appendix A – EGT Studies 128
Appendix B – Glyphosate FGT Biosensor Characterization 129
Appendix C – FGT Biosensor Design 134
Appendix D – Serotonin FGT Biosensor Characterization 135
Appendix E – Electrochemical Stability of 11-MUA and Antibody-Conjugated Electrodes 137

List of Figures

Figure 1.1 Biosensing pathway. 2
Figure 1.2. Scheme of EGT architectures and configuration. 4
Figure 1.3. Scheme of the FGT inverter. 7
Figure 1.4. Scheme of E-AB sensors. 10
Figure 2.1. Aerosol jet printing. 18
Figure 2.2. FGT sensor preparation. 20
Figure 3.1. Schematic representation of FGT with parasitic capacitance. 26
Figure 3.2. EGT transfer curves. 28
Figure 3.3. Area dependence of FG2 on FGT and EGT operation 29
Figure 3.4. Model of 1/κCGf vs 1/C2 to extract f. 31
Figure 3.5. EGT transfer curve characteristics over 28 days in ambient air. 33
Figure 3.6. Effect of high humidity on EGT. 34
Figure 3.7. EGT inverters after 27 weeks in the glove box 35
Figure 3.8. EGT inverter with varied sweep rates. 36
Figure 4.1. Diagram of the glyphosate FGT biosensor. 40
Figure 4.2. Antibody conjugation to gold through carboxyl-to-amine crosslinking. 45
Figure 4.3. XPS of 11-MUA and PEG monolayer. 46
Figure 4.4. Time-dependent formation of 11-MUA and PEG thiol mixed monolayer. 48
Figure 4.5. RAIRS spectra of EDC/NHS activation and antibody conjugation 50
Figure 4.6. XPS of antibody conjugation to gold. 51
Figure 4.7. XPS characterization of antibody conjugation to FG2 52
Figure 4.8. CV of 11-MUA and antibody conjugation. 53
Figure 4.9. Inverter curve shift with antibody conjugation to FG2. 55
Figure 4.10. Glyphosate FGT biosensor inverter curve shift after glyphosate dosing. 56
Figure 4.11. Response of glyphosate FGT biosensors and controls to glyphosate 57
Figure 5.1. Diagram of the serotonin FGT biosensor. 63

Figure 5.2. XPS of aptamer/MCH-functionalized FG2 electrodes. 67
Figure 5.3. Cyclic voltammograms of aptamer/MCH functionalization. 68
Figure 5.4. Inverter curve shift with aptamer/MCH functionalization of FG2. 69
Figure 5.5. Concentration dependence and selectivity of serotonin FGT biosensor 70
Figure 5.6. Functionalized control FGTs respond to serotonin. 72
Figure 5.7. MCH FGTs stabilized in 1X PBS and subsequent exposure to 1 mM serotonin. 74
Figure 5.8. XPS of interrogated MCH-functionalized FG2 electrodes. 75
Figure 6.1. Schematic representation of electrochemically-induced thiol desorption in an FGT. 80
Figure 6.2. CV of bare gold electrodes with 10 mM $[Fe(CN)_6]^{3-/4-}$. 84
Figure 6.3. Electrochemical stability of MCH-only and aptamer-only functionalized gold electrodes in 1X PBS with the redox reporter. 85
Figure 6.4. Electrochemical stability of aptamer/MCH-functionalized gold electrodes in 1X PBS with the redox reporter. 86
Figure 6.5. Changes in ΔE_p after the interrogation of aptamer/MCH electrodes for each potential window. 87
Figure 6.6. Electrochemical stability of aptamer-functionalized gold electrodes with varied sweep rate. 89
Figure 6.7. Interrogation of bare gold working electrode with CV in 1X PBS. 90
Figure 6.8. CV of functionalized electrodes in 1X PBS 91
Figure 6.9. Electrochemical stability of aptamer/MCH-functionalized gold electrodes in 1X PBS. 92
Figure 6.10. Full voltammograms of aptamer/MCH-functionalized electrodes before and after electrochemical interrogation in 1X PBS. 93
Figure 6.11. Comparing CV to FGT electrochemical interrogation. 95
Figure 7.1. Altering the length of carboxylic acid-terminated thiols 104
Figure 7.2. In situ infrared spectroscopy under microfluidic flow 109
Figure A.1. Capacitance of P3HT/ion gel interface 128
Figure B.1. XPS of time-dependent monolayer formation of 11-MUA 129
Figure B.2. XPS of time dependent monolayer formation of PEG thiol. 130
Figure B.3. XPS of 11-MUA and PEG thiol mixed monolayer (1:2 molar ratio 130

Figure B.4. XPS of Au_{4f} attenuation upon antibody conjugation. 131
Figure B.5. XPS of self-assembly of 11-MUA with different gold cleaning protocols. 132
Figure B.6. Glyphosate antibody conjugation onto CM5 chip with SPR. 133
Figure D.1. Serotonin FGT inverter curve shift after serotonin dosing 135
Figure D.2. Response to serotonin depends on the functionalization response 136
Figure D.3. HxSH and PEG FGTs response to 10 µM serotonin. 136
Figure E.1. Electrochemical stability of 11-MUA functionalized gold electrodes with varying positive potentials. 137
Figure E.2. Electrochemical stability of 11-MUA functionalized gold electrodes with varying negative potentials. 138
Figure E.3. Electrochemical stability of antibody-functionalized gold electrodes with varying positive potentials. 139
Figure E.4. Electrochemical stability of antibody-functionalized gold electrodes with varying negative potentials. 140

List of Tables

Table 5.1. Serotonin aptamer selectivity with SPR. 71

Table B.1. Experimental conditions for glyphosate SPR trials. 133

Abbreviations

11-MUA	11-Mercaptoundecanoic acid
A	Area
C	Capacitance
C_i	Specific capacitance
CG	Control gate
CV	Cyclic voltammetry
E_p	Peak potential from cyclic voltammogram
EAB	Electrochemical aptamer-based
EDC/NHS	Intermediate, activation chemistry toward carboxyl-to-amine crosslinking
EGT	Electrolyte-gated transistor
f	Fraction of charge lost to parasitic capacitance in an FGT
FET	Field-effect transistor
FG1	Lower end of the floating gate
FG2	Upper end of the floating gate (sensing surface)
FGT	Floating gate transistor
I_D	Source-drain current
I_G	Gate-source current
K_D	Equilibrium dissociation constant
L	Length of the semiconductor channel
LOD	Limit of detection
MCH	6-mercapto-1-hexanol
OECT	Organic electrochemical transistor
ORR	Oxygen reduction reaction
P3HT	Poly(3-hexylthiophene-2,5-diyl) (organic semiconductor)
PEG thiol	Poly(ethylene glycol) methyl ether thiol
Peak ΔV_{OUT}	Peak signal output, FGT biosensor signal
PBS	Phosphate-buffered saline
Q	Charge

R_L	Load resistor
RAIRS	Reflection-absorption infrared spectroscopy
SAM	Self-assembled monolayer
SPR	Surface plasmon resonance
TE	Tris-EDTA
V_D	Drain-source voltage
V_{DD}	Drain-source voltage (inverter configuration)
V_F	Floating gate voltage
V_G	Gate-source voltage
V_{OUT}	Output voltage
ΔV_{OUT}	FGT biosensor signal output
V_T	Threshold voltage
V_W	Working voltage
W	Width of the semiconductor channel
XPS	X-ray photoelectron spectroscopy

λ_D	Debye length
κ	Intrinsic potential drop for FGT models
μ	Semiconductor mobility
φ	Surface potential

Statements of Authors' Contribution

Portions of this dissertation were written in collaboration with Dr. Mathew S. Thomas, Dr. Jiayi He, Clarice E. Froehlich, Prof. Daniel Frisbie, Prof. Kevin D. Dorfman, and Prof. Christy Haynes. In Chapter 4, C.E.F. assisted with conducting SPR measurements. In Chapter 5, C.E.F. and J.H. conducted the SPR measurements. In Chapters 5 and 6, J.H. conducted a portion of the sensing and CV measurements.

Part of Chapter 3 was published in an article: Thomas, M.S.; Adrahtas, D.Z., Frisbie, C. D., Dorfman, K. D.; Modeling of Quasi-Static Floating-Gate Transistor Biosensors. *ACS Sensors* (2021), 6(5), 1910-1917. In this work, we investigate the influence of FGT architecture, materials, and device operation on the amplification of charge-based and capacitance-based FGT signals. Further, predictive models were developed and outlined to provide a roadmap for FGT design. I performed experiments and data analysis related to parasitic capacitance for this paper.

Chapter 1. Background & Introduction

With the onset of the COVID-19 pandemic, it is evident how the use of portable, on-site biosensors can shape healthcare and public health outcomes. Translating the goal of analytical instrumentation to detect molecules of interest to an easy-to-use, inexpensive platform not only has the potential to revolutionize how we approach diagnostics but can also enable high-throughput screening in food safety and environmental protection industries. As the United States lacks the use of the precautionary principle, products are able to reach the market before toxicity analyses are done on the chemicals used for their products. Within these industries, small molecules with widespread use, such as those used in commercial products and herbicides, can pose environmental and public health risks where current analytical testing cannot meet and maintain widespread monitoring. Where the level of concern depends on the concentration of the target analyte, a quantitative sensor platform is necessary. Like the blood glucose meter, electrochemical biosensors can fulfill this criterion while also providing an adaptable platform for sensitive and specific detection. In this vein, development of adaptable and portable electrochemical biosensors can lead toward larger-scale monitoring of small molecule toxins, resulting in higher accessibility to testing and regulation better reflecting public health and ecological risks. This thesis highlights the need for thorough surface characterization to properly design of the sensing interface and how it may influence the sensing mechanism and stability of a type of electrochemical biosensor, the floating gate transistor biosensor.

1.1 Basics of Biosensors

Biosensing technologies have been integrated into the workflow of several fields, including medical diagnostics,[1,2] food safety and regulation,[3,4] and environmental monitoring[5] as commercial products and tools for research. Advanced analytical instrumentation, such as mass spectrometry (MS) and liquid chromatography-MS (LC-MS), are also widely adopted tools for highly specific and sensitive detection of molecules, such as proteins [6–8] and small molecules. [9]

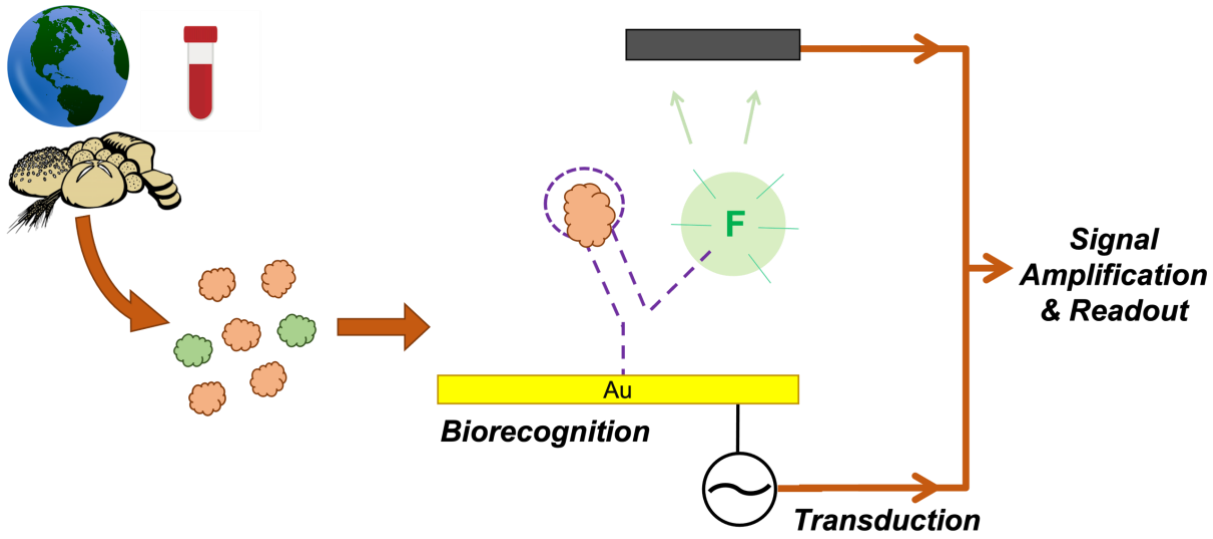

Figure 1.1 Biosensing pathway. Upon target-binding to an immobilized capture agent, signals can be transduced optically or electronically. Signal amplification and readout follow.

However, their complex methodologies require trained technicians and result in expensive testing compared to commercial biosensors that are cost-effective, portable, and user-friendly. Compared to traditional analytical techniques, biosensors utilize a capture agent and a transducer in order to produce a measurable physical or chemical change when a target analyte binds to its capture agent (e.g., an antigen-antibody complex). The design of biosensors, thus, has revolved around three elements to deliver a response upon target binding: biorecognition; signal transduction; and signal amplification (Fig 1.1).

Owing to the broad library of analytes and their chemical nature, methods have been tailored to achieve sensitivity and selectivity toward a single analyte (e.g., blood glucose meters and pregnancy tests). For research and diagnostic tests, a commonly used, state-of-the-art detection platform for a large volume of samples and broad applicability is the enzyme linked immunosorbent assay (ELISA) kit. Sandwich ELISA kits work by immobilizing antibodies to the well walls of microplates where the binding of the target analyte is followed with an enzyme-labeled secondary antibody. Subsequent conjugation of a colorigenic substrate to the enzyme elicits an optical response that corresponds to the concentration of the target analyte. Signals are optically transduced with a spectrophotometer, or plate reader, to provide quantitative readouts.[10] Other optical biosensors, including lateral flow immunoassays (e.g. pregnancy tests), have integrated spectroscopic tools such as surface enhanced Raman spectroscopy (SERS)[11,12] and surface plasmon resonance (SPR)[2,13] for signal amplification and quantification. Recent work is beginning to demonstrate portability for such advanced optical biosensors.[14,15] The following section details an alternative approach that uses electronic signal transduction and amplification strategies.

1.2 Bio/chemical Sensing with Electrolyte-Gated Transistors

Electrochemical biosensors, such as the aforementioned blood glucose meter, uniquely combine an understanding of electronics, chemistry, and biology to package nearly all key elements of a biosensor into one device. Of this class, transistor-based biosensors, including field-effect transistors (FETs) and electrolyte-gated transistors (EGTs), have been employed over the past several decades due to their ability to relay and amplify electrochemical detection events, be it change in pH or molecular binding events, into electronic signals.[16–18] Transistors are

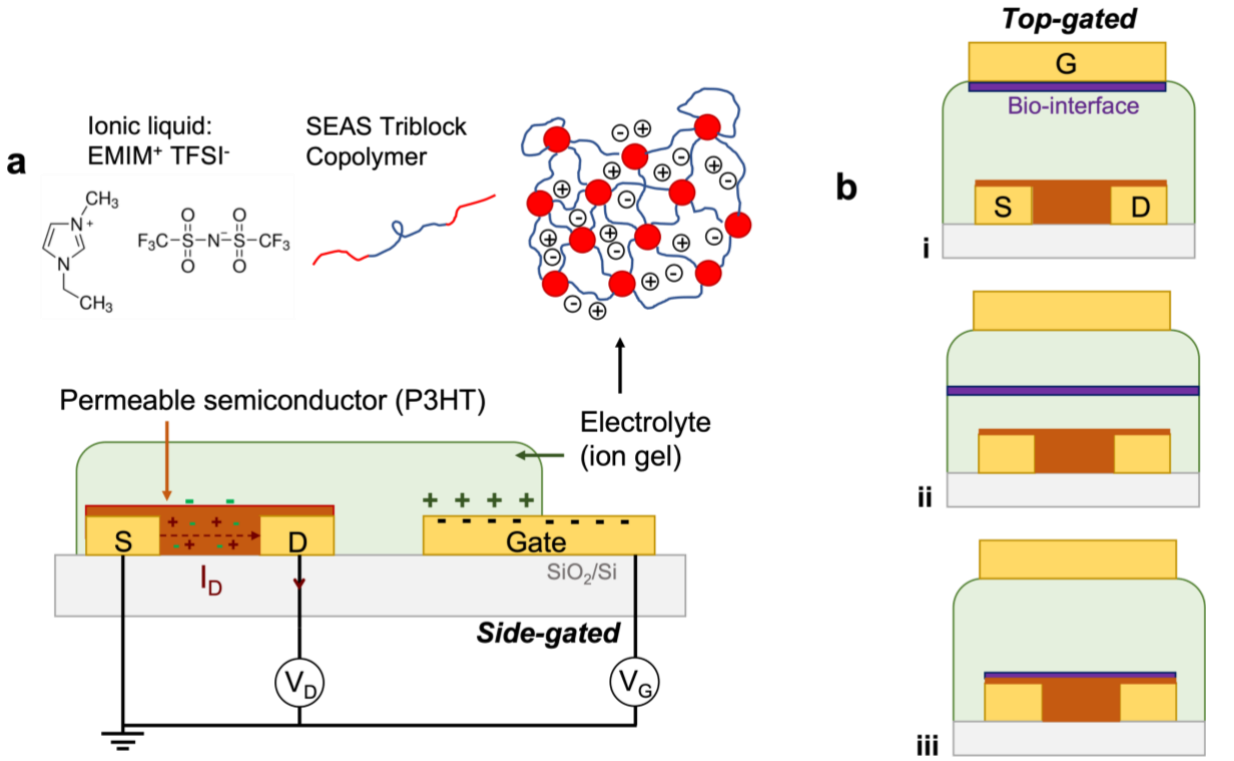

Figure 1.2. Scheme of EGT architectures and configuration. (a) Schematic of a side-gated EGT, outlining the source (S), drain (D), and gate electrodes. The organic semiconductor is P3HT, and the electrolyte is an ion gel composed of ionic liquid and polymer. The drain voltage, V_D, is applied between the source and drain. The gate voltage, V_G, is applied between the gate and source. The drain current is denoted as I_D. (b) Top-gated EGT with a bio-interfacial layer for biosensing located (i) on the gate, (ii) within the electrolyte, and (iii) on the semiconductor. Adapted with permission from Torricelli, F.; Adrahtas, D. Z.; Bao, Z.; Berggren, M.; Biscarini, F.; Bonfiglio, A.; Bortolotti, C. A.; Frisbie, C. D; et al. Electrolyte-Gated Transistors for Enhanced Performance Bioelectronics. *Nature Reviews Methods Primers* **2021**, *1* (66). Copyright 2021 Springer Nature.

three-terminal devices, consisting of source, drain, and gate electrodes. The semiconductor, which lies between the source and drain, is capacitively coupled to the gate electrode through a dielectric material. Minor changes in the gate-source voltage, which alters the electric field through the dielectric, can elicit a significant change in the conductivity of the semiconductor, enabling the sensitivity needed to transduce minor potentiometric or capacitive changes upon molecular binding events at semiconductor or gate interfaces.

Compared to conventional transistors, the EGT utilizes an electrolyte in the place of a dielectric material (e.g. SiO_2), as shown in Fig 1.2a. Rather than polarization of the dielectric, ions in the electrolyte are polarized upon a voltage application at the gate, inducing capacitances on the order of nanometers thick that have no thickness dependence.[19] Such capacitances can be as high as 50 μF/cm^2 at gold interfaces[20] and 200 μF/cm^2 for permeable semiconductors,[19,21] enabling low voltage operation (sub-1V) and greater amplification capabilities. Upon applying a negative gate voltage, V_G, for a p-type EGT, the ions in the electrolyte polarize, storing charge at the electrode and semiconductor interfaces through capacitive coupling. Capacitances either result from the formation of an EDL at the interface or from the penetration of ions into the semiconductor (if permeable).[19] Once the potential at the semiconductor exceeds the threshold voltage, V_T, a conductive channel is induced in the semiconductor, resulting in an increase in free charge carriers or holes for p-type semiconductors. With a voltage applied between the source and drain, V_D, the output or source-to-drain current, I_D, increases by several orders of magnitude. Measures of I_D as a function of V_G with a constant application of V_D are termed transfer curves. The relationship between the I_D and V_G is dictated by the square law current equation:

$$I_D = \frac{W\mu C_i}{L}\left[(V_G - V_T)V_D - \frac{V_D^2}{2}\right]^2 \qquad (1.1)$$

Where I_D is dependent on V_D and properties of the semiconductor: width (W) and length (L) of the channel, mobility of the free carriers (μ), and specific capacitance (C_i) of the semiconductor/electrolyte interface. The specific capacitance is the ratio of the capacitance to the area of the interface.

In considering the case of a p-type semiconductor, this equation is valid when $V_G - V_T < 0$. However, the equation can be simplified to two specific regimes when considering V_D: [22]

Linear, $V_D << V_G - V_T$

$$I_D = \frac{W\mu C_i}{L}(V_G - V_T)\,V_D \tag{1.2}$$

Saturation, $V_D > V_G - V_T$

$$I_D = \frac{W}{2L}\mu C_i (V_G - V_T)^2 \tag{1.3}$$

The linear regime yields a linear I_D–V_G relationship; whereas, in the saturation regime, all of the free carriers induced in the channel are swept by the high V_D, producing a "saturated" current. EGT sensors in this work operate within the saturation regime where the output is more sensitive to changes in V_G.

It is important to distinguish EGTs and organic electrochemical transistors (OECTs), a class of electrochemical transistors inspired by EGTs and used for sensing applications. OECTs similarly use an electrolyte for gating, but instead of a semiconductor, they commonly employ a conducting polymer, PEDOT:PSS.[23–25] Here, OECTs are grouped into the broader class of EGTs. Electrolytes extend to any media containing mobile ions, including aqueous buffers,[26] biological media, food/beverage media,[27,28] ion-conducting membranes,[29,30] ionic liquids, and ion gels.[19,31]

Included in Fig 1.2b, the bio-interfacial layer, where biorecognition occurs, is typically located at one of two important transistor surfaces: the gating electrode or the semiconductor. This builds a sensing surface designed for specific binding to target molecules and electrochemical relaying of those events to the transistor. Here, target molecule binding events alter the electronic state of the surface, such as the capacitance or potential of the interface, directly influencing the transistor's operation based on the target molecule's concentration to produce a quantifiable, electronic signal. This is often quantified by changes in V_T or I_D at a specific V_G after the target analyte is introduced. EGTs are especially suitable for signal transduction and amplification due to their high transconductance (dI_D/dV_G),[18,19] while additive manufacturing of these devices via direct-write printing[19,32,33] presents the opportunity for facile materials- and cost-saving

fabrication. To date, EGTs have been employed for a variety of bioelectronic applications: cell monitoring, ultrasensitive diagnostics, electrophysiology, neuromorphics, and synaptics.[18] In some of these cases, a bio-interfacial layer can also be suspended within the electrolyte, for example, for ion-selective detection[34] and cell monitoring.[35,36]

1.3 The Floating Gate Transistor Biosensor

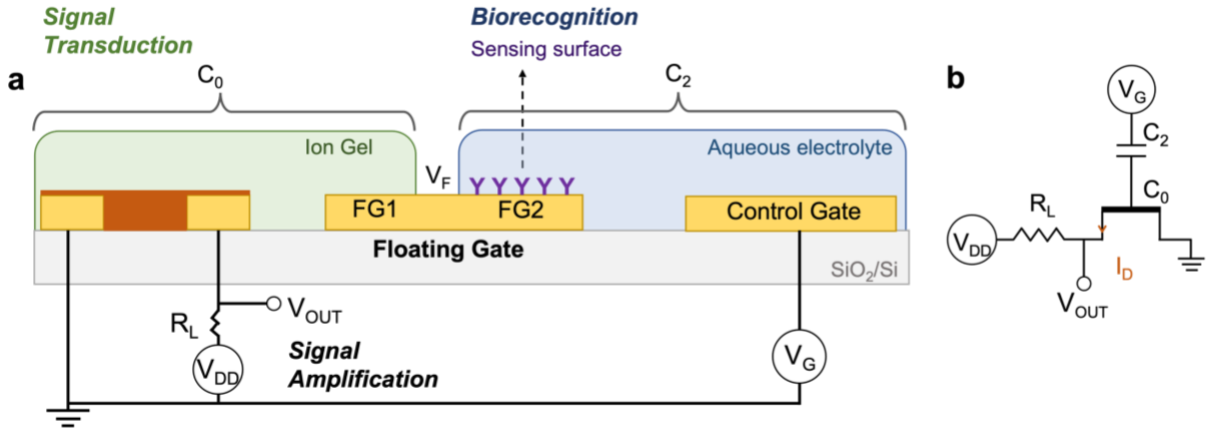

Figure 1.3. Scheme of the FGT inverter. (a) Side-on view of the device, where the signal transduction element is a side-gated electrolyte-gated transistor. The floating gate couples the device to the biorecognition element, an aqueous electrolyte compartment with a functionalized floating gate for target capture. Signals are further amplified with the inverter configuration. The drain voltage is denoted as V_{DD}. The load resistor is denoted R_L. The output voltage, V_{OUT}, measures the potential between the channel and ground.

Another type of architecture utilized for EGT sensing is an extended-gated architecture.[37] Similar to the side-gated architecture, the gate is extended to a second compartment containing an aqueous electrolyte for gating and sensing. Two common extended gate architectures found in the literature are organic charge modulated FET (OCMFET)[38–40] and the floating gate, electrolyte-gated transistor (FGT).[27,28,41,42] This work utilizes the FGT. As illustrated in Fig 1.3, the floating gate physically separates and electronically couples the sensing medium, where biorecognition occurs, and the signal transducer, an EGT. In this and previous work, the EGT (first compartment)

is comprised of a P3HT semiconductor (p-type) that is gated by the left end of the floating gate (FG1) through an ion gel electrolyte ([EMIM][TFSI]-SEAS). The sensing medium (second compartment) contains the control gate (CG), used to gate the device, and the right end of the floating gate (FG2). An aqueous electrolyte is used for gating and as the sample medium. The physical separation resolves any potential material incompatibility between the aqueous solutions and electronic materials comprising the transistor. Further, this design enables independent engineering of the two compartments. Moreover, the gold floating gate is well suited for versatile self-assembled monolayer (SAM) chemistry for the immobilization of capture agents at FG2.[43] White et al. demonstrated the ability design the FGT for biosensing applications in 2014.[42] A SAM of single-stranded DNA was immobilized onto FG2. After incubating the sensing surface with the complementary strand, V_T of the same device shifted more negatively due to hybridization, where negative charges along the DNA backbone accumulate near the sensing interface. The magnitude of the V_T shift scaled with concentration of the complementary strand, generating a dose-response curve. The FGT biosensor has also achieved detection of ricin in potable media (e.g., milk and orange juice)[28] and distinguished between various sources of gluten.[27] Here, microfluidics and an inverter configuration were integrated to alleviate mass transfer limitations and to further amplify signals, respectively. In the inverter configuration, outlined in Fig 1.3, a load resistor (R_L) is positioned between the drain voltage (V_{DD}) and the P3HT channel.[28]

To understand how biorecognition is translated into an electronic signal with the EGT, it is first important to understand how an FGT operates. When a negative V_G is applied to the FGT at the control gate (CG), cations from the aqueous electrolyte are attracted to CG, creating an EDL at the CG-electrolyte interface. This polarization of the electrolyte leads to anions accumulating at the sensing surface (FG2), with subsequent electronic polarization of the floating gate to form a

second double layer whose capacitance is termed C_{FG2}. The two double layer capacitors in series (C_{CG} and C_{FG2}) form a lumped capacitance for the sensing compartment, termed C_2, and the intentional oversizing of the control gate causes C_{FG2} to be the dominant contributor to C_2, i.e., $C_2 = C_{CG}C_{FG2}/(C_{CG} + C_{FG2}) \approx C_{FG2}$.[21,41] In turn, the positive polarization of the floating gate at FG2 means there is negative polarization at FG1 (the other end of the floating gate), which is in contact with the ion gel electrolyte of the EGT. Cations are attracted to FG1, and a third double layer forms. The polarization of the ion gel by FG1 results in anion accumulation at the P3HT semiconductor, facilitating electrochemical doping of the material and increasing its conductivity.[19] Thus, there is an effective electrochemical capacitance at the P3HT/gel interface termed C_{P3HT},[21,41] and FG1 is intentionally oversized such that, $C_0 = C_{FG1}C_{P3HT}/(C_{FG1} + C_{P3HT}) \approx C_{P3HT}$. Considering now the full impact of this cascade of polarization events, application of a negative V_G on CG causes polarization of the floating gate and thus accumulation of charge carriers (holes) in P3HT, turning on the EGT channel and generating I_D. As the channel conductivity, and thus I_D, increase as V_G becomes more negative, an increasing fraction of V_{DD} is dropped across R_L due to I_D, causing the output potential (V_{OUT}) to move toward ground. Alternatively, when the channel is highly resistive (off state at positive V_G), V_{OUT} remains equal to $V_{DD} = –0.5$ V. So, the sensor output signal ranges from 0 to –0.5 V depending on the sign and magnitude of V_G. By raising the resistance of R_L, the rate between V_{OUT} and V_G, otherwise known as the gain, increases. The gain is also impacted by the coupling of the two compartments, where decreasing potential losses between the two ends of the floating gate increases the gain.[21]

A critical point is that the impact of V_G on the device is modified by surface functionalization of the floating gate sensor surface, FG2. This is because the gate voltage that the EGT experiences is not V_G but V_{FG}, the floating gate potential (the EGT is coupled directly to

FG1, not CG). V_{FG} in turn depends on $C_2 \approx C_{FG2}$ and $\Delta\varphi$, the surface potential change at the FG2/electrolyte interface due to adsorption of a charged analyte, as follows:[41]

$$V_{FG} = \frac{V_G}{1 + \frac{C_0}{C_2}} + \Delta\varphi \tag{1.4}$$

Changes in C_2 or $\Delta\varphi$ due to target adsorption on FG2 result in changes in V_{FG} and thus impact the conductivity of P3HT and the magnitude of the sensor output, V_{OUT}. Past work dedicated to understanding the sensing mechanism revealed that changes in interfacial charge ($\Delta\varphi$) and capacitance (C_2) at FG2 independently alter transfer and inverter curve characteristics.[44,45] Our recent study expands on these findings for quasi-static FGT biosensors in the inverter configuration where we demonstrated that the capacitance of the electrodes can be altered to achieve higher signals for either charge- or capacitance-based sensing.[21]

1.4 Electrochemical Aptamer-based Sensors and Monolayer Stability

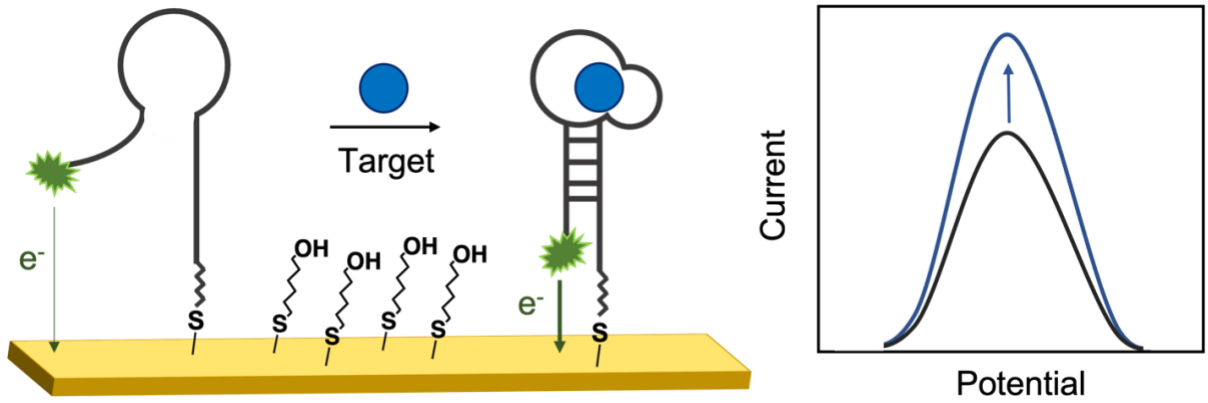

Figure 1.4. Scheme of E-AB sensors. Redox-tagged aptamers undergo a structural reorganization upon target-binding, further enabling charge transfer between the redox tag and the electrode with the electrochemical window.

Electrochemical aptamer-based sensors, or EAB sensors, differ from EGTs in that the signal is amperometric based on a redox-tagged aptamer. Traditionally, EAB sensors are

composed of a conductive electrode and surface-bound, redox-tagged aptamers, whose changes in confirmation yield a change in current proportional to the target concentration (Fig 1.4).[46–51] Aptamers can be isolated using a large library of oligonucleotides and the SELEX process, providing a relatively simpler means for discovering a selective and specific aptamer for any target molecule as compared to eliciting an immunogenic response for developing antibodies.[52] Additionally, aptamers are increasingly attractive for sensing applications due to their longer shelf life and the ability to synthesize them as-is or with linkers, such as redox-tags and C_6 thiols.[53] More so, engineering the aptamer to not only have a structure-switching mechanism,[54] but a significant molecular switch, has enabled 30-fold signal gain with aptamers.[55] Square wave voltammetry is often used to measure current from an oscillating voltage, whose frequency is optimized to maximize the current measured from charge transfer.[49]

Early use of EAB sensors saw real-time biosensing of therapeutic agents in animals, providing a promise platform for future diagnostics.[47] However, their development since has focused on parameters affecting signal gain and preservation over continuous use. This prompts revisiting literature on the desorption of thiols via reduction and oxidation at gold interfaces when interrogated in aqueous solvents.[56–62]

The reductive desorption of thiols is understood as a one electron process with the electrochemical half reaction[63]

$$AuSR + 1\ e^- \rightarrow Au(0) + RS^- \qquad (1.5)$$

where R represents the thiol chain. Additionally, oxidation desorption of thiols, in the case of 100 mV/s sweeps, is understood as a three electron process having the reaction[57,63]

$$AuSR + 2\ H_2O \rightarrow Au(0) + RSO_2^- + 3\ e^- + 4\ H^+ \qquad (1.6)$$

The reactions for oxidative desorption vary on a case-to-case basis where sweep rate and electrolyte are relevant variables.[64] These electrochemical processes have been monitored for various SAMs on electrodes using chronoamperometry,[61] cyclic voltammetry,[57,60,62,63] fluorescence microscopy,[56] in situ sum frequency generation vibrational spectroscopy,[65] quartz crystal microbalance,[59] surface plasmon resonance,[64] and time of flight secondary ion mass spectrometry[58] with various thiols and electrolytes. As EAB sensors utilize thiol self-assembly on gold, parameters such as the redox tag,[66] interrogation modality,[67–69] backfilling thiols,[70] and aptamer density[67,68] were investigated due to their contributions to signal loss/gain at the sensing interface due to desorption of bound aptamers in various electrolyte environments where high temperatures, fouling, and enzymatic attacks can further contribute to signal loss. Attention and investigation into these parameters has produced EAB sensors engineered for week-long operation in both buffer and serum, a biologically relevant media.[67] Recently, the sensing mechanism behind EAB sensors has been translated to the gate electrode of an organic electrochemical transistor (OECT) that operates similarly to EGTs.[71] In this configuration, the current upon target capture is amplified by the OECT, dictated by the device's transconductance. Structure-shifting aptamers have more recently been translated to FET biosensors for use as capture agents;[72] however, their conjugation has been primarily at the semiconductor interface. For use in FGTs, where conjugation occurs at the gold floating gate, it is important to note the present electrochemical instabilities EAB sensors face and how they are translated to devices operating with quasi-static potentials. Furthermore, these sources of instability must also be investigated for all biosensing interfaces built upon self-assembled monolayers (SAMs).

1.5 Small Molecule Detection: Existing Methods and Considerations for FGT Sensing

Many widely-used small molecules with industrial relevance have emerged as public health and ecological threats, such as glyphosate,[73,74] bisphenol-A,[75,76] and perfluoroalkyl and polyfluoroalkyl substances (PFAS).[77,78] Standard detection methods extend to advanced, mass-based analytical instrumentation, such as high-performance liquid chromatography (HPLC) and liquid chromatography/tandem mass spectrometry (LC/MS-MS).[79] These are robust but require expensive laboratory facilities and trained technicians, usually leading to long turnaround times, qualities in stark contrast to most biosensors.[79–81] In looking toward ease of use and data interpretation, Enzyme-linked Immuno-sorbent Assays (ELISA) kits satisfy these criteria and are the gold standard for use in hospital and research settings. However, the need for plate preparation, plate readers (spectrophotometers), and relatively long detection times (3 h) are limitations for evolving the platform for widespread and on-site use.

As was evident during the COVID-19 pandemic, simple-use, rapid, low-cost, and portable biosensors can lead to convenient and widespread monitoring of health threats. Moreover, the combination of broader accessibility to testing and new avenues of research opened by new technologies can provide the scientific basis for regulation, better reflecting the public health and ecological risks such molecules can pose. As the sensing mechanisms and signal amplification strategies are better understood with recent FGT models, we look toward extending the library of detectable analytes, including large, charged proteins and ssDNA, to small molecules. Small molecule detection by FGTs, however, must overcome three major issues pertaining to electrochemical biosensors: Debye length limitations, fouling from interferents in solution, and electrochemical stability of sensing interfaces. Strategies to overcome these limitations include tailoring the sensing surface composition,[82–87] adjusting the electrochemical interrogation of the

surface,[68,69,88] and usage of structure-shifting aptamers[72,89] or molecularly imprinted polymers[90–93] as recognition elements.

Whether the sensor be amperometric, potentiometric, or capacitive, the main commonality between EGT and EAB sensors is the reliance on the sensing surface for critical elements of detection: biorecognition, signal transduction, and signal amplification. In this vein, it is important to thoroughly characterize the sensing surface to both verify that the capture agent is tethered to the surface and that adjacent molecules, like backfilling and/or antifouling agents, are present. Furthermore, as these molecules on the surface can have an impact on sensing,[70,94] characterization of the surface composition (e.g. the ratio of each molecule on the surface) can improve understanding of how sensing is impacted. Past FGT sensor work has characterized surface functionalization with epifluorescence microscopy for DNA patterning,[42] Rutherford backscattering spectroscopy for monolayer density,[44] and cyclic voltammetry to measure the capacitance of alkylthiols of varied chain length.[21] The FGT also served as a form of characterization, where the effects of pH on ionizable thiols and the capacitance changes of extending alkylthiols reflected, as expected, on the electrical characteristics of the device.[21,44,45]

With the aim of small molecule detection with an FGT biosensor, this thesis looks toward both antibodies and aptamers as capture agents. To enhance the understanding of the FGT sensing mechanism, the charge lost between the sensing medium and EGT was reframed to be understood as differences in capacitance among the FGT interfaces. Influenced by this understanding, models for charge-based signals using quasi-static FGTs in the inverter configuraiton[21] were then utilized for the first time, and additional parameters to improve sensing are considered. Surface characterization was extended to other advanced, surface-sensitive tools to achieve characterization of multi-step chemistries, such as those necessary for antibody conjugation, and

of functionalization directly on the FG2 electrode to guarantee translation of these chemistries to the millimeter sized electrode was possible. Furthermore, these tools can be utilized to understand the effects that electrochemical interrogation, either by the FGT or CV, have on the surface.

Chapter 2. Materials & Methods

Below is a detailed description of the materials and methods used in this work. Specifics to each chapter are provided in their Experiments subsection.

2.1 Materials for FGT Fabrication

P-doped silicon wafers having a four inch diameter and a 300 nm silicon dioxide (SiO_2) film were purchased from Silicon Valley Microelectronics (Santa Clara, CA). Fused silica, or glass, wafers having a four inch diameter were purchased from University Wafer (South Boston, MA) and used for studies on parasitic capacitance. Electronic grade regioregular poly(3-hexylthiophene-2,5-diyl), or P3HT, was purchased from Rieke Metals (Lincoln, NE) and serves as the organic semiconductor used throughout this work. The ion gel used consisted of a triblock co-polymer, poly(styrene-b-ethylacrylate-b-styrene) or SEAS, and an ionic liquid, 1-ethyl-3-methyl-imidazolium bis(trifluoromethyl sulfonylimide) or [EMIM][TFSI]. SEAS was synthesized in-house as reported by Tang et al.[95] Chloroform, [EMIM][TFSI], ethyl acetate, terpineol, and polystyrene were purchased from Sigma-Aldrich. Stainless steel stencils were purchased from Photo Etch Technology (Lowell, MA).

2.2 Materials for Antibody Conjugation and Sensing

11-mercaptoundecanoic acid (11-MUA), poly(ethylene glycol) methyl ether thiol (M_n ~ 800), 1-ethyl-3-(3-dimethylaminopropyl)carbodiimide HCl (EDC), N-hydroxysuccinimide (NHS), glyphosate, potassium hexacyanoferrate (III), and 200 proof ethanol were purchased from Sigma-Aldrich. 2-(N-morpholino)ethanesulfonic acid (MES), 10X phosphate buffered saline (PBS), HPLC water, hydrochloric acid, sodium hydroxide, and ethanolamine HCl were purchased

from Fisher Scientific. Glyphosate antibodies (5 mg/mL) and AlexaFluor647 IgY antibodies (5 mg/mL) were purchased from Thermo Fisher Scientific (Waltham, MA). The glyphosate antibody solution was aliquoted and stored in the freezer at –20 °C. Krayden Dow Sylgard 184 Silicone Elastomer (PDMS) Kits were purchased from Fisher Scientific.

2.3 Materials for Aptamer Conjugation and Sensing

The serotonin aptamer, glyphosate aptamer, and 1X TE buffer (10 mM Tris-HCl, 0.1 mM EDTA, pH = 8.0) were purchased from Integrated DNA Technologies (Coralville, IA). The glyphosate sequence is 5'-GGA-CAG-CTG-GCC-GCG-TAG-CGA-GAC-ACG-TAC-AAG-GTA-CTA-TAC-GGC-TGG-CAT-ATG-TAT-CTG-3'. The serotonin aptamer sequence is 5'-CTC-TCG-GGA-CGA-CTG-GTA-GGC-AGA-TAG-GGG-AAG-CTG-ATT-CGA-TGC-GTG-GGT-CGT-CCC-3'. Both aptamers were purchased with a 5' C_6 thiol linker and were desalted. Tris[2-carboxyethyl] phosphine (TCEP), hydrogen peroxide (30%), and anhydrous $CaCl_2$ were purchased from Thermo Fisher Scientific (Waltham, MA). 6-Mercapto-1-hexanol (MCH), 1-hexanethiol, adenosine 5'-diphosphate (ADP) sodium salt, L-tryptophan, dopamine hydrochloride, and γ-aminobutyric acid (GABA) were obtained from Sigma Aldrich (St. Louis, MO). Histamine was obtained from Alfa Aesar (Ward Hill, MA).

2.4 Electrode Patterning of FGTs

Wafers were patterned using photolithography and chrome photomasks. An electron beam evaporator (CHA SEC-600) was used to evaporate 5 nm of Cr followed with 50 nm of Au onto the patterned wafers. The positive photoresist (Microposit S1813 G2) was stripped off in a 1:1

volumetric ratio of acetone to isopropanol overnight (lift-off) further rinsed off with acetone and IPA, and dried with N_2. All wafers were stored in the glove box until use.

2.5 Aerosol Jet Printing of EGTs

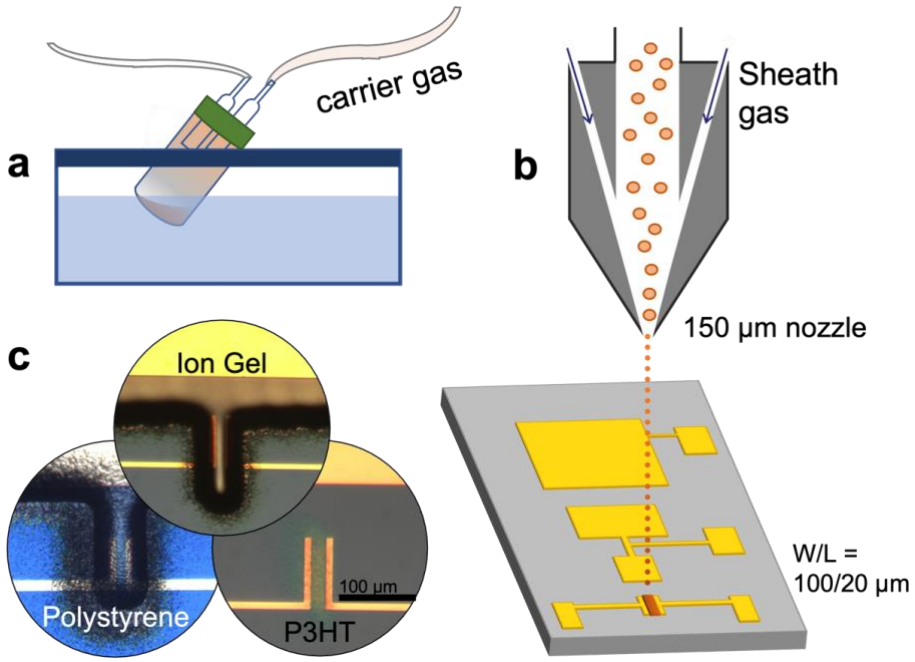

Figure 2.1. Aerosol jet printing. (a) A vial of ink immersed in an ultrasonic bath, producing an aerosol. The inlet tubing (clear) introduces N_2 gas while the outlet tubing (orange) contains both the aerosolized mist and the N_2 gas. (b) Cross-section of the deposition head. Sheath gas (N_2) is used to focus the carrier gas and aerosol as it exits the nozzle and prints between the source and drain of the FGT, creating the P3HT channel (100 x 20 µm). (c) Optical micrographs of printed P3HT, ion gel, and polystyrene.

An Aerosol Jet Printer 200 (Optomec, Inc) was used for aerosol jet printing, an additive process where materials are printed only where they are needed. A wide range of materials varying in viscosity can be printed, and printing parameters can be optimized to enable rapid prints with high stage speeds (several mm/s) onto rigid or flexible substrates.[32,96–99] In this work, the aerosol jet printing was used to print P3HT, ion gel, and polystyrene, completing EGT fabrication. Images

of printed materials and a general overview of aerosol jet printing is shown in Fig 2.1. The temperature of the atomizer bath was kept at 18 °C for all inks. The sheath gas was N_2 (99.999%). A fresh 1.0 mg/mL solution of P3HT in chloroform was prepared and stirred at 60 °C for 1 h before use. For printing, terpineol was added as a co-solvent (10% by volume). P3HT was printed with a 150 µm nozzle, a carrier gas flow rate of 10 sccm, and a sheath gas flow rate of 65 sccm, and the platen speed was adjusted to print an ~50 nm thick channel. The ultrasonic current for ink atomization was 250-260 mA. The thickness of the P3HT channel was estimated by the color of the channel. Color of the P3HT channel was correlated to thickness by measuring the height of several printed P3HT lines using a P16-Surface Profiler. Ion gel ink was prepared at a 1:9:90 ratio (by mass) of SEAS, [EMIM][TFSI], and ethyl acetate, respectively. The solution was stirred overnight at room temperature and stored at room temperature for multiple uses. Ion gel was printed with a 150 µm nozzle, a carrier gas flow rate of 25 sccm, and a sheath gas flow rate of 50 sccm. The ultrasonic current in the atomizer was 250-260 mA. A 5.0 mg/mL solution of polystyrene in chloroform was prepared and stirred at 60 °C for multiple uses. For printing, terpineol was added as a co-solvent (4% by volume). Polystyrene was printed with a 200 µm nozzle, a carrier gas flow rate of 45 sccm, and a sheath gas flow rate of 55 sccm. The ultrasonic current in the atomizer was 400-450 mA. After printing, all transistors were annealed in a N_2 glove box at 120 °C for 30 min. All transistors were stored in the glove box until use unless otherwise specified.

2.6 FGT Cleaning and Functionalization

Polydimethylsiloxane (PDMS) wells were used to ensure that solutions for functionalization and sensing only contacted key interfaces of the FGT device at different steps in

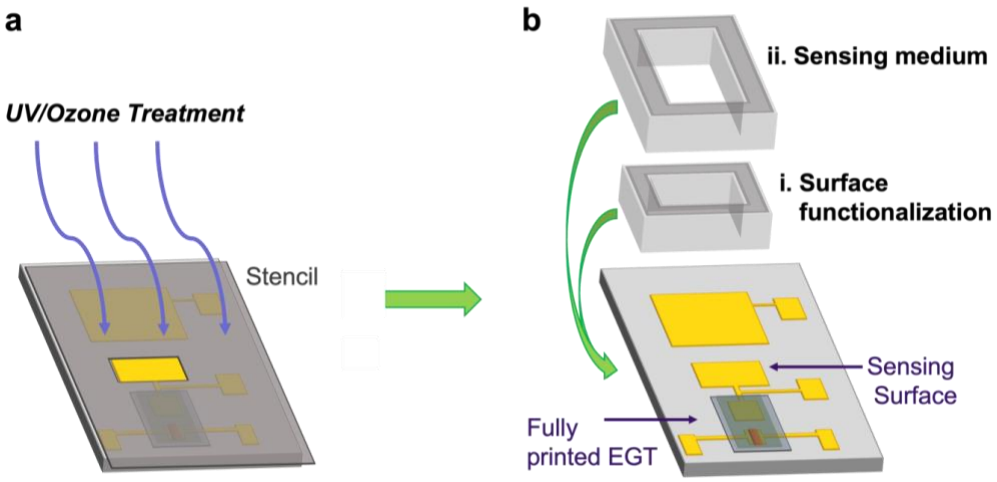

Figure 2.2. FGT sensor preparation. Schematic of sensing surface cleaning and functionalization protocol for FGT sensing. (a) Selective UV/ozone treatment of FG2 using a stencil. (b) PDMS wells used for (i) surface functionalization over FG2 and (ii) for containing the sensing medium over FG2 and CG.

the functionalization protocol (Fig 2.2). PDMS wells can be reversibly and irreversibly sealed to the SiO_2 interface, preventing leakage of solutions. A smaller well exposed the sensing electrode (FG2) to functionalization solutions, and a larger well exposed both the control gate and sensing surface to the aqueous electrolyte and sample solutions for sensing. The smaller PDMS well was reversibly bonded to a PDMS lid to prevent solvent evaporation for reaction times > 30 min. Subsequent steps for surface functionalization and rinsing were carried out in the same well. To prepare PDMS wells, the base and curing agent were mixed at a 10:1 volumetric ratio and mixed with an ARE-310 Planetary Centrifugal Mixer (Thinky USA, Laguna Hills, CA) at a speed of 2000 rpm for 5 min. The PDMS was poured onto a silicon wafer treated with trichloro(1H, 1H, 2H-perfluoro-octyl)silane (PFOTS) enclosed by an glass dish to ensure easy delamination from the wafer and low surface roughness. The PDMS was cured in an oven at 60 °C for 4 h. PDMS wells were cut with a razor blade by hand, pressed onto double-sided tape to remove any debris from the surface, removed from the tape, and reversibly bonded to the substrate.

2.7 X-ray Photoelectron Spectroscopy (XPS)

XPS spectra were collected using a PHI 5000 Versa Probe III XPS system (ULVAC-PHI) equipped with a monochromic Al K_α X-ray source (1486.6 eV). The base pressure was 3.0×10^{-8} Pa. The beam spot size was 100 µm with a power of 25 W under 15 kV. The survey scans were taken with a 280 eV pass energy and 1 eV step size. The high-resolution scans were taken with a 55 eV pass energy and 0.05 eV step size. The sample was mounted on a piece of carbon tape onto a sample holder and grounded with conductive tape to the sample holder. MultiPak software was used to fit peaks to high-resolution spectra using a Shirley background subtraction method. All peaks were referenced to the Au_{4f} (7/2) peak at 84.0 eV.

2.8 Reflection-Absorption Infrared Spectroscopy (RAIRS)

Infrared spectra were collected using a Thermo Scientific Nicolet iS50 FTIR spectrometer equipped with a Harrick Seagull accessory for grazing-angle specular reflectance measurements. The p-polarized IR beam was 86° from the surface normal. The resolution was 2 cm^{-1}. Substrates were approximately 1 x 5 cm in area. A bare Au substrate was used for background subtraction. The functionalized substrate was purged in a dry air chamber for 15 min prior to scanning. A total of 1500 scans were collected and averaged. Subsequently, the bare Au substrate was placed on the sample stage in the chamber and left to purge 10-15 min before the measurement. The background was continuously subtracted from the sample spectrum until noise from H_2O bands in the carbonyl region was minimized, at which point the spectrum was saved.

2.9 Epifluorescence Microscopy

Cy5 fluorescently labeled IgY antibodies conjugated to gold were imaged with an epifluorescence microscope (Leica DMI 4000B) equipped with a Coolsnap EZ camera (Photometrics, Tucson, AZ) and Cy5 filter. The substrate was placed face-down onto a cover slip directly over a 100x, 1.4 NA oil immersion objective. All images were acquired with Micro-Manager software and processed with ImageJ.

2.10 Cyclic Voltammetry (CV)

CV measurements were conducted with a CHI660 electrochemical workstation (CH Instrument, InC, Austin, TX) or Pine WaveDriver 40 DC Bipotentiostat/Galvanostat (Durham, NC) in a three-electrode cell system (Ag/AgCl saturated in 3 M KCl as the reference electrode, platinum wire with platinum mesh as the counter electrode, and gold substrate as the working electrode). Gold substrates were patterned using photolithography as previously discussed (5 nm Cr/50 nm Au on SiO_2 wafers). The electroactive species was 10 mM $K_3[Fe(CN)_6]$ in 1X PBS (0.2 µm filtered, pH = 7.4) electrolyte solution. The CV sweep rate and potential window were varied. The sample interval and quiet time were 1 mV and 2 s, respectively. No contact was made with the SiO_2 substrates of the working electrode, as this would lead to quick electrochemical dissolution of the gold electrode. All files were processed with a custom-made Python script.

Chapter 3. Reconsidering Parasitic Capacitance in FGTs and Optimizing EGT Operation*

3.1 Introduction and Motivation

Despite its demonstrated use as a platform for biosensing, the FGT was restricted by its architecture to fully translate the perturbations at the sensing surface to the EGT. An understanding of how the FGT architecture, particularly, the sizing of the floating gate electrodes, revealed how the device can be constructed to prevent potential losses between each of the four interfaces. This previous work had constructed the argument that FGTs face limitations due to parasitic effects.[41] As the area of the sensing surface, FG2, is decreased, the threshold voltage, V_T, became increasingly more negative to that measured for the EGT of the same device. Specifically, the gate voltage applied at the control gate, V_G, was unable to fully modulate the P3HT channel conductivity, as potential was lost to differences in capacitance and to lost charge. The fraction charge lost, f, from the sensing surface to the EGT was experimentally estimated by White et al. as 0.77.[41] This fraction of lost charge was hypothesized to stem from a capacitance (C_{paras}) formed between the floating gate and the p-doped silicon substrate underlying the 300 nm SiO_2 and, in turn, forced constraints on the sizing of the device.[41] Such parasitic losses were avoided by oversizing FG2, but for the purposes of biosensing, this limits the sensitivity of the device, as more molecular binding events must occur across the electrode to elicit a large change in C_2 for capacitance-based sensing.

*Portions of this chapter are reprinted (adapted) with permission from Thomas, M.S.; Adrahtas, D.Z.; Frisbie, C.D.; and Dorfman K.D. Modeling of Quasi-Static Floating Gate Transistor Biosensors, *ACS Sensors* **2021**, *6* (5), 1910-1917. Copyright 2021 American Chemical Society.

In this chapter, we further investigate the sources of potential losses between the two electrolytes in order to remediate losses and provide a means to better design FGTs for capacitance- and charged-based detection. We repeated the experiments and analysis done to extract f in ambient air, instead of the N_2 glove box, by measuring the transfer curves of FGTs with varied areas of FG2 (A_{FG2}) and their EGT-subunits. Initially, a fused silica (glass) substrate was also used in order to challenge the inclusion of C_{paras}, or f, in FGT models. The extracted value of f for glass (0.41) was larger than SiO_2 FGTs (0.32), prompting an investigation into other factors for potential loss. As specific capacitances also play a role in the coupling between the two electrolytes, the specific capacitance of the P3HT/ion gel interface was measured, adding uncertainties to $C_{i,\ P3HT}$. As such, the uncertainties of the ion gel/gold interface were also considered. In implementing uncertainties of these essential capacitances and using a new model to understand FGT operation built on the change on the slope of transfer curves rather than V_T, f was eliminated from our FGT models.

This chapter also considers the short- and long-term operation of EGTs, where EGTs remained operable for FGT sensing after 28 days in an ambient, dark environment and 6 months in an inert, dark environment. However, changes in the environment, such as humidity, were shown to have a significant impact on EGT electrical characteristics. Finally, the EGT was shown to operate with sweep rates at high as 150 mV/s.

3.2 Experiments

FGTs were fabricated with photolithography and aerosol jet printing, as described in Sections 2.4 and 2.5, respectively. The second compartment of the FGT was printed over with ion gel electrolyte instead of using an aqueous buffer for capacitive coupling. Fabrication was the same

on fused silica glass substrates. The dimensions of the P3HT channel were 100 µm by 20 µm, and the target area of the P3HT channel was 100 µm by 30 µm. The area of FG1 was 0.003 cm^2 (A_{FG1}/A_{P3HT} = 100). The area of FG2 was varied: A_{FG2}/A_{P3HT} = 1000, 600, 400, 200, 100, and 50. The dimensions of CG were kept at 3.2 mm by 3.2 mm. Due to assessing the thickness of printed P3HT lines by color, P3HT was printed over the glass EGT channels immediately after printing the SiO_2 EGT channels with the same printing parameters.

Transfer curves for parasitic capacitance studies were measured with a LabVIEW program. The drain voltage (V_D) was sourced with a Keithley 2611 source-measure unit. The gate voltage (V_G) was sourced and gate current (I_G) was measured with a Keithley 2400 source-measure unit. The source electrode was grounded. All transfer curves were measured with an initial hold of the starting gate voltage for 3 s to polarize the ion gel electrolyte, sweep rate of 25 mV/s, a V_G step size of 50 mV, and V_D = –0.5 V. Each device was swept several (3-4) times until consecutive sweeps overlapped, producing a stable transfer curve. Displacement current measurements were taken with a Keithley Test Script Builder program which utilized the Keithley 2612B for V_G sourcing and I_G measurement. The drain and source electrodes were grounded, while V_G was applied to the floating gate. Optical micrographs of the printed P3HT channel were taken, and the area of the channel was measured using ImageJ.

To measure the inverter curves, a custom-made Python program was used. V_G and I_G were sourced and measured, respectively, with a Keithley 2612B source-measure unit (channel B). The drain voltage (V_{DD}) was sourced with a Keithley 2611 source-measure unit across the transistor and over a load resistor (1 MΩ). The output voltage (V_{OUT}) was measured at the drain electrode with a Keithley 2612B source-measure unit (channel A). The source electrode was grounded.

Inverter curves were measured with a sweep rate of 100 mV/s, V_G step size of 10 mV, and V_{DD} = –0.5 V. V_G was swept from the OFF state to the ON state and back.

3.3 Results and Discussion

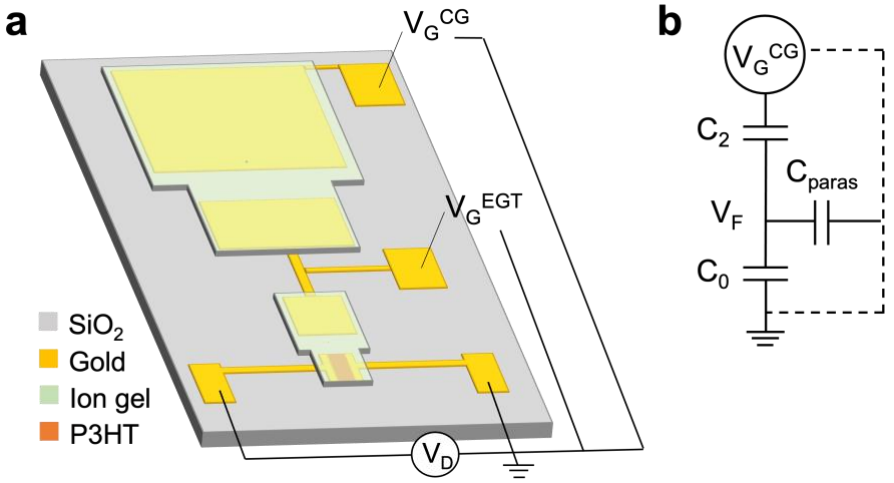

Figure 3.1. Schematic representation of FGT with parasitic capacitance. (a) Printed FGT with V_G applications for EGT (V_G^{EGT}) vs FGT (V_G^{CG}) operation. (b) Equivalent circuit of an FGT considering parasitic capacitance.

The extension of the floating gate and addition of CG can be modeled as two additional capacitors (from EDL formation) in series with the EGT. In order to make the EGT sensitive to changes in capacitance and interfacial charge at FG2, the area of CG is intentionally oversized in order to neglect its capacitance (C_{CG}) in the sensing medium, or secondary electrolyte.[41] This can be understood by expressing the capacitor in series,

$$\frac{1}{C_2} = \frac{1}{C_{i,\text{ion gel/gold}} A_{FG2}} + \frac{1}{C_{i,\text{ion gel/gold}} A_{CG}} \tag{2.1}$$

where $C_{i,\text{ion gel/gold}}$ is the specific capacitance of the ion gel/gold interface. The electrodes continue to decrease in area, schematically shown in Fig 3.1. Following the same implications of Eq. 2.1, the capacitance of the EGT is estimated as C_0 since due to the oversizing of FG1 to prevent

potential loss between FG1 and the P3HT/ion gel interface. The charge stored in a capacitor is the product of the capacitance and voltage, which, in this case, is expressed as

$$Q_0 = C_0(V_F - 0) \tag{2.2}$$

where the potential of the floating gate, V_F, is dropped at the P3HT/ion gel interface during operation when the source is grounded. The charge stored in the secondary electrolyte should be equal and opposite to the charged stored in the primary electrolyte, in order to satisfy the charge balance: $Q_2 + Q_0 = 0$. Yet, between FGT and EGT transfer curves of the same device exist discrepancies, which are observed as changes in the effective gating of the device as expressed by the following equation,[41]

$$\Delta V_T = V_G^{CG} - V_G^{EGT} = \left(\frac{1}{1-f}\frac{C_{i,P3HT}A_{P3HT}}{C_{i,FG2}A_{FG2}}\right) V_G^{EGT} \tag{2.3}$$

The fraction charge lost from C_2 to the floating gate is defined as f, and this loss led to decreased gating from the control gate to the EGT. The first approach to minimize or eliminate parasitic capacitance was to change the substrate to fused silica, or glass, an insulating material. As previously done by White et al., the parasitic effects can be amplified by decreasing A_{FG2} and comparing the changes in V_T to fit a value of f to the model (Eq. 2.3).[41] Alongside this, the same experiments were carried out on SiO_2/Si wafers in order to verify previous work and to ensure the device fabrication procedures were consistent.

In order to calculate V_T for each device in EGT and FGT mode, Eq. 1.3 can be rearranged to extract V_T. As V_G was swept more negatively for both EGTs, I_D increased by several orders of magnitude (I_{ON}/I_{OFF} ~ 10^5 to 10^6), as observed in Fig 3.2. The linear regression of the $|I_D|^{1/2}$–V_G plot where the device is in its ON state results in V_T as the x-intercept. The linear regression was done on the forward sweep for consistency, as some devices exhibited hysteresis. The average V_T

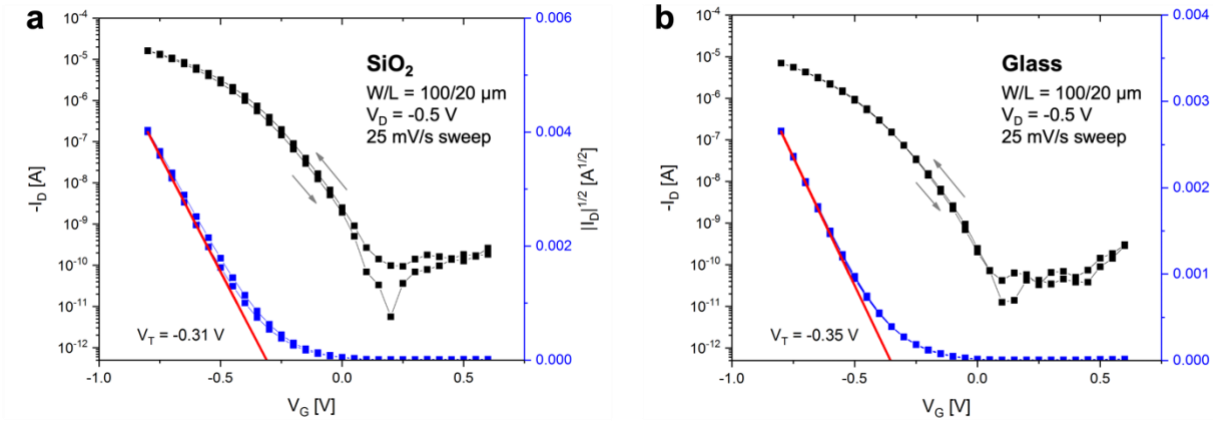

Figure 3.2. EGT transfer curves. Transfer curves on a semi-log scale (black) and linear $I_D^{1/2}$ vs V_G plots (blue) of (a) SiO_2/Si and (b) glass EGTs. Gray arrows indicate the direction of the forward and backward sweeps, starting from positive V_G. The x-intercept of the red linear regression is V_T.

among 30 SiO_2 EGTs and 32 glass EGTs was –0.30 ± 0.06 V and –0.31 ± 0.09 V, respectively. The difference between V_T of the FGT and EGT-subunit was used for the fit using Eq. 2.3 (Fig 3.3). The values for the specific capacitance of each electrolyte were chosen based on previous experimental work, being 12.5 µF/cm^2 and 100 µF/cm^2 for $C_{i,\ ion\ gel/gold}$ and $C_{i,\ P3HT/ion\ gel}$, respectively.[33,41] The estimated values for f, according to this set of experimental data, were 0.32 and 0.41 for SiO_2 and glass devices, respectively.

Both sets of experimental data were fit to Eq. 2.3 with the exception of A_{FG2}/A_{P3HT} = 400 due to its larger change in V_T that did not follow the trend. Changes in V_T are expected with decreasing A_{FG2}, even when f = 0, due to differences in capacitance, as modeled by the gray line in Fig 3.3. Devices had nearly no change in V_T for large areas of FG2, but as the area decreased, there were changes in I_D–V_G characteristics between EGT and FGT modes. Smaller-area FG2 devices had lower dI_D/dV_G, as evident by the smaller slope, indicating less capacitive coupling between the two ends of the floating gate as more negative V_G must be applied to achieve similarly

high I_D. Based on the current data set, the use of glass substrates does not eliminate nor lower parasitic capacitance. In fact, the value of f was higher for glass than for SiO_2 devices. The slopes of the linear regressions for glass devices were consistently lower than SiO_2 devices and can be attributed to differences in P3HT film thickness and morphology.

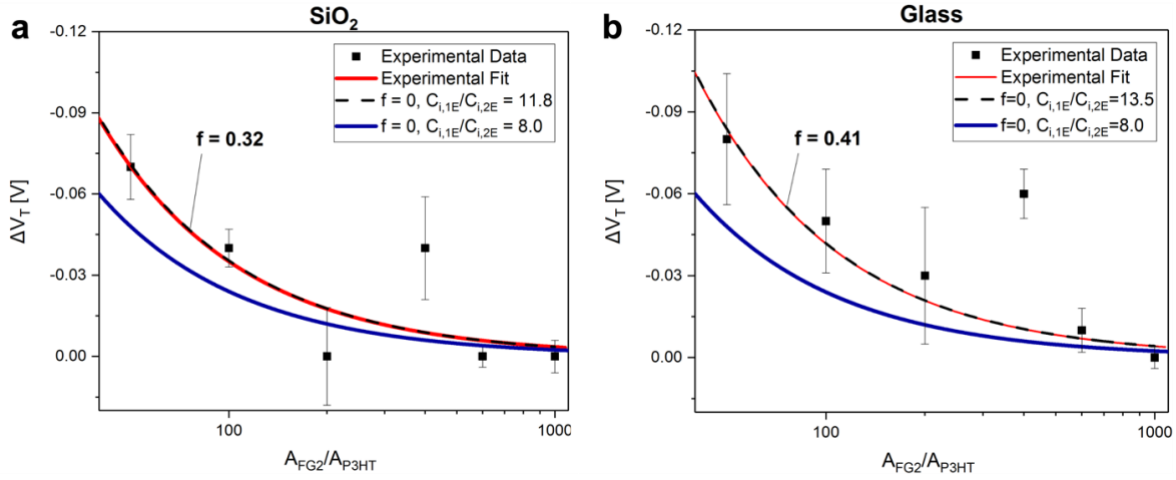

Figure 3.3. Area dependence of FG2 on FGT and EGT operation. Semi-log plot for (a) SiO_2/Si and (b) glass substrates show changes in V_T between the FGT and EGT modes as function of A_{FG2}/A_{P3HT}. The curves fit the experimental data using Eq. 2.3 where blue and gray curves are representative of no fraction of charge (f) lost at the floating gate for $C_0/C_2 = 8$ and a value of C_0/C_2 set to fit the experimental data (11.8), respectively. The red curve estimates, using $C_0/C_2 = 8$, that $f = 0.32$ for SiO_2 FGTs and $f = 0.41$ for glass FGTs. Each data point and error represent the average and standard deviation of 5 devices, respectively. $A_{FG2}/A_{P3HT} = 400$ was excluded from the fits.

A second fit is shown in Fig 3.3 where the ratio of capacitances is changed to fit the experimental data by multiplying by $1/(1-f)$. This fit suggests that, instead of parasitic capacitance affecting the device output, the estimations for the specific capacitances are not correct. Since the P3HT channel is permeable, it's specific capacitance is not only reliant on its area but also its thickness. Variations in printing can result in such variability in P3HT capacitance. To assess this, a set of devices' specific capacitances was measured in order to determine

variability. Displacement current measurements were used to estimate $C_{i,\,P3HT/ion\ gel}$ (Fig A.1), finding the P3HT/ion gel specific capacitance to be 209 ± 25 μF/cm^2 among 10 EGTs.

As f was not eliminated with glass substrates, we look toward other approaches using our experimental data to model the relationship between the gating of the FGT and EGT-subunit. By modeling the system as capacitors in series, the fraction of the applied V_G at the control gate can be modeled as

$$\kappa^f = \kappa_{EGT}\kappa^f_{CG} \tag{2.4}$$

Here, κ^f is expressed as two multiplicative factors, where κ_{EGT} is the intrinsic potential drop over the EGT, or primary electrolyte, and κ^f_{CG} is the potential drop over the secondary electrolyte along with the parasitic loss, f. The I_D-V_G relationship for FGT operation in the saturation regime can thus be expressed as[21]

$$I_D^{1/2} = \left(\frac{\mu C_i W}{2L}\right)^{1/2}\left(\kappa^f V_G - V_T\right) \tag{2.5}$$

where the potential effectively felt by the P3HT channel is $\kappa^f V_G$. To extract a value for f, we can rearrange the model for κ^f_{CG} where

$$\frac{1}{\kappa^f_{CG}} = \frac{(C_0\ C_1)}{C_2(1-f)(C_0 + C_1)} + 1 \tag{2.6}$$

enables varying C_2, or A_{FG2}, while maintaining C_0 and C_1, to extract f. Following Eq. 2.4 and Eq. 2.5, the slope of the transfer curve in the saturation regime of the FGT, $(\mu C_i W/2L)^{1/2}\kappa^f$, can be divided by the slope of the same device operating as an EGT, $(\mu C_i W/2L)^{1/2}\kappa_{EGT}$, resulting in a measured value of κ^f_{CG}.

To test our newly derived model, we first determined ion gel-gold and P3HT-ion gel capacitances from literature or experiments. A previous report found the specific capacitance of

the ionic liquid used, [EMIM][TFSI], on gold to be approximately 8 μF/cm^2 at low frequencies (10 Hz),[100] while quasi-static measurements have yielded 12.5 μF/cm^2.[33,95] We hence assigned a value of 8 ± 4 μF/cm^2 to represent the uncertainty in $C_{i,\text{ ion gel/gold}}$, yielding C_1 = 24 ± 12 nF. We used the value of $C_{i,P3HT/\text{ion gel}}$ measured here, 209 ± 25 μF/cm^2, and the value reported in previous work, 100 μF/cm^2,[41] to set values for C_0 as 6.27 (± 0.75 nF) and 3 nF, respectively. Uncertainties in specific capacitance can potentially reflect surface contamination by organics, varied thickness of the ion gel electrolyte or P3HT channel, and/or moisture from humidity.[101]

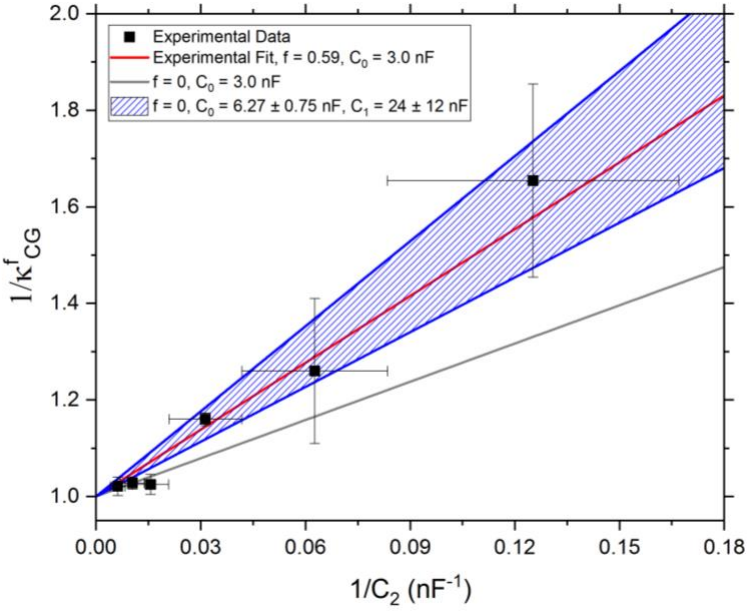

Figure 3.4. Model of $1/\kappa^f_{CG}$ vs 1/C2 to extract *f*. The inverse of measured κ^f_{CG} against the inverse of the corresponding value of C_2 using Eq. 2.6. The blue region reflects the range in $C_{i,\text{ion gel/gold}}$ (8 ± 4 μF/cm^2) for C_1 and the uncertainty in $C_{i,P3HT/\text{ion gel}}$ for C_0 with the presumption of no charge lost, or f = 0. Both the red and gray fits reflect $C_{i,P3HT/\text{ion gel}}$ = 100 μF/cm^2, where the grey fit assigns f = 0. A total of 5 devices were measured for each data point. Error in C_2 is based on the range of values for $C_{i,\text{ion gel/gold}}$. Reprinted (adapted) with permission from Thomas, M.S.; Adrahtas, D.Z.; Frisbie, C.D.; and Dorfman K.D. Modeling of Quasi-Static Floating Gate Transistor Biosensors, *ACS Sensors* **2021**, *6* (5), 1910-1917. Copyright 2021 American Chemical Society.

The inverse of the experimentally obtained values of κ_{CG}^{f} are plotted against the inverse of C_2 in Fig 3.4 in order to extract f by fitting the data to Eq. 2.6. In assigning the originally used values of 100 μF/cm^2 for $C_{i,P3HT/ion\ gel}$ and 5.33 μF/cm^2 for $C_{i,ion\ gel/gold}$, the fit yields $f = 0.59$ (red). Alternatively, by assigning $C_{i,P3HT/ion\ gel} = 209 \pm 25$ μF/cm^2, $C_{i,ion\ gel/gold} = 8 \pm 4$ μF/cm^2, and $f = 0$ (blue range) the red experimental fit falls within the uncertainty range, indicating that the new equivalent circuit model is sufficient in explaining the experimental data. This result indicates that rather than having parasitic losses, the differences in capacitance at each interface lead to perceived excess losses in capacitive coupling from the control gate to the P3HT channel. FGT models for charge- and capacitance-based sensing based on experimental data were further developed without consideration of f.[21] We also find how sensitive these interfaces are to FGT operation, lending greater attention to the fabrication and measurement protocols.

3.4 Optimizing the EGT as a Signal Transducer

Based on the results in Section 3.3, it was evident that the EGT device properties may be sensitive to experimental protocols, such as electrode cleanliness, thickness of printed materials, and the operating environment. A strategy already implemented to limit interactions between the ion gel and semiconductor with the environment is the use of a poly(styrene) (PS) encapsulation layer printed on top of the ion gel encompassing the source, drain, and FG1 electrodes. The purpose of the PS encapsulation layer is to extend the lifetime and decrease the inherent variability of the device by reducing its interaction with the air. Continuous exposure to oxygen and humidity can result in a reduction of P3HT conductivity and hole transport as oxidation occurs.[102] As the conductivity is linearly related to the mobility of the semiconductor at a specific electric field, there would be continuous decreases in the transconductance with degradation. Such a result was

noted in the case of the ion gel, where SEAS, a more hydrophobic polymer, used in ion gel led to more air-stable EGTs compared to the use of poly(styrene-b-ethylene oxide-b-styrene), or SOS, in ion gel.[95]

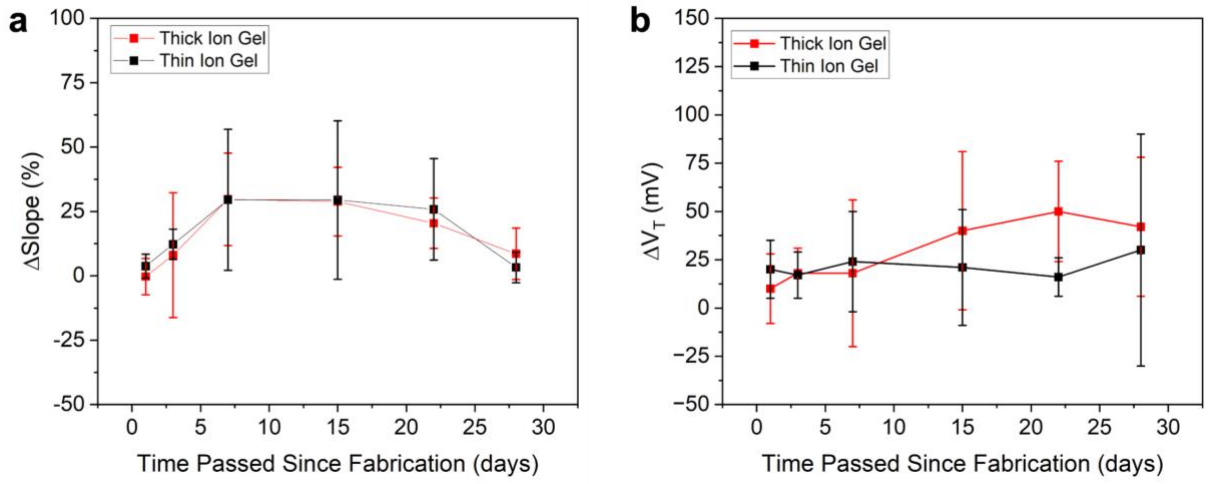

Figure 3.5. EGT transfer curve characteristics over 28 days in ambient air. Changes in (a) the slope of the $I_D^{1/2}$ vs V_G fit for V_T, $(\mu C_i W/2L)^{1/2}$, and (b) V_T. EGTs were printed with thin and thick layers of ion gel and encapsulated with polystyrene. The error represents the standard deviation of 5 devices.

EGTs were printed with both thick and thin layers of ion gel before encapsulation to study how ion gel thickness may also act as a barrier to P3HT over time. The thicknesses of ion gel were solely qualitative. The devices in this study were stored in the dark in ambient air between measurements. Changes in the electrical characteristics of EGTs were monitored over 28 days (Fig 3.5). The fit used to calculate V_T has a slope of $(\mu C_i W/2L)^{1/2}$, where changes to the slope indicate changes in the P3HT mobility or P3HT/ion gel specific capacitance. Nearly all devices had a change in slope that increased from 3 days to 7 days, then decreased after 28 days, indicating that an external factor was affecting device properties. The slope did not continuously decrease over time, as expected for a P3HT device that is degrading. As such, the variability can instead be attributed to changes in the specific capacitance. This result aligns with our earlier data that

suggests there is variability in the specific capacitance of the ion gel interfaces. Ultimately, over the month, thick ion gel EGTs exhibited a maximum threshold voltage shift of 70 mV while thin ion gel EGTs exhibited a maximum threshold voltage shift of 100 mV. PS does completely protect the EGT from the air, as noted by varied device performance. Variability in measuring the same device has been overcome by sweeping the device until consecutive transfer curves overlap, making it unlikely that instability could be responsible for the trend. Because EGTs with thick ion gel exhibited lower hysteresis than those with thin ion gel, we proceeded with printing thick layers of ion gel for all EGTs.

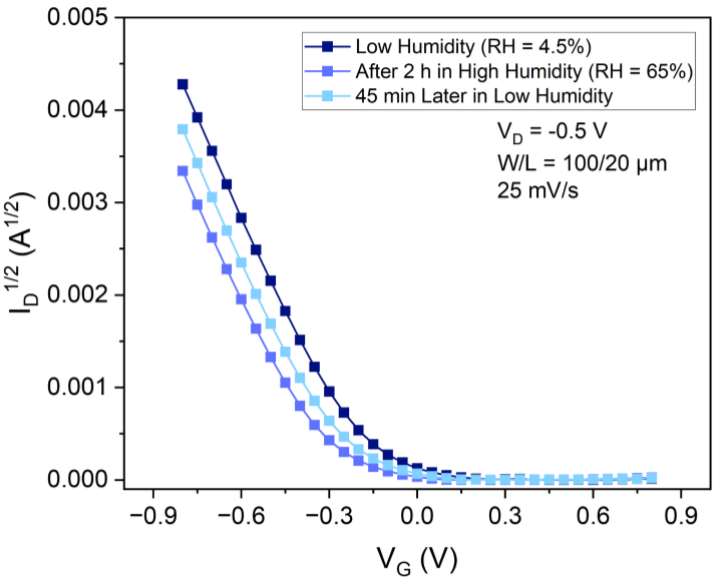

Figure 3.6. Effect of high humidity on EGT. The transfer curve of the EGT was initially measured in a low humidity (r.h. = 4.5%) environment (blue). After 2 h in a high humidity (r.h. = 65%), the curve (red) shifted to a more negative V_G. Stabilization in the low humidity environment for 45 min led to the curve (purple) shifting positively back toward its initial state.

A simple test of measuring the same device inside and outside the glove box (< 0.1 ppm O_2) provided sufficient evidence that the humidity and/or oxygen affect EGT electrical characteristics by shifting the transfer curve to a more positive V_G in ambient air. Further, after incubation in a high humidity chamber (r.h. = 65%), the transfer curve shifted positively compared to the low

humidity environment (r.h. = 4.5%), retreating back toward its initial state with time (Fig 3.6). Among four devices, the average shift in V_T after 2 h in the high humidity environment was –47 ± 17 mV, and the average change in slope was 1.2 ± 2.6%. This result resembles previous report by Li et al. observed for p-type organic thin film transistors (OTFTs), where the device performance worsens within a high humidity environment (lower I_{ON}/I_{OFF}).[103] However, the retreating of the transfer curve as it adjusted to the low humid environment suggests the effect is reversible, where water molecules likely diffuse out of the ion gel as it equilibrates. With this, other encapsulants that provide a barrier to water diffusion should be explored in order to protect the EGT from changes in humidity for long-term signal transduction use. Otherwise, the FGT response must be calibrated to the state of the EGT for use in ambient air.

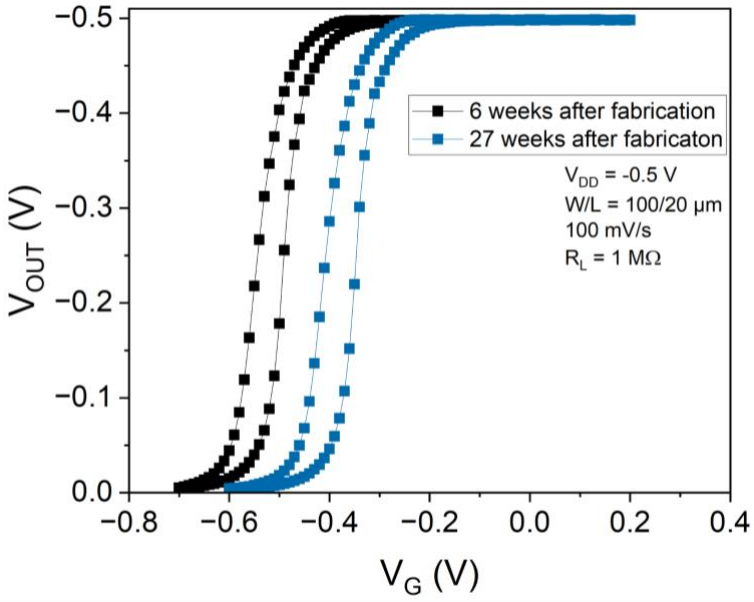

Figure 3.7. EGT inverters after 27 weeks in the glove box. Operation of an EGT inverter after storage in the glove box for 6 weeks (black) and 27 weeks (blue) after fabrication.

For storage purposes, the longevity of an EGT was also investigated. EGTs, in the inverter configuration, continue to operate within low potential windows despite being stored in the glove

box 6 months after fabrication (Fig 3.7). Shifts in the inverter curves are not surprising based on the shifts humidity can cause, and the average change in gain among three EGTs was 0.7 ± 2.1%. As a result, EGTs can be fabricated in mass and subsequently stored in the glove box, saving unused materials for printing and time for solution preparation and annealing.

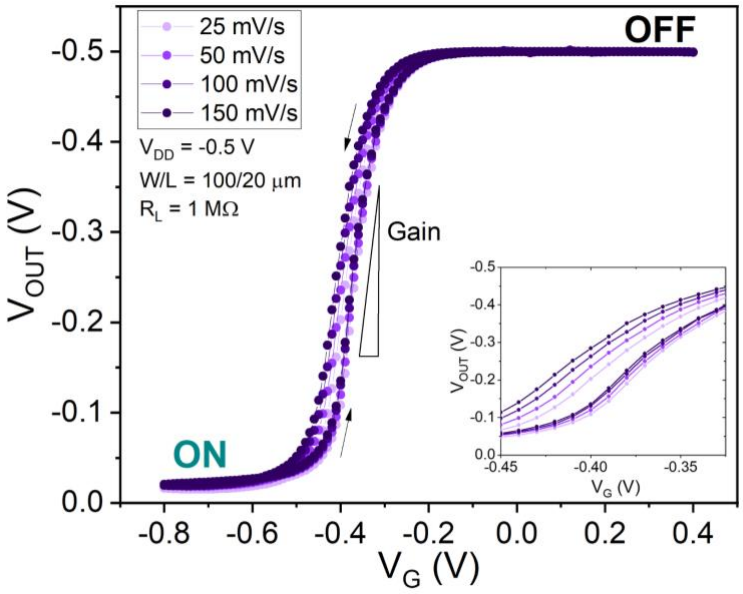

Figure 3.8. EGT inverter with varied sweep rates. The sweep rate was increased from 25 mV/s to 150 mV/s. The inset shows the impact on inverter hysteresis. Arrows indicate the direction of the forward and backward sweep, starting from the OFF state.

The inverter curve measurement program was further optimized, allowing for sweep rates up to 150 mV/s. Fig 3.8 exemplifies how EGT inverter curves respond to changes in the sweep rate from 25 mV/s to 150 mV/s. The hysteresis of the device systematically increased with increasing sweep rate, as expected for devices utilizing ion gels. Among three devices, the hysteresis from 25 mV/s to 150 mV/s increased by a factor of ~2. We also note that the gain of the backward sweep, taken by running a linear regression between V_{OUT} = 0.15 and V_{OUT} = 0.35 V, was larger than the forward sweep. In this example, the gain of the forward and backward sweep

at 50 mV/s were 3.6 and 4.1, respectively. As the gain is proportional to the signal amplification, we chose to use the backward sweep of inverter curves for signal processing in sensor work in this thesis.

3.5 Conclusion

The fraction of charge lost, f, in FGTs was previously interpreted as parasitic capacitance between the underlying p-doped Si wafer and gold electrodes, as charge balance models did not account for the full potential loss between the two electrolyte compartments. Experiments were replicated in ambient air, leading to charge loss being understood as uncertainty in specific capacitances at key interfaces: P3HT/ion gel (209 ± 25 μF/cm^2) and ion gel/gold (8 ± 4 μF/cm^2). FGTs were constructed with ion gel as the secondary electrolyte for the FG2 and CG interfaces on both glass (insulating) and SiO_2/Si substrates. Glass FGTs presented similar losses (f = 0.41) compared to SiO_2 FGTs (f = 0.32) measured in ambient air. Models were reconstructed to represent the potential differences between the applied potential, V_G, and the final potential felt by the channel ($\kappa^f V_G$) through changes in the slope of the $I_D^{1/2}$ vs V_G curves, $(\mu C_i W/2L)^{1/2}\kappa^f$ for the FGT. Further, by introducing uncertainty to the specific capacitances in the model, the estimated capacitances were sufficient to model the response of FGTs with descending A_{FG2} without inclusion of f. With this, new models, excluding f, have been developed to predict the EGT inverter behavior and FGT inverter response to charge- and capacitance-based perturbations.[21]

The use of EGTs as signal transduction elements was also explored. EGTs can be stored as long as 6 months in the glove box and 28 days in ambient air for use without detriment to the transconductance/gain, enabling long-term storage. EGTs can be swept up 150 mV/s with a ~2x increase in hysteresis, providing faster signal transduction for quasi-static operation. Finally, EGTs

were observed to shift in V_T due to changes in humidity with negligible changes in the $I_D^{1/2}$–V_G slope. As such, the day-to-day operation of EGTs change, as indicated by observing changes in V_T and slope over 28 days in ambient air, raising a need for EGT calibration in the case on long-term, continuous FGT sensing.

Chapter 4. Designing an Antibody-based FGT Toward Small Molecule Detection

4.1 Introduction and Motivation

Of the different classes of analytes, small molecules are challenging because their size limits the ability to cause capacitance-based perturbations for FGTs equipped with rigid capture agents. A charged, small molecule of interest for food safety and environmental monitoring is glyphosate (169.07 Da, 2– charge at pH = 7.4).[104] Glyphosate, shown in Fig 4.1, is the active ingredient in the herbicide, Roundup® and has had a dramatically increased use worldwide since 2000.[79] Global consensus on the public and environmental health risk of glyphosate has yet to be established, with the International Agency for Research on Cancer concluding it may be a carcinogen and the Joint Food and Agriculture Organization (FAO)/World Health Organization (WHO) Meeting on Pesticide Residues (JMPR) concluding it is unlikely to be a carcinogen.[105] According to the US EPA Code of Federal Regulations (CFR), tolerances for glyphosate residues, including its metabolites and degradates, have been established for over one hundred products with varied limits in parts per million (0.1 – 400 ppm).[106]

Compliance is currently determined by measuring the concentration of glyphosate in a sample,[106] relying on complex analytical instrumentation such liquid chromatography mass spectrometry (LC-MS).[79,107] An in-house and simple-use detection method can be beneficial, as not all facilities can afford the time and cost of current detection methods.[79] Although electrochemical sensors have shown proof-of-principle studies that provide these advantages, other figures of merit such as sensitivity, reproducibility, and selectivity (without sample

preconcentration) inhibit their use in the field.[79] Within the past couple of years, electrochemical biosensors have achieved detection of glyphosate using electrochemical impedance spectroscopy and chronoamperometry for both antibody-based and aptamer-based sensors.[108–111] Each of these sensors elicits changes in capacitance upon glyphosate capture rather than potentiometric changes.

Detection of glyphosate with an FGT would expand the library of detectable analytes toward small molecules. To date, the FGT biosensor has been deployed to detect large biomolecules, including proteins[27,28] and DNA.[42] The low molecular weight and charge associated with small molecules limit electronic perturbations at the sensing surface, making small molecules challenging to detect with the FGT biosensor. Antibody-based FGT detection has been previously achieved for the gluten in an extraction cocktail (250 mM 2-mercaptoethanol, 2 M guanidine HCl),[27] demonstrating the FGT's ability to transduce signals antibody-target binding events in high electrolyte strength solutions.

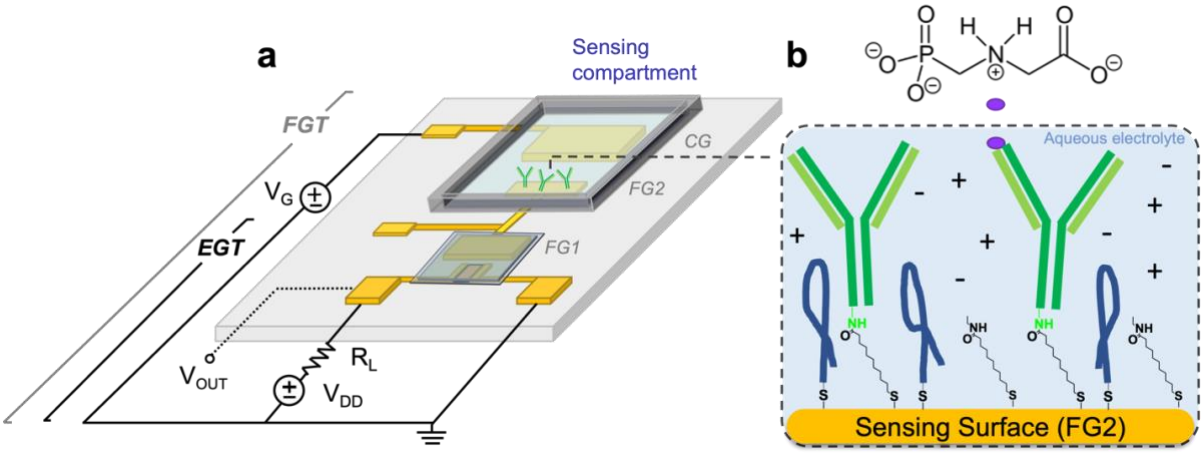

Figure 4.1. Diagram of the glyphosate FGT biosensor. (a) Schematic of the device, outlining the inverter configuration and sensing compartment. The FGT (gray bracket) includes the control gate, upper end of the floating gate, and EGT inverter (black bracket). (b) The schematic magnification of FG2 depicts the functionalized sensing surface composed of surface-bound antibodies after glyphosate binding.

As such, an electrode functionalized with antibodies was utilized in conjunction with FGT models[21] to design the sensor toward charge-based sensing with an antibody-conjugated sensing surface (Fig 4.1). As the presence of the antibody on the sensing surface is essential to biosensing, a thorough assessment of surface chemistries for antibody conjugation and subsequent surface characterization was done using X-ray photoelectron spectroscopy (XPS), reflection-absorption infrared spectroscopy (RAIRS), cyclic voltammetry (CV), and epifluorescence microscopy (detailed in Section 2). After confirming the conditions for antibody conjugation, the surface chemistry was translated to the floating gate using PDMS wells. Initial controls were done to measure the response to 0.1 – 100 μM glyphosate in 1X PBS over 10 min for bare gold and PEG-thiol FGTs which did not exhibit dose-dependent responses. Glyphosate FGT biosensors elicit responses to 100 μM glyphosate that are on average low and irreproducible, prompting an assessment of the binding constant (K_D) of the glyphosate antibody with surface plasmon resonance (SPR). While SPR validated conjugation of the antibody to the chip, glyphosate-antibody binding was undetectable despite varying the running buffer and antibody conjugation protocol to alleviate possible electrostatic or pH effects.

4.2 Experiments

Surface functionalization was initially characterized on a control substrate. A home-built thermal evaporator housed in a glove box was used to evaporate 5 nm of Cr and 50 nm of Au onto silicon substrates. The gold control electrodes were cleaned with UV/ozone treatment for 20 min and immersed in ethanol for 40 min. Before immersion in the 1 mM thiol solution in ethanol, the substrates were rinsed thoroughly with ethanol and dried with N_2. Thiol solutions containing 11-MUA were prepared with 10% HCl in order to prevent a bi-layer of 11-MUA through hydrogen

bonding of the carboxylic acid groups.[112] The substrate was stored in a vial at room temperature in the dark. Incubation times for self-assembly were varied for initial XPS studies but led to a final incubation time of 20 h. After incubation, the substrate was thoroughly rinsed with HPLC water and ethanol and dried with N_2. The substrate was then immersed in a 100 mM 2-(N-morpholino)ethanesulfonic acid (MES) buffer (pH = 5.8) containing 50 mM N-hydroxysuccinimide (NHS) and 200 mM 1-ethyl-3-(3-dimethylaminopropyl)carbodiimide HCl (EDC) solution for 30 min, reacting with carboxylic acid of 11-MUA to yield a succinimidyl ester (NHS ester) tail group. The substrate was rinsed with MES buffer and HPLC water and dried with N_2. A 5.0 mg/mL glyphosate antibody aliquot was brought to room temperature before dilution and gentle mixing. The 0.1 mg/mL glyphosate antibody solution in 1X phosphate buffered saline (PBS) buffer (pH = 7.4) was drop casted onto the substrate and reacted for 2 h in the dark. Finally, the unreacted NHS-ester sites were quenched with a 1.0 M ethanolamine-HCl solution (1X PBS, pH = 8.6) for 15 min. The substrate was thoroughly rinsed with HPLC water and dried with N_2. The pH of each solution was measured with a Horiba LAQUAtwin pH-11 meter, and the pH of the solutions were adjusted with NaOH or HCl.

FGTs were fabricated with photolithography and aerosol jet printing, as described in Sections 2.4 and 2.5, respectively. For cleaning the gold FG2 surface for antibody functionalization, the surface was exposed to UV/ozone for 10 min using a stainless steel stencil then incubated in ethanol for 20 min with a PDMS well. The surface was thoroughly rinsed with ethanol before adding the thiol solutions. The clean gold surfaces were initially functionalized with 1 mM of 11-MUA and PEG thiol (1:1 molar ratio, 1:1 ethanol/water, 5% HCl). HPLC water was introduced as a solvent in order to decrease the wettability of the thiol solution, as ethanol can easily leak out of the PDMS well through minor imperfections in the PDMS/substrate seal. The

surface was subsequently reacted for EDC/NHS activation, antibody conjugation, and ethanolamine quenching, as described for the control substrate. The surface was never dried in between steps. Solutions were dispensed and drawn out of the PDMS well with a micropipette.

XPS, RAIRS, epifluorescence microscopy, and cyclic voltammetry were used as described in Sections 2.7 to 2.10. SPR measurements were conducted by C.E.F. on a Biacore S200 instrument (Cytiva Life Sciences, Marlborough, MA) set at 25 ˚C. All running buffers were filtered (0.22 µm, cellulose acetate, Thomas Scientific, Swedesboro, NJ) and degassed before use. Solutions were prepared fresh prior to measurement. A series CM5 chip (Cytiva Life Sciences, Marlborough, MA) was used for each run. For activating the dextran matrix toward antibody conjugation, 400 mM EDC and 100 mM NHS in Milli-Q water were co-injected and flowed over the chip at 10 µL/min for 7 min. Subsequently, the 0.2 mg/mL glyphosate antibody in 10 mM sodium acetate (pH = 5) , unless otherwise specified, was injected at 10 µL/min for 10 min. Finally, 1 M ethanolamine (pH = 8.5) was injected at 10 µL/min for 7 min. A 1 mM glyphosate stock was prepared with the running buffer and serially diluted ten-fold down to a concentration of 1 nM. The multi-cycle assay began with buffer injection. The sample solutions were injected at 20 µL/min over both the reference and active cell for 120 s. The running buffer was subsequently injected for 300 s to measure dissociation. Sample solutions were injected from lowest to highest concentration glyphosate. The running buffer, antibody concentration, and antibody solution pH were altered between trials (Table D.1).

All sensing measurements were carried out with 1X PBS as the aqueous electrolyte and buffer. Glyphosate stock was made by dissolving 1 mM glyphosate in 1X PBS and vortexed until full dissolution (~30 s). A ten-fold serial dilution was done for lower concentrations. The functionalization PDMS well was replaced with the larger PDMS well for sensing. Initial

measurements were carried out with 1X PBS only. V_G was swept until subsequent inverter curves overlapped. Once the device was stable, the buffer was removed from the well and replaced with fresh 1X PBS to ensure that the act of replenishing did not disturb the sensing surface, and ultimately, the FGT response. The target solution was then introduced, and the FGT response was measured over 10 min for glyphosate. The final 1X PBS curve was subtracted from the target curve, producing a signal (ΔV_{OUT}). The maximum value was recorded as the signal (peak ΔV_{OUT}). To guarantee a signal arises from target capture, the EGT was measured before and after the FGT measurements. EGTs that had significant drift were considered outliers for the study. All files were processed with a custom-made Python script. Plotting was done in OriginLab.

To measure the inverter curves, a custom-made Python program was used. V_G and I_G were sourced and measured, respectively, with a Keithley 2612B source-measure unit (channel B). The drain voltage (V_{DD}) was sourced with a Keithley 2611 source-measure unit across the transistor and over a load resistor (1 MΩ). The output voltage (V_{OUT}) was measured at the drain electrode with a Keithley 2612B source-measure unit (channel A). The source electrode was grounded. Inverter curves were measured with a sweep rate of 100 mV/s, V_G step size of 10 mV, and V_{DD} = –0.5V. V_G was swept from the OFF state to the ON state and back.

For inverter curves measured at 45 mV/s (UV/ozone study), the V_G and I_G were sourced and measured, respectively, with a Keithley 2400. The drain voltage (V_{DD}) was sourced with a Keithley 2611 source-measure unit across the transistor and over a load resistor (1 MΩ). The output voltage (V_{OUT}) was measured at the drain electrode with a Keithley 2612B source-measure unit (channel A).

4.3 Surface Characterization

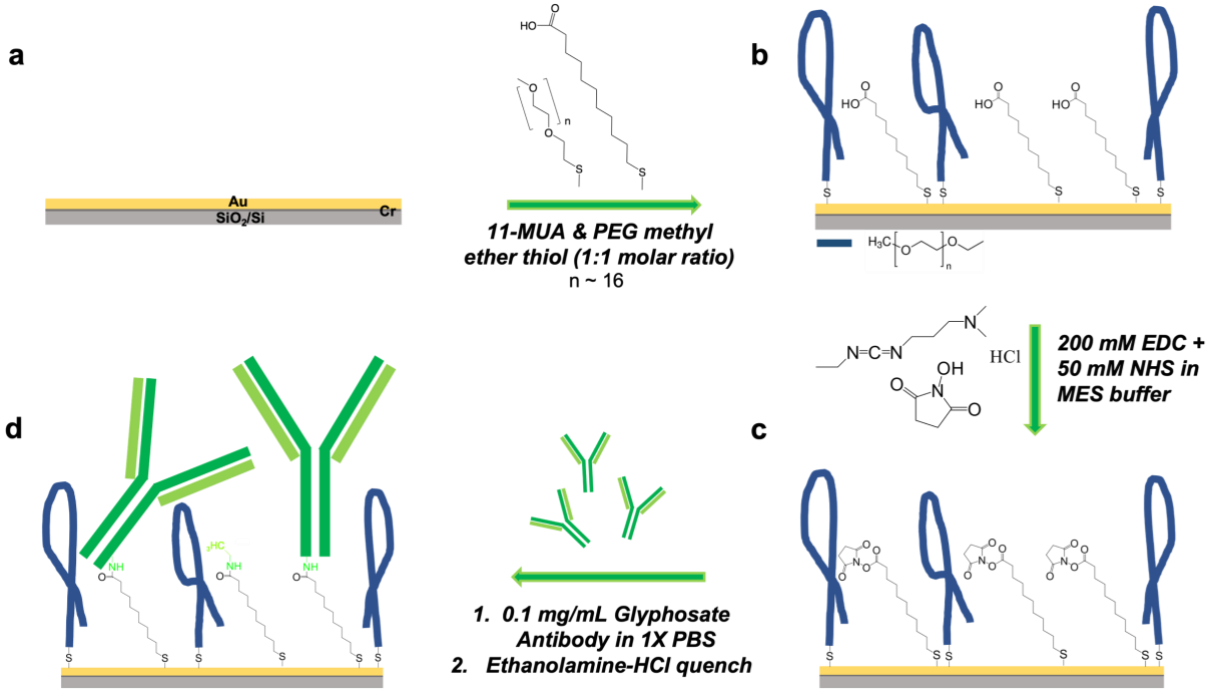

Figure 4.2. Antibody conjugation to gold through carboxyl-to-amine crosslinking. Four-step surface chemistry to conjugate antibodies to the gold sensing surface, FG2. (a) Bare, clean gold substrate. (b) Self-assembly of 11-MUA and PEG methyl ether thiol on gold through thiolate bonds. (c) EDC and NHS in MES buffer react with the carboxylic acid of 11-MUA to form an NHS ester tail group. (d) The NHS ester reacts with a primary amine on the antibody in 1X PBS, forming a stable amide bond that conjugates the antibody to the thiol.

Often used for transistor-based platforms, our strategy to conjugate antibodies to gold uses carboxyl-to-amine crosslinking in conjunction with self-assembled monolayers, or SAMs (Fig 4.2).[18,27,113] A versatile, well-studied route for surface functionalization of gold is the use of thiols to create a SAM. The sulfur head group of the thiol forms a covalent bond with gold, termed a thiolate bond. SAMs are sensitive to time, solvent, and surface cleanliness: all variables to consider when intending to have a dense, well-packed monolayer that can prevent nonspecific gold-analyte interactions. The thiol, 11-MUA, contains a carboxylic acid functional group at its tail that can be further reacted with EDC and NHS to yield a succinimidyl ester, termed NHS

ester.[113–117] The NHS ester functional group is readily substituted with primary amines, enabling conjugation to the antibody through lysine amino acid residues that are located on the outside of the antibody. Lysine residues can be located throughout the antibody, randomizing the orientation of the antibody with respect to the surface. Ethanolamine subsequently reacts with the NHS ester functional groups in order to prevent binding with other primary amines in the buffer or sample solutions.[113] PEG methyl ether thiol is included in the monolayer as an anti-fouling agent.[118] It has also been reported to reduce the effect of Debye screening due by reducing the relative permittivity compared to water,[86,119–121] where the effect depends on the length and extension of PEG.[87,121]

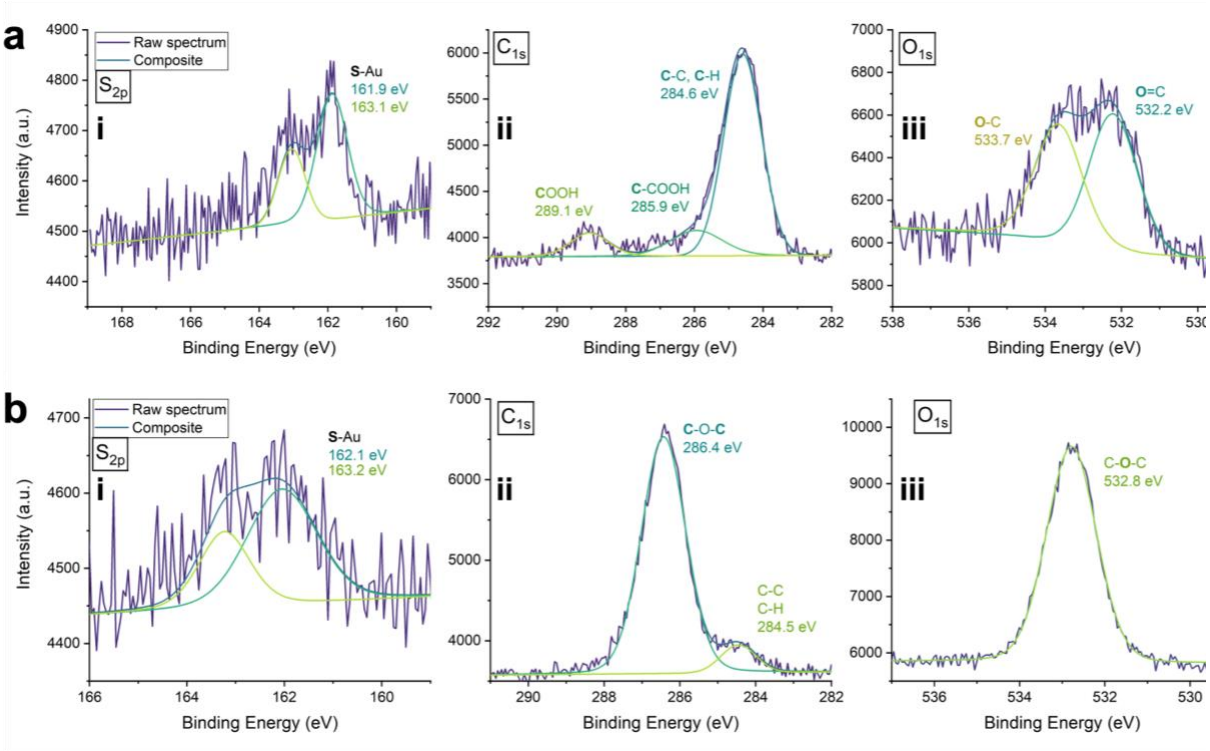

Figure 4.3. XPS of 11-MUA and PEG monolayer. SAMs of (a) 11-MUA and (b) PEG thiol on gold are characterized with high-resolution XPS spectra of (i) S_{2p}, (ii) C_{1s}, and (iii) O_{1s} orbitals. Characteristic peaks are labeled.

We first characterized monolayer formation with 11-MUA and PEG thiol using X-ray photoelectron spectroscopy (XPS). XPS is a quantitative, surface-sensitive characterization tool

that can be used to determine the chemical composition and identify the characteristic bonds of the SAM, importantly including the thiolate bond and functional groups along the thiol. XPS uses high energy x-rays to promote ejection of photoelectrons from the sample, travelling toward the hemispherical analyzer (detector) which a specific kinetic energy. The measured kinetic energy and work function of the detector are subtracted from the x-ray's energy (hν) to calculate the electron's binding energy, corresponding to an element's orbital and bond type.[122] The self-assembly of 11-MUA and PEG thiol were studied and characterized with XPS both independently and as a mixed monolayer. The high-resolution spectra for 11-MUA and PEG thiol were collected for 20 h self-assembly times in a 1 mM ethanolic solution. In Fig 4.3a, 11-MUA exhibited an S_{2p} doublet at 161.9 eV and 163.1 eV, indicating gold-thiol covalent binding.[123] Based on spin-orbit splitting, the S_{2p} doublets were fit with a 2:1 area ratio for the $2p_{3/2}$ and $2p_{1/2}$ states, respectively. Characteristic carbon bonds include aliphatic carbon (C–C, C–H) at 284.6 eV, the carbon adjacent to the carboxylic acid tail (C–COOH) at 285.9 eV, and the carbon within the carboxylic acid functional group (COOH) at 289.1 eV.[112,124–126] Additionally, the carbonyl oxygen and alcohol oxygen are characterized at 532.2 eV and 533.7 eV in the O_{1s} spectrum, respectively. PEG thiol similarly exhibited the thiolate bond observed in the doublet at 162.1 eV and 163.2 eV in Fig 4.3b**.** Since the PEG thiol is primarily composed of ether (C-O-C) functional groups, the large intensity C_{1s} peak at 286.4 eV is attributed to ether carbon.[127,128] A small aliphatic carbon peak was observed at 284.5 eV. This is interpreted as adventitious carbon, suggesting that there were bare gold sites on the substrate interacting with the air. Finally, the O_{1s} spectrum contains a single peak at 532.8 eV, representative of the oxygen within the ether.

The high-resolution spectra for a 1:1 molar ratio of 11-MUA to PEG thiol are shown in Fig 4.4 for different self-assembly times. High-resolution spectra of 11-MUA and PEG thiol

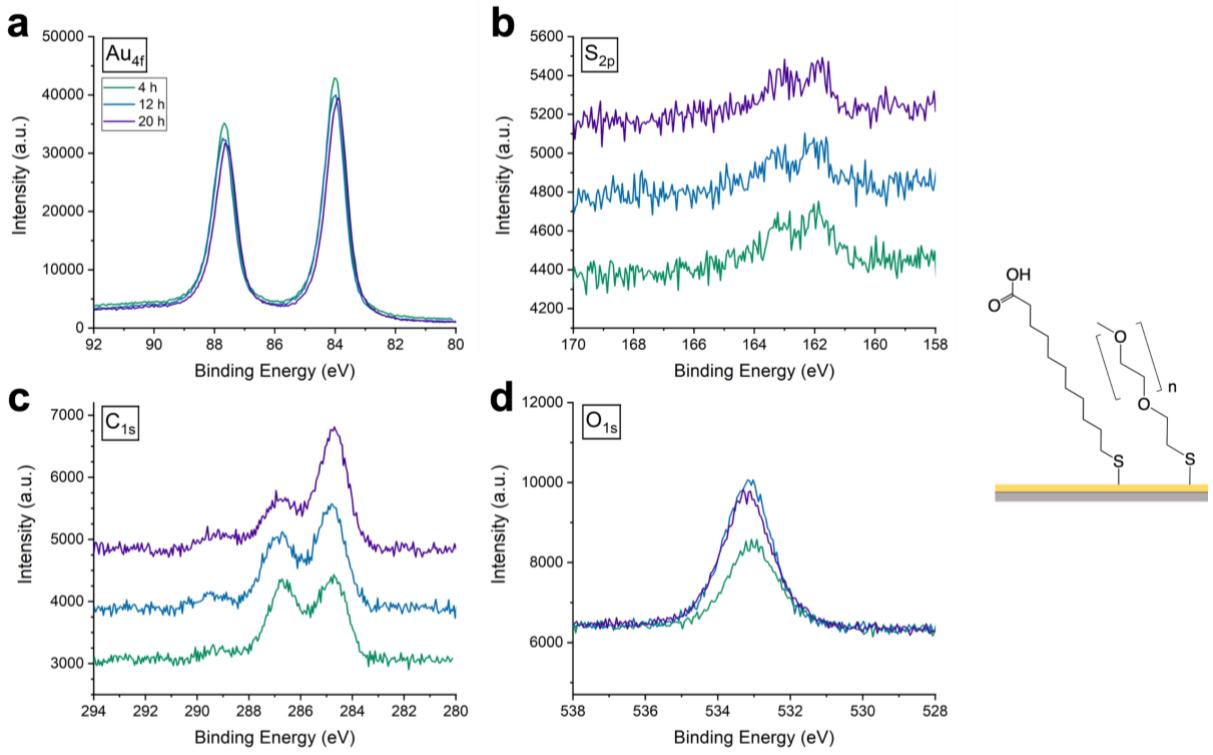

Figure 4.4. Time-dependent formation of 11-MUA and PEG thiol mixed monolayer. High-resolution XPS spectra of (a) Au_{4f}, (b) S_{2p}, (c) C_{1s}, and (d) O_{1s} orbitals of mixed monolayer of 11-MUA and PEG at a l:1 molar ratio on gold. Self-assembly times were 4 h (green), 8 h (blue), and 20 h (purple).

monolayers for different self-assembly times are included in Appendix B (Figs B.1 and B.2). After 4 h, there is an indication of self-assembly for all samples, as made evident by the thiolate doublet near 162 eV. There was little change in the characteristic peaks of 11-MUA over 20 h. However, PEG thiol showed time-dependent changes in its self-assembly on gold between 4 h and 12 h. Namely, the attenuation of both the Au_{4f} and S_{2p} doublets indicate that self-assembly times beyond 4 h lead to densification of the monolayer, where thiols assemble in bare gold sites. Also, characteristic ether peaks increased in intensity while the adventitious carbon peak near 284.5 eV decreases with self-assembly time, further evidencing an increase in the number of PEG thiols molecules. The 11-MUA/PEG sample spectra contains characteristics of both thiols, but these

characteristics change with self-assembly time. The decrease in the ether carbon peak (~286.4 eV) with time suggests competitive adsorption between 11-MUA and PEG thiol, where the increase in intensity of both the aliphatic carbon and carboxylic acid carbon peaks suggest 11-MUA displaces PEG thiol from the surface over time. However, at 12 h, the O_{1s} peak, near ether oxygen (~532.8 eV), and the Au_{4f} doublet have intensities that are maintained after 20 h. The ether oxygen peak also increases from 4 h to 12 h. With this, the alleviation of space from perhaps physisorbed PEG thiol promoted binding of both PEG and 11-MUA on the surface. In order to guarantee a dense monolayer based on both the PEG and 11-MUA/PEG XPS time studies, the functionalization times were kept at 20 h. For tailoring the number of 11-MUA carboxylic acid sites, the molar ratio of PEG thiol can be increased (Fig B.3). XPS revealed a larger intensity C_{1s} peak for ether carbon at 286.6 eV, increasing from 31.3% to 43.8% of the C_{1s} area from a 1:1 to 1:2 molar ratio, respectively.

Reflection-absorption infrared spectroscopy (RAIRS) uses p-polarized IR light to measure vibrations on a reflective surface to characterize absorbed molecules. Because it utilizes a low grazing angle (4°) from the surface normal, only vibrational modes whose dynamic dipole has a non-zero component perpendicular to the surface are resolvable.[129] Fig 4.5 includes the spectra from 11-MUA, EDC/NHS activation, and antibody-conjugated gold electrodes. Firstly, the 11-MUA spectrum (green) exhibits two characteristic bands for carbonyl stretching (ν(C=O)) within the carboxylic acid: 1738 cm^{-1} and 1717 cm^{-1}.[130] Depending on conditions, such as EDC and NHS concentration, solvent, and pH, EDC/NHS activation can also yield nonreactive anhydride and/or *N*-acylurea functional groups.[114–116] The challenge in distinguishing the NHS ester from nonreactive groups is primarily from band overlap with anhydride at 1750 cm^{-1} ((ν_{as}(C=O)) and 1820 cm^{-1} (ν_{s}(C=O)).[114] The *N*-acylaurea is characterized by bands at 1548 cm^{-1} and 1650 cm^{-1},

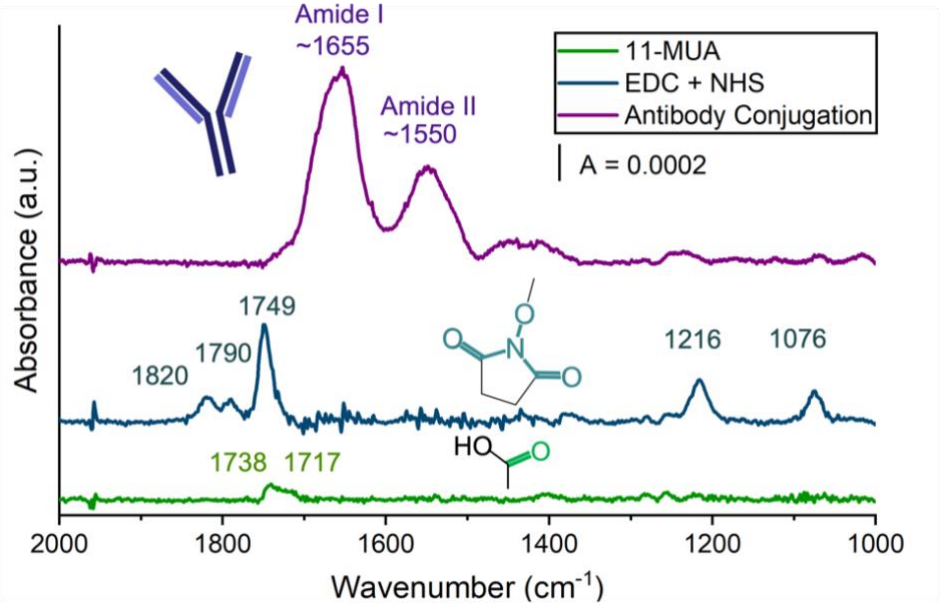

Figure 4.5. RAIRS spectra of EDC/NHS activation and antibody conjugation. RAIRS spectra and characteristic bands of 11-MUA (green), EDC/NHS activated (blue), and antibody-conjugated (purple) gold electrodes.

resulting from amide I and amide II vibrations, which were not found in the EDC/NHS spectrum (blue) in Fig 4.5. After activation, the NHS ester group is characterized by a triplet of carbonyl bands: 1749 cm^{-1} (ν_{as}(C=O)), 1790 cm^{-1} (ν_{s}(C=O)), and 1820 cm^{-1} (ν(C=O)).[114–116,130,131] The band at 1216 cm^{-1} is assigned to the C-N-C stretch (ν_{as}(C–N–C)) while the band at 1076 cm^{-1} is assigned to the N–C–O stretch (ν(C–O)) of the NHS ester.[114–116,130,131] These two bands are solely indicative of NHS ester, assuring its presence on the surface. After reacting with the glyphosate antibody, broad amide I (1600-1700 cm^{-1}) and amide II (1500-1600 cm^{-1}) bands emerged in the spectrum (purple), with no carbonyl bands from the NHS ester present. These large represent various bands from secondary structures within the protein; specifically, amide I bands typically contain C=O bending and N–H stretching and amide II bands contain N–H bending and C–N stretching.[132,133] Secondary structures include β-sheets, random coils, β-turns, and α-helices.

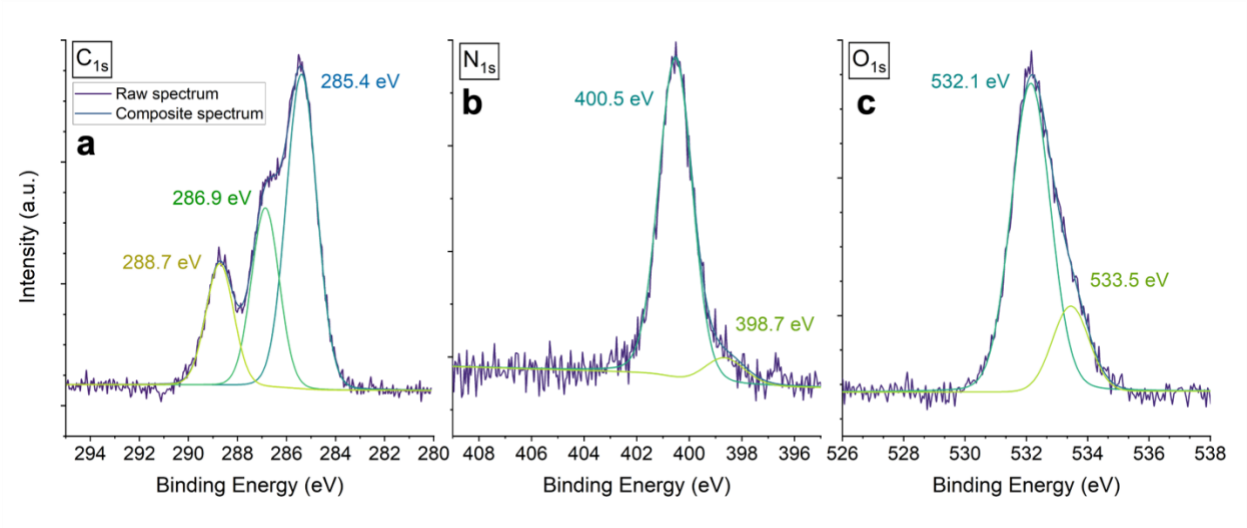

Figure 4.6. XPS of antibody conjugation to gold. High-resolution XPS spectra of control substrate functionalized with 11-MUA and subsequently reacted for antibody conjugation. Spectra include (b) C_{1s}, (c) N_{1s}, and (d) O_{1s} orbitals.

To further characterize antibody conjugation to gold, the same electrode used with RAIRS was characterized with XPS. Fig 4.6 shows the high-resolution spectra of the C_{1s}, N_{1s}, and O_{1s} orbitals, along with fits to characterize each peak. The C_{1s} spectrum contains three characteristics peaks: 285.4 eV for C–C, C–H, and C–COOH; 286.9 eV for C–S, C–N, and C–O; and 288.7 eV for HN–C=O.[113] The amide nitrogen and amine nitrogen appear in the N_{1s} spectrum as a large intensity 400.5 eV peak and a small intensity shoulder at 398.7 eV, respectively.[113] Carbonyl oxygen in the O_{1s} spectrum is located at 532.1 eV while the lower intensity peak at 533.5 eV characterizes O–C bonds.[113]

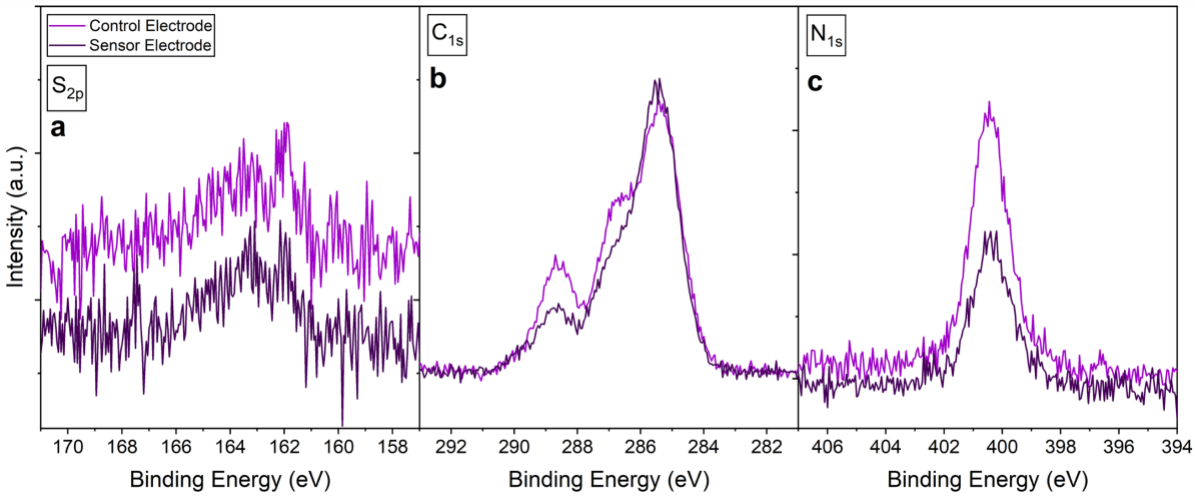

Figure 4.7. XPS characterization of antibody conjugation to FG2. High-resolution XPS spectra of (a) S_{2p}, (b) C_{1s}, and (c) N_{1s} orbital of antibody-conjugated gold electrodes. Glyphosate antibodies were conjugated to the sensing surface of the FGT (pink) and of the control electrode (purple). The sensing surface had a 1:1 molar ratio of 11-MUA to PEG thiol; whereas, the control electrode was solely 11-MUA.

An FG2 electrode that underwent the antibody conjugation chemistry, but in a PDMS well, was also characterized and compared to the control electrode (Fig 4.7). FG2 differed in that it had a mixed monolayer of 1:1 11-MUA to PEG thiol. Both electrodes have an S_{2p} doublet near 162 eV, indicative of thiolate bonds. The Au_{4f} spectrum (Fig B.4) shows attenuation of the doublet from monolayer formation to antibody conjugation for both electrodes, as is expected with a bulky protein preventing electrons from escaping the surface. Key differences between the sensor and control electrode are the intensity differences of the non-aliphatic C_{1s} and N_{1s} peaks, where the control electrode has higher intensity from both. As peak positions are similar, the lower intensities can be an indication that there was a lower density of antibody conjugated to the sensor electrode. XPS, thus, is able to characterize antibody conjugation directly to the sensor surface (2.8 x 1.0 mm), offering a surface characterization tool for future biosensing work.

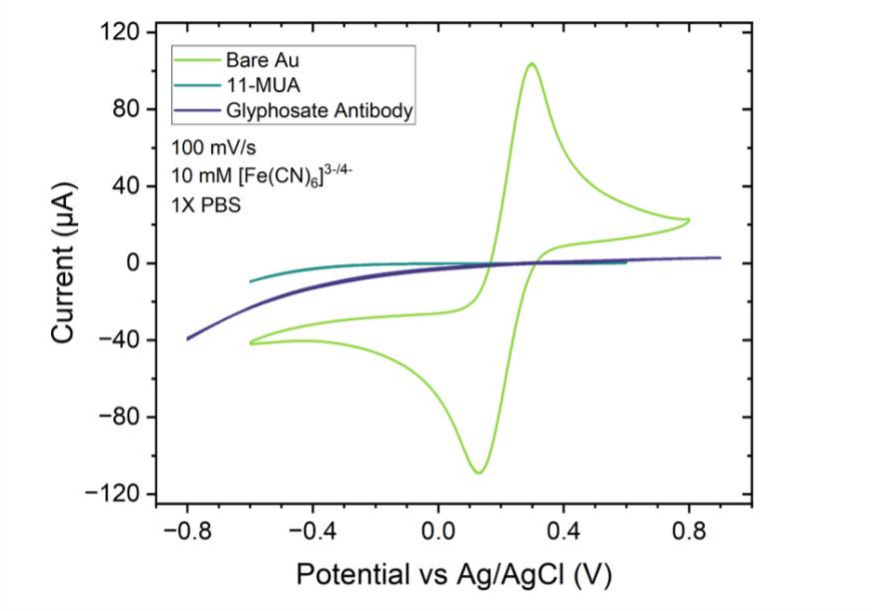

Figure 4.8. CV of 11-MUA and antibody conjugation. Cyclic voltammograms of bare gold (green), 11-MUA functionalized gold (teal), and antibody-conjugated gold (blue). The electrolyte was 1X PBS (pH = 7.4), the redox reporter was 10 mM $[Fe(CN)_6]^{3-/4-}$, and the sweep rate was 100 mV/s.

Antibody conjugation was further electrochemically characterized in Fig 4.8 with cyclic voltammetry (CV) using a redox reporter, $[Fe(CN)_6]^{3-/4-}$, in aqueous electrolyte (1X PBS). After 20 h incubation of gold substrates in 1 mM 11-MUA (ethanol/water, 10% HCl), both E_p characteristic of $[Fe(CN)_6]^{3-/4-}$ electrochemistry disappear. The self-assembled monolayer occupies electrode surface area, blocking access of $[Fe(CN)_6]^{3-/4-}$ species to the surface where they exchange electrons with the gold working electrode. In pH = 7.4 solution, the carboxylic acid groups of 11-MUA are partially negatively charged which can also cause repulsion of $[Fe(CN)_6]^{3-/4-}$. Subsequent EDC/NHS activation, antibody conjugation, and ethanolamine quenching also fully prevents electron transfer from +0.8 V to –0.9 V. Here, conjugation of antibodies increased the thickness of the bio-interfacial layer, leading to inaccessibility of $[Fe(CN)_6]^{3-/4-}$ near the gold electrode.

Because the EGT of the FGT is printed prior to surface functionalization, a surface cleaning protocol that does not degrade the EGT materials was determined. Initially, the FGT was patterned without FG2. After EGT fabrication, a stencil was used to thermally evaporate FG2 (5 nm Cr, 50 nm Au) aligned to the floating gate of the devices. Immediately after evaporation, all FG2 electrodes were enclosed with a PDMS well for surface functionalization. Despite a clean surface, the thermal evaporator produced misaligned Cr and Au layers, leading to poor adhesion and delamination of the electrode while immersed in aqueous buffers and thus, unstable FGTs. A simple tape test was done on electrodes after sensing where the outer area of the electrode was removed with the tape. To resolve the delamination problem, the entirety of the FGT was instead photolithographically patterned, and cleaning protocols were explored and assessed with XPS after 1 mM 11-MUA functionalization. The thiol solution was a 1:1 volumetric ratio of ethanol to HPLC water because of the low contact angle between ethanol and the substrate that enabled the leakage of ethanol from a minor defect in the PDMS well. Of solution-based and electrochemical cleaning methods noted for cleaning gold,[134] the study was focused on solution-based cleaning methods. Because FG2 is coupled to the EGT, electrochemical methods would also mean interrogation of the EGT outside of typical operating potentials, potentially damaging the device. We proceeded with UV/ozone (10 min) followed with ethanol immersion (20 min) due to the XPS S_{2p} spectrum revealing thiolate binding without physisorbed and/or oxidized thiol (Fig B.5).

4.4 Sensor Results and Discussion

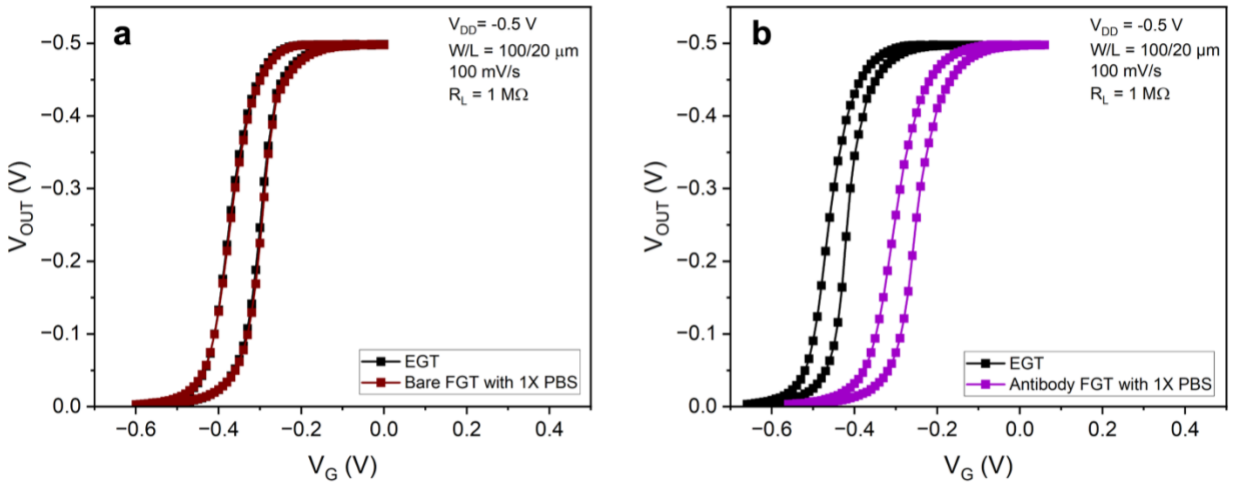

Figure 4.9. Inverter curve shift with antibody conjugation to FG2. (a) Bare FGT inverter curve and (b) antibody/PEG functionalized inverter curve against the device's EGT inverter curve. Antibody conjugation causes a positive shift in V_G of the inverter curve.

The glyphosate FGT was designed for maximal sensitivity to charge-based signals when functionalized with an antibody/PEG surface, as detailed in Appendix C. Briefly, for charge sensing, it is best that the ratio C_0/C_2 be small because this increases the steepness of the V_{OUT} vs V_G behavior (or gain) of the device, which in turn maximizes the signal when the sample and background inverter curves are subtracted. The areas of FG1 and CG were oversized in order to minimize voltage losses and maximize the gain. In this design, the sensitivity to capacitance-based signals is low due to the large C_2.[21] Fig 4.9 shows the inverter curves of a glyphosate FGT that was functionalized with antibodies, as described earlier, and its EGT subunit. Glyphosate FGTs turn on at a more positive V_G than bare gold FGTs compared to their EGT-subunits. This result is understood as a change in the work function of FG2. Functionalization of FG2 with 6-mercapto-1-hexanol (MCH) has been shown to shift FGT curves positively compared to FGTs without a SAM based on its dipole moment eliciting a positive change in the surface potential ($\Delta\varphi$) that

decreases the work function.[41] These findings are consistent with other reports SAM-induced work function shift, finding alkanethiols[135] and PEG thiols[136] both elicit positive shifts. The shift upon functionalization serves as an indicator for functionalization of FG2. FGTs that are not functionalized (bare gold FG2) perform the same as their EGT subunit, indicating maximized coupling between the sensing medium and EGT. This is expected for devices with a high C_2/C_0 ratio, as described earlier in Subsection 3.3.

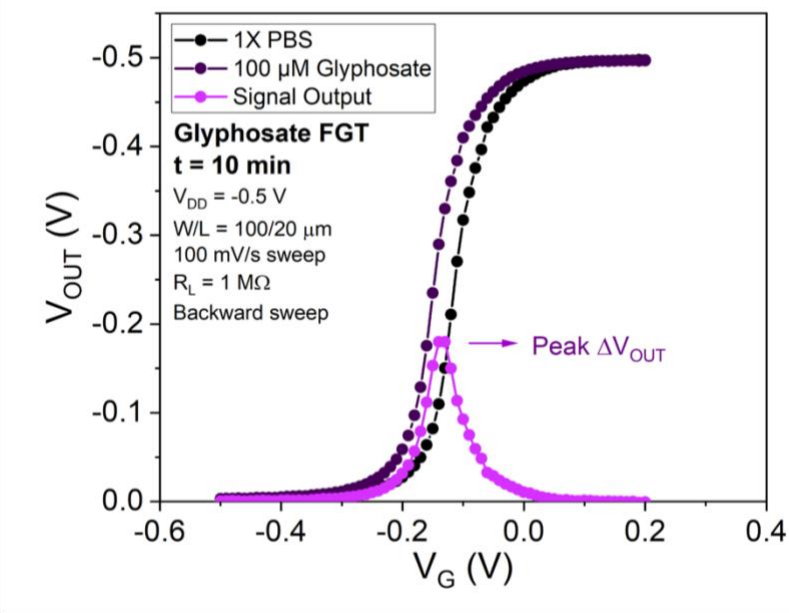

Figure 4.10. Glyphosate FGT biosensor inverter curve shift after glyphosate dosing. The glyphosate FGT biosensor inverter curves after stabilization in 1X PBS (black) and dosing in 100 µM serotonin (purple). The subtraction of the 1X PBS curve from the serotonin curve produces the signal readout, ΔV_{OUT} (pink). The maximum value of ΔV_{OUT} is the signal. Both inverter curves are of the backward sweep.

With the glyphosate binding to the antibody, we expected the surface-bound negative charges to contribute to a negative potential to FG2. The negative charges repulse the anions accumulating near FG2 when $V_G < 0$, necessitating a more negative V_G to turn the device ON. As such, the inverter curve shift would shift negatively in V_G with no change in the gain, as the device

is not designed toward sensitivity to changes in capacitance. This type of interfacial charge sensing has been observed with 11-MUA functionalized FGTs where, upon deprotonation of the carboxylic acid functional group with a basic solution, the transfer curves (V_T) and inverter curves shift negatively.[21,44,45] Our first experiments yielded a signal based on this sensing mechanism (Fig 4.10). The signal was measured by subtracting the backward sweeps of the stable 1X PBS (black) from the glyphosate curve (purple). The maximum value of the peak signal output (ΔV_{OUT}) was taken as the signal, shown in pink.

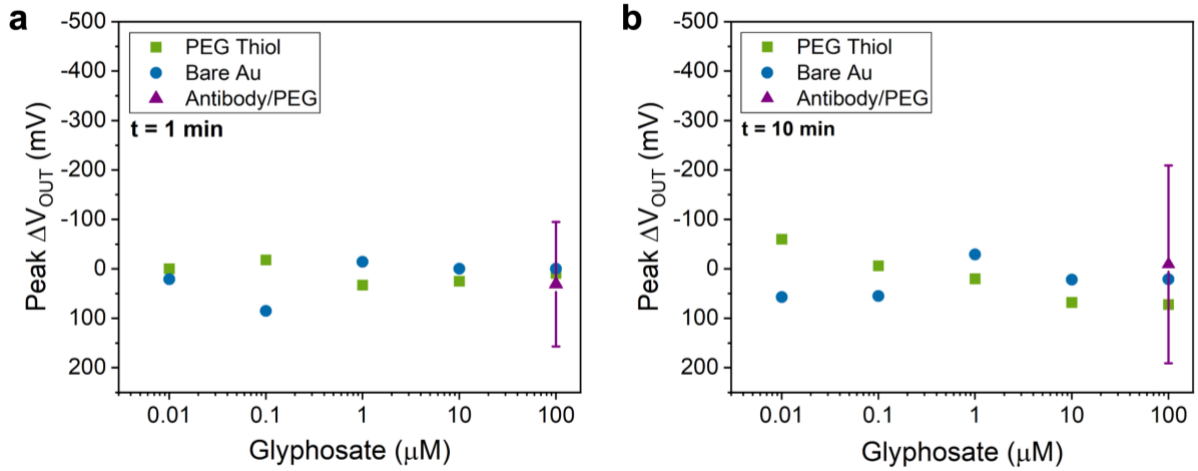

Figure 4.11. Response of glyphosate FGT biosensors and controls to glyphosate. Signals of glyphosate FGT biosensors after dosing with 100 µM glyphosate compared to PEG thiol and bare gold FGTs after dosing with glyphosate from 0.01 – 100 µM. Signals were measured (a) 1 min and (b) 10 min after glyphosate introduction. Bare gold and PEG-only FGT data points at each concentration represent a single device. Glyphosate FGT biosensors represent an average and standard deviation of 11 devices. All signals were measured with the backward sweep of the inverter curves.

PEG FGTs and bare gold FGTs were used as controls against glyphosate to measure if glyphosate-gold or glyphosate-PEG nonspecific interactions were occurring. The response to glyphosate was measured from 0.01 – 100 µM glyphosate (Fig 4.11). The concentration could not extend beyond 100 µM glyphosate due to the loss of buffering capacity from 1X PBS, as the pH

of 1 mM glyphosate and 10 mM glyphosate were 6.9 and 3.6, respectively. Preliminary results for the PEG (green) and bare gold (blue) FGT controls suggest there was no concentration-dependent response from glyphosate, but we observed drift of the FGT over time in both positive and negative directions.

The limit of detection (LOD), the lowest concentration that can be reliably detected, was calculated using

$$\mathrm{LOD} = \bar{x}_{\mathrm{control}} - 3\,\sigma_{\mathrm{control}} \tag{4.1}$$

where $\bar{x}_{\mathrm{control}}$ and $\sigma_{\mathrm{control}}$ are the mean and standard deviation of the bare gold and PEG FGT signals. Three standard deviations away from the mean was used for 99.7% confidence. Eq. 4.1 yields an LOD with units in mV (signal). A dose-response curve would be used to correspond the signal to a concentration along the curve. At 1 min and 10 min, the LOD was calculated as the corresponding concentration at –75 mV and –105 mV, respectively. At least 3 replicates at each concentration would be needed to better represent the LOD for the system.

Glyphosate FGTs were measured with the introduction 100 µM glyphosate at 1 min and 10 min for a total of 11 devices. The average signal (Fig 4.11, purple) was within the signals for the controls, and glyphosate FGTs shifted both negatively and positively in V_G with 100 µM glyphosate. The standard deviation also increased with dosing time. These results suggest that either capture of glyphosate by the antibody was not occurring within this time frame, the antibody has a poor binding affinity, or the signal was undetectable due to Debye length screening. The Debye length (λ_D) is the distance from the electrode interface where potential decays due to charge screening from the electrolyte.[137] In 1X PBS, λ_D is 0.7 nm. In all cases, there is concern over FGT stability over the exposure time, as the signals varied in both the positive and negative direction.

As the conjugation of the antibody to FG2 was characterized with XPS, surface plasmon resonance (SPR) was used to try to validate the binding affinity of the glyphosate antibody. SPR is a surface-sensitive technique that capitalizes on the ability of metal (e.g., gold) surfaces to generate plasmons upon a characteristic angle of incident polarized light. An evanescent wave field adsorbs the energy of the incident light, dropping the intensity of the total internally reflected light.[138] Changes in the refractive index between the gold and media above it change the characteristic resonance, producing a measurable, time-dependent signal termed response units (RU). As such, SPR is used to monitor biomolecular interactions where ligands are immobilized to the gold chip. Despite achieving high antibody loading (Fig B.6), a dose-dependent curve was not measured among 9 trials. To understand whether pH, electrostatics, or antibody density were inhibiting binding, these variables were altered among different trials (Table B.1) but did not enable a measurable binding response.

Because the binding affinity of the antibody could not be characterized with either the FGT or SPR, it is possible the binding affinity of the antibody was poor. However, this may also demonstrate the challenge to detect small molecules with such techniques where experimental conditions can hinder target binding and/or resolving a signal. From the perspective of the glyphosate FGT biosensor, an average IgG antibody in its upright orientation has binding sites ~15 nm away from the electrode interface, beyond the Debye length (0.7 nm).[139] IgY antibodies differ from IgG in that they have an extra domain at the Fc region and lack a hinge region. Binding of negatively charged gluten proteins to antibodies in an extraction cocktail with an FGT biosensor was deduced to elicit a signal based on changes in surface potential.[27] In looking into the methodology, we find two main differences between the aforementioned study and this work: the use of a reference FGT (PEG only) in parallel with the test FGT and integration of a microfluidic

PDMS chamber for sample delivery. Here, we anticipate the implementation of these methods moving forward will reduce the drift of the FGT, as the test FGT was calibrated to the reference FGT when establishing a baseline. Microfluidics would also alleviate mass transfer limitations, enabling target binding to occur over shorter time scales. Further, we can also look toward the use of antibody fragments as capture agents for less variability in capture site orientation, reducing the average distance of target capture from the surface.

Recent work on detecting interfacial charge with quasi-static FGTs by Thomas et al. finds a maximum V_T shift in similar electrolyte strength to 1X PBS (100 mM KCl) of approximately –150 mV, nearly half the signal compared to 10 mM KCl.[44] Comparing this to amplified signals with FGT models and the inverter configuration,[21] the signal upon 11-MUA protonation in 10 mM KCl was nearly –450 mV, suggesting a signal of approximately –225 mV in 100 mM KCl. Further, the V_T shift was halved for a mixed monolayer of 11-MUA to octanethiol (1:1 molar ratio), yielding a rough estimation of an approximate –100 mV signal anticipated for an FGT inverter. This resembles the mixed monolayer used for the glyphosate FGT biosensor, but the density of antibody binding sites on the surface, where a net charge of 2– would be introduced upon glyphosate capture at each site, is not quantified and binding sites are likely beyond the theoretical length of 11-MUA when considering a tilt angle of 30° (~1.5 nm), increasing charge-screening. In order to achieve small molecule detection while still utilizing models built for quasi-static FGTs (not considering a reference FGT), we can look toward the use of smaller capture agents that, in themselves, elicit changes in the interfacial charge upon target-binding, such as structure-shifting aptamers.

4.5 Conclusions

Prior FGT sensing contributions utilized self-assembly of thiols on gold to conjugate capture agents, such as aptamers and antibodies, and to explore the capacitive and ionic effects of thiols themselves. However, little characterization of these chemistries was done to validate the anticipated functionalization. In this work, antibody conjugation chemistry was achieved on the sensing electrode of the FGT, FG2, and was well-characterized using XPS, RAIRS, epifluorescence microscopy, and CV. A mixed monolayer of 11-MUA and PEG thiol was characterized with XPS, and epifluorescence microscopy revealed antibody conjugation up to a 1:9 molar ratio between 11-MUA and PEG. Responses to glyphosate at all relevant concentrations were measured for PEG thiol and bare gold FGTs. The responses were not concentration-dependent, and the signal that determines the LOD increases with increased exposure time to glyphosate. The glyphosate FGT biosensor does not respond to 100 µM glyphosate within 10 min of exposure beyond the responses of the control FGTs; moreover, when considering the irreproducibility, based on a large standard deviation, and the inability to increase glyphosate concentration without changes to pH, the glyphosate FGT biosensor cannot detect glyphosate. Furthermore, the antibody-glyphosate binding kinetics could not be verified with SPR. This is either the result of a poor binding affinity or demonstrates the challenge, even among advanced analytical instrumentation, to detect small molecules. In having used FGT models for charge-based sensing to optimize the biosensor, we must look toward other routes to consider detection of a small, charged molecules. As the electrolyte strength is considered to be a limitation for charge-based sensing with quasi-static FGTs, a simplest route is looking toward other types of capture agents with shorter lengths, such as aptamers, whose binding affinity is well-characterized.

Chapter 5: Designing an Aptamer-based FGT Toward Small Molecule Detection

5.1 Introduction & Motivation

In Chapter 4, the detection of the small, charged molecule, glyphosate, was inhibited either by the poor binding affinity of the antibody or the Debye length limitations of the platform with 1X PBS. To further amplify charge-based detection of small molecules beyond the design of the FGT, we look toward the capture agent. Nanobodies are a class of antibodies found in camels that lack the light chain domains, maintaining high binding affinities while truncating their height (~4 nm).[140] Implementing nanobodies enables capture closer to the sensing surface which is useful in cases where the charge screening, or the Debye length, prevents sufficient signal. Alternatively, single stranded oligonucleotides, or aptamers, have emerged as a pseudo-natural and synthetic capture agent whose height can be a few nm.[53] Aptamers that undergo structural changes upon target-binding can be utilized to rearrange the negative backbone of the DNA near the surface, further amplifying target capture for neutral molecules and small, charged molecules.

In this chapter, we reapproach small molecule detection with an FGT biosensor by implementing a structure-shifting serotonin aptamer reported by Nakatsuka et al. as the capture agent for detection outside of the Debye length.[72] Upon target-binding, the aptamer lengthens from 4.2 nm to 7.11 nm long, reorganizing the highly negatively charged aptamer away from the surface.[141] The detection of serotonin (172.6 Da) has been accomplished electrochemically in prior work by exploiting its electroactive nature at a conductive electrode,[142–144] by target capture with aptameric sensors,[72,145–151] and by its chemical reactivity as bivalent 4,4'-dimer-serotonin.[152] Here,

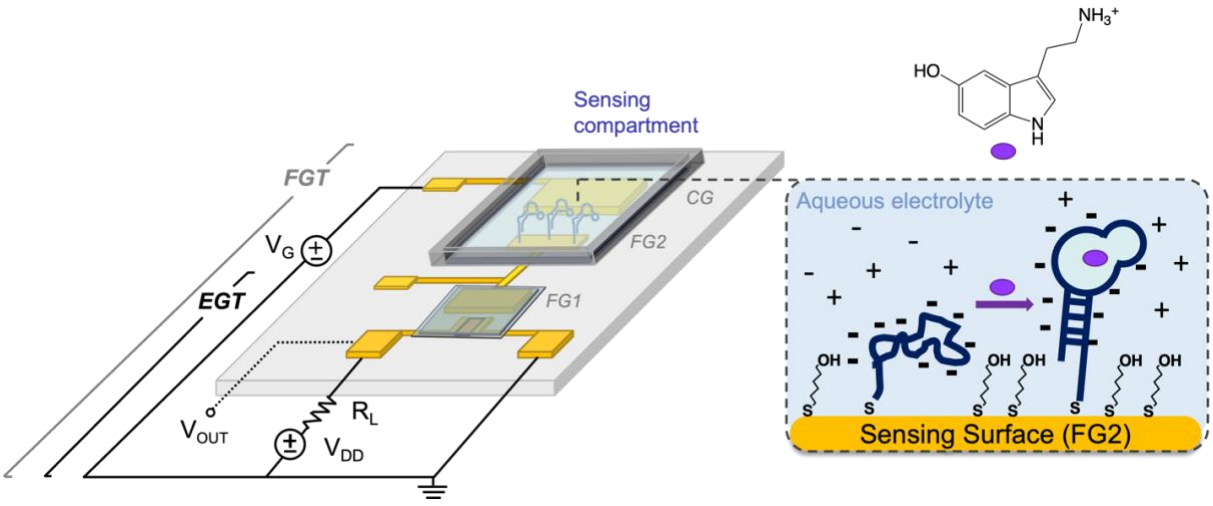

Figure 5.1. Diagram of the serotonin FGT biosensor. (a) Scheme of the device, outlining the inverter configuration and sensing compartment. The FGT (gray bracket) includes the control gate, upper end of the floating gate, and EGT inverter (black bracket). The schematic magnification of FG2 depicts the sensing surface composed of surface-bound aptamers and MCH upon serotonin introduction, showing the anticipated aptamer reorganization.

the structure-shifting mechanism of the charged aptamer (upon target capture) near the sensing surface[72] was anticipated to alter the gating of the FGT, placing the sensing mechanism and signal amplification onto the capture agent rather than just the target analyte (Fig. 5.1). Aptamer modification of the gold sensor surface was characterized via XPS and CV. The binding affinity of the serotonin aptamer was characterized with SPR, yielding a K_D of 360 nM.[153]

Our initial work revealed that the serotonin FGT biosensor produces a limit of detection (LOD) of ~2 µM serotonin in 5 min. However, investigation into the selectivity revealed some small molecule interferents, such as dopamine, also produced measurable signals. SPR similarly measures responses to ADP, dopamine, and histamine at relevant concentrations. While bare gold FGTs produced small responses across all relevant concentrations, MCH-only FGTs elicited dose-dependent responses of high magnitude. Furthermore, FGT inverter drift when interrogated in 1X PBS also raises the question of stability. The results here lay the groundwork for small

molecule detection with an aptameric FGT biosensor but prompts investigation into how serotonin interacts with the functionalized surface and why the aptameric FGTs necessitate a stabilization period.

5.2 Experiments

FGTs were fabricated with photolithography and aerosol jet printing, as described in Sections 2.4 and 2.5, respectively. Serotonin FGT biosensors were designed for charge-based sensing utilizing FGT models.[21] The architecture is further detailed in Appendix C. The surface functionalization for aptamer conjugation begins with reduction of 50 µM aptamer with 50 mM TCEP-HCl in TE buffer (pH = 8.0) for 2 h in the dark. The aptamer solution was diluted to 1 µM with TE containing 1 M NaCl and gently mixed with a micropipette. The concentration of aptamer was verified with a NanoDrop^{TM} One/One^{C} Microvolume UV-Vis Spectrophotometer (Thermo Fisher Scientific, Waltham, MA). The gold FG2 electrode was cleaned by dropcasting a 0.1 M NaOH + 27% H_2O_2 solution and leaving it for 15-20 min. The surface was thoroughly rinsed with HPLC water and dried with N_2. A PDMS well held the aptamer solution overnight (16-18 h). The surface was rinsed with TE followed with the addition of 1 mM MCH (TE buffer) for 30 min. The surface was then rinsed with TE and 1X PBS. The functionalization protocol for CV characterization was the same. XPS and CV were used for characterization, as detailed in the Sections 2.7 and 2.10, respectively.

SPR experiments were conducted by C.E.F. and J.H. on a Biacore S200 instrument (Cytiva Life Sciences, Marlborough, MA) set at 25 ˚C. All running buffers were filtered (0.22 µm, cellulose acetate, Thomas Scientific, Swedesboro, NJ) and degassed before use. Aptamer immobilization via biotin-streptavidin capture and the high-ionic-strength multicycle assay

protocols used were previously reported by Froehlich et al.[153] Selectivity studies were performed immediately after a high ionic strength multi-cycle SPR assay using the same chip and immobilized serotonin aptamer. Each sample ($CaCl_2$, ADP, GABA, tryptophan, histamine, or dopamine) was injected three times at 100 nM and then three times at 1 µM in the listed order. PBS-P+ containing 1 M NaCl was used as the running buffer and was used as the buffer to make all sample solutions. Statistical analysis performed for the selectivity testing used a one-way ANOVA with $\alpha = 0.05$ and the Tukey HSD test for means comparison between serotonin and interfering molecules: $CaCl_2$, GABA, and tryptophan, as well as separately for dopamine and histamine.

For FGT sensing, the functionalization PDMS well was replaced with the larger PDMS well. Initial measurements were carried out with 1X PBS only. Serotonin was added to 1X PBS at a 10 mM serotonin concentration and vortexed until full dissolution. The 10 mM stock was serially diluted with 1X PBS to concentrations ranging from 1 nM to 1 mM. The negative controls were prepared in the same manner (dopamine, $CaCl_2$, GABA, and L-tryptophan). The gate voltage was swept until subsequent inverter curves overlapped. The stabilization period, where the inverter curves continuously drifted until overlapping, typically lasted 5 to 20 min. Once the device was stable, the buffer was removed from the well and replaced with fresh 1X PBS to ensure that the act of replenishing did not disturb the sensing surface, and ultimately, the FGT response. The serotonin solution was then introduced, and the FGT response was measured over 5 min. The final 1X PBS curve was subtracted from the serotonin curve, producing a signal peak (ΔV_{OUT}). The maximum value was recorded as the signal (peak ΔV_{OUT}), and all the calculated signals over the 5 min measurement period were averaged as the final reported signal. J.H. conducted a portion of the sensing measurements.

To measure the inverter curves, a custom-made Python program was used. V_G and I_G were sourced and measured, respectively, with a Keithley 2612B source-measure unit (channel B). The drain voltage (V_{DD}) was sourced with a Keithley 2611 source-measure unit across the transistor and over a load resistor (1 MΩ). The output voltage (V_{OUT}) was measured at the drain electrode with a Keithley 2612B source-measure unit (channel A). The source electrode was grounded. Inverter curves were measured with a sweep rate of 100 mV/s, V_G step size of 10 mV, and V_{DD} = –0.5V, V_G was swept from the OFF state to the ON state and back.

5.3 Surface Characterization

To characterize the surface functionalization directly at the sensing surface, FG2, we employed XPS to determine surface chemical composition. The same methodology for functionalizing the sensing surface was used. After overnight aptamer self-assembly and 30 min of MCH backfilling, the surface was rinsed thoroughly with 1X TE. The surface was incubated with 1X PBS for 5 min then rinsed thoroughly with Milli-Q water. The 1X PBS incubation was done to mimic the sensing environment. A Milli-Q water rinse was necessary to remove any salt ions from the surface, which could contribute to the XPS signal and interfere with the analysis.

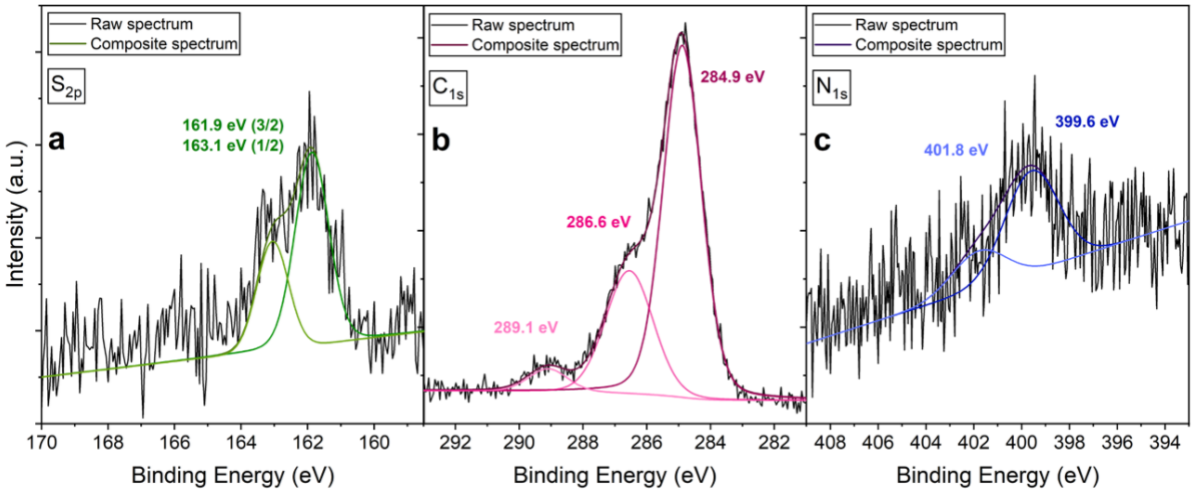

Figure 5.2. XPS of aptamer/MCH-functionalized FG2 electrodes. The electrode was immersed in 1X PBS for 5 min after functionalization before rinsing with water. High-resolution spectra of (a) S_{2p}, (b) C_{1s}, and (c) N_{1s} orbitals with labels for each peak position.

High-resolution spectra revealed peaks at binding energies characteristic of the elemental composition of thiolated DNA and MCH. Fig 5.2a shows the S_{2p} high-resolution spectrum contains a doublet representative of S–Au bonds (161.9 eV), indicating bound thiol.[123] To identify the presence of aptamer on the surface, C_{1s} and N_{1s} spectra were analyzed. Carbon species relevant to

MCH include aliphatic carbon, the alcohol functional group, and C–S. In Fig 5.2b, the three carbon peak fits were assigned to the following moieties: C–C and C–H (284.9 eV); C–N, C–O, and C–S (286.6 eV); and N–C(=O)–N, N–C(=O)–C, N–C(=N)–N, N=C–N, and N–C–O (289.1 eV).[123] The higher energy peak at 289.1 eV relates directly to C species solely in the aptamer. Aliphatic carbon composes the aptamer's C_6 spacer, MCH, and adventitious carbon adsorbed to the gold surface. The N_{1s} high-resolution spectrum in Fig 5.2c has two peaks: 399.6 eV and 401.8 eV. These peaks evidence the presence of aptamer on the FG2 surface, where the 399.6 eV peak is from heteroaromatic nitrogen while the 401.8 eV peak is from N–C(=O)–N, N–C(=O)–C, N–C(=N)–N, N=C–N, and N–C–O.[154]

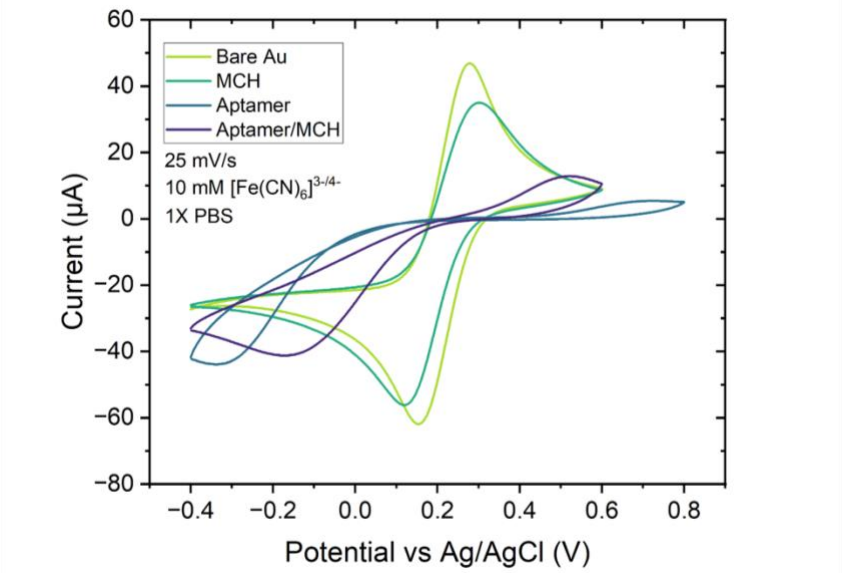

Figure 5.3. Cyclic voltammograms of aptamer/MCH functionalization. CV of bare gold (green), MCH-functionalized gold (teal), aptamer/MCH-functionalized gold (blue), and aptamer-functionalized gold (purple). The sweep rate was 25 mV/s, the redox reporter was 10 mM $[Fe(CN)_6]^{3-/4-}$, and the electrolyte was 1X PBS.

Fig 5.3 presents cyclic voltammetry (CV) of $[Fe(CN)_6]^{3-/4-}$ in 1X PBS employed for qualitative characterization of film density as a function of surface functionalization steps. After overnight incubation of gold substrates in 1 µM thiolated aptamer, the peak-to-peak separation

(ΔE_p) in CV for $[Fe(CN)_6]^{3-/4-}$ electrochemistry increased substantially from 122 mV to 920 mV. The adsorbed aptamer occupies electrode surface area, blocking access of $[Fe(CN)_6]^{3-/4-}$ species to the surface where they exchange electrons with the gold working electrode. The aptamer backbone is highly negatively charged which can also cause repulsion of $[Fe(CN)_6]^{3-/4-}$. Subsequent exposure of the aptamer-functionalized gold to 1 mM MCH decreases ΔE_p to 761 mV, suggesting that MCH displaces physisorbed aptamer on the surface, decreasing repulsion of $[Fe(CN)_6]^{3-/4-}$. Finally, MCH-only functionalized surface (1 h self-assembly) exhibited ΔE_p of 182 mV which is higher than gold but lower than aptamer/MCH surfaces.

5.4 Sensor Results and Discussion

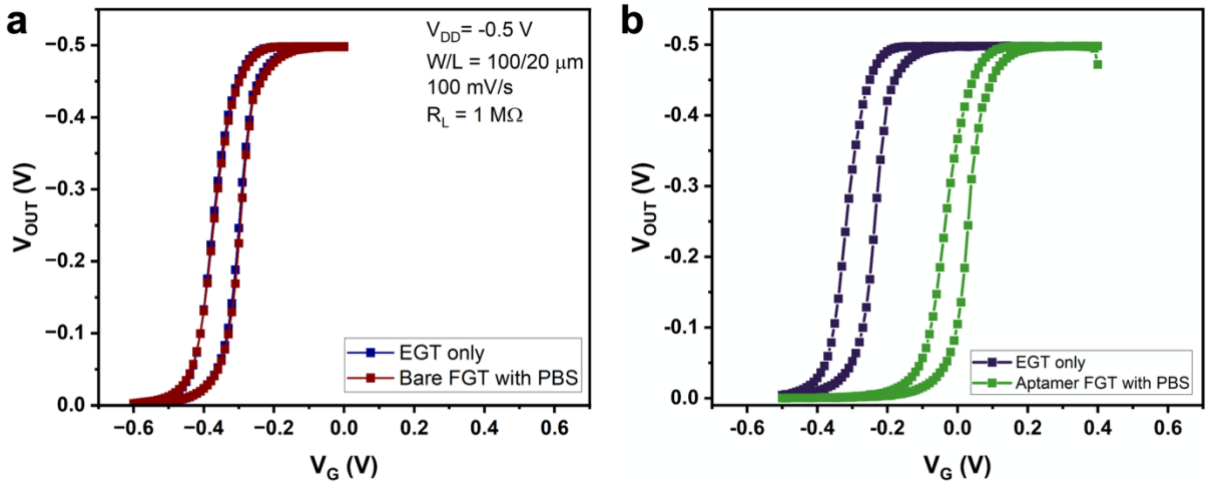

Figure 5.4. Inverter curve shift with aptamer/MCH functionalization of FG2. (a) The bare FGT operating with 1X PBS overlaps with the EGT, showing minimal potential loss over the sensing medium. (b) The aptamer/MCH-modified FGT operating with 1X PBS (green) shows a significant positive shift compared to the EGT alone (blue).

To elucidate the sensing mechanism, it is important to first understand how functionalization alters the gating of the FGT. In 1X PBS (pH = 7.4), the serotonin aptamer's phosphodiester backbone is negatively charged. Previous studies find this aptamer arranges into a

folded conformation in close proximity to the substrate.[72,141,146] After functionalization of FG2 with the aptamer and MCH, the FGT turns on at more positive potential compared to the EGT subunit of the same device (Fig 5.4b). Functionalization of FG2 with MCH has been shown to shift FGT curves positively compared to FGTs without a SAM due to a lowered work function and positive change in the surface potential ($\Delta\varphi$).[41] Figure 5.4a shows that bare FGTs (no functionalization on FG2) have little to no threshold voltage shift compared to the EGT subunit. Most serotonin FGT biosensors exhibited a stabilization period during 1X PBS that varied in time from one device to the next. Devices whose FGT and EGT-subunit had inverter curves that overlapped were considered outliers.

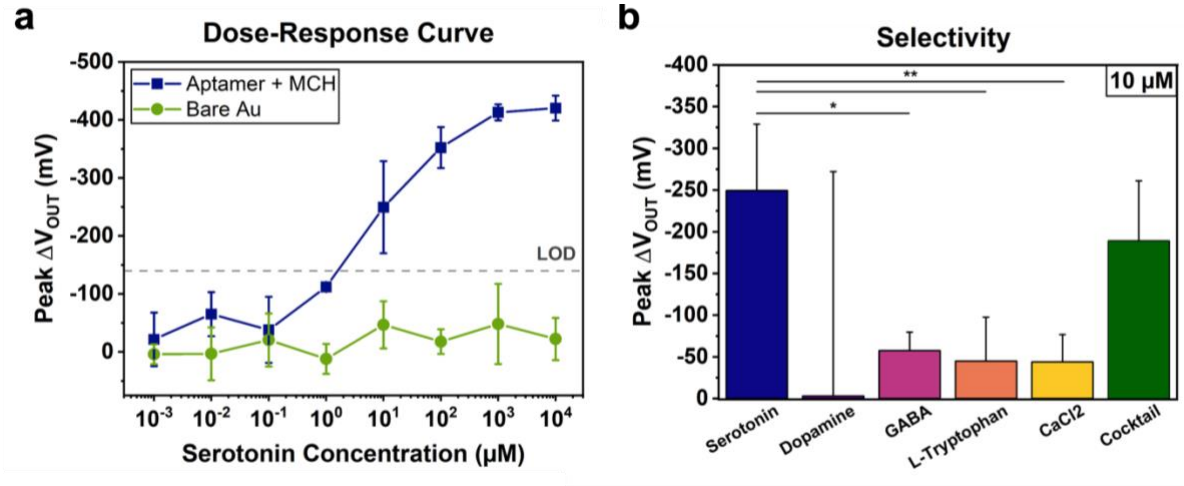

Figure 5.5. Concentration dependence and selectivity of serotonin FGT biosensor. (a) Dose-response curve for different concentrations of serotonin with aptamer-modified (blue) and non-modified (green) FGT biosensors. The dashed line represents the LOD. (b) Selectivity of the serotonin FGT biosensor against dopamine, $CaCl_2$, GABA, L-tryptophan, and a cocktail of all control analytes at a concentration of 10 μM. Error in both plots is shown as the standard deviation from 3-4 FGT biosensors. * indicates $p < 0.01$ and ** indicates $p < 0.005$ as determined using a one-way ANOVA with $\alpha = 0.05$ and using the Tukey HSD test for means comparison against serotonin, excluding the dopamine and control cocktail results.

Upon aptamer-mediated serotonin capture, the aptamer's folded conformation reconfigures, elongating away from the surface.[72,146] This conformational change redistributes

negative charges along the aptamer backbone away from the sensing interface. Due to the high density of negative charges on the aptamer compared to the single positive charge on serotonin, we initially attributed the charge-based FGT response largely to aptamer reconfiguration. The reconfiguration of negative charge at the interface reduces the aptamer-induced surface potential at FG2, necessitating a more negative V_G to induce enough charge to ultimately turn the device ON, as shown in Fig D.1.[44,45] In Fig 5.5a, the serotonin FGT biosensor produces dose-dependent signals after 5 min of exposure to serotonin compared to the bare gold FGT. The LOD, calculated with the average and standard deviation of the bare controls using Eq. 4.1, was approximately 2 µM.

Table 5.1. Serotonin aptamer selectivity with SPR. Average SPR binding response for each target analyte at 100 nM and 1 µM. Error is the standard deviation from three replicates. All error is shown as the standard deviation from three replicates.

Analyte	Response at 100 nM (RU)	Response at 1 µM (RU)
ADP	-24.5 ± 30.6	-10.3 ± 10.7
$CaCl_2$	-0.1 ± 0.1	-0.0 ± 0.1
Dopamine	0.7 ± 0.9	-7.2 ± 2.2
GABA	-2.4 ± 1.5	0.0 ± 0.2
Histamine	0.1 ± 0.0	5.5 ± 5.5
L-tryptophan	-0.4 ± 0.2	-0.1 ± 0.1
Serotonin	3.0 ± 0.1	10.6 ± 0.1

The serotonin FGT biosensor exhibited good selectivity against GABA, L-tryptophan, and $CaCl_2$; however, the device responds inexplicably to dopamine with a high level of variability (Fig 5.5b). When the serotonin FGT biosensor was tested against a 10 µM cocktail of these control analytes (2.5 µM of each), the device consistently exhibits nonnegligible negative responses. SPR results for probing the selectivity of the aptamer found statistically insignificant responses to 1 µM

$CaCl_2$ and L-tryptophan, as determined using a one-way ANOVA with $\alpha = 0.05$ and using the Tukey HSD test for means comparison. When tested against ADP the surface elicited large, negative responses for both 100 nM and 1 µM concentrations. Table D.1 provides the SPR responses for all analytes at both concentrations. Dopamine and histamine also elicited relatively large responses at 1 µM. As opposed to the positive responses arising from serotonin capture at the surface,[153] negative SPR responses can result from aptamer conformational changes where there is a decrease in the effective refractive index near the sensor surface, such as if the aptamer undergoes a conformational change that increases the hydrodynamic radius and/or decreases its hydration shell.[155] This aligns with the observed responses to the cocktail control, indicating that dopamine may be responsible for the aptamer elongation and subsequent changes in the gating of the FGT.

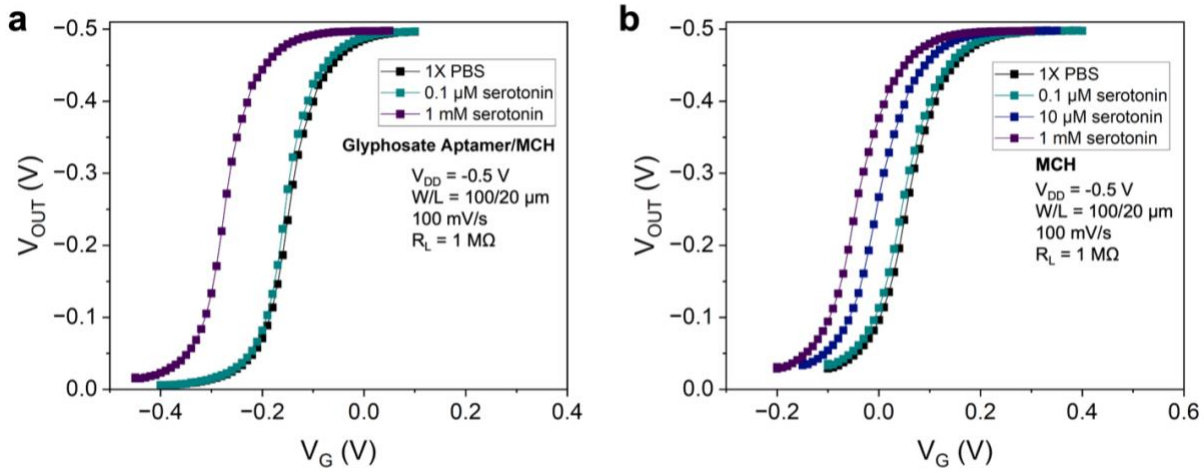

Figure 5.6. Functionalized control FGTs respond to serotonin. (a) Glyphosate aptamer/MCH FGTs and (b) MCH FGTs inverter curves (backward sweeps) remain near the 1X PBS curve (black) after 0.1 µM serotonin dosing (teal) but shift negatively after 10 µM serotonin (blue) and 1 mM serotonin (purple).

Interestingly, responses are also observed when the serotonin aptamer was replaced with the glyphosate aptamer (Fig 5.6a), eliciting an average response to 1 mM serotonin of

–282 ± 120 mV among 3 devices. Similar to the serotonin aptamer, FGTs with larger functionalization shifts (between FGT and EGT-subunit) were observed to produce larger responses to serotonin (Fig D.2). To deduce whether nonspecific aptamer-serotonin or MCH-serotonin interactions were occurring, MCH-only FGTs were tested where MCH was functionalized for 1 h with TE. Similarly, MCH FGTs exhibited both a stabilization period and dose-dependent responses to serotonin (Fig 5.5b). Furthermore, with PEG thiol and hexanethiol FGTs, 10 μM serotonin also elicited a similar response over 5 min, indicating nonspecific interactions between serotonin and the functionalized sensing surfaces, shown in Fig D.3. We also reconsider the selectivity results, as some of these target analytes may be interacting with the surface, be it the gold electrode or thiols, in a similar manner as serotonin.

To understand the nonspecific interactions at the FG2 interface, we can look toward surface characterization. Two possible scenarios may be responsible for the negative shifts observed from serotonin with functionalized FGTs: fouling by polyserotonin or electrochemical desorption of thiols. The production of polyserotonin films at the surface of gold electrodes has been reported for both spontaneous polymerization and electropolymerization of serotonin.[156] XPS can be strategically used to understand how the sensing surface was altered after stabilization in 1X PBS and dosing in serotonin. XPS was used to measure the high-resolution spectra of the N_{1s} orbital in search of polyserotonin and the S_{2p} orbital to monitor changes in the monolayer, specifically, for loss of thiols from the surface. Because the aptamer contains nitrogen, the study was focused on MCH-functionalized surfaces in order to associate the N_{1s} signal with polyserotonin. As further evidence of polyserotonin film growth, the high-resolution spectrum of the Au_{4f} orbital was measured, expecting a lower intensity with a polyserotonin coating. Finally, the C_{1s} spectrum was

measured to characterize MCH functional groups in the control and to further characterize the changes in the sensing surface.

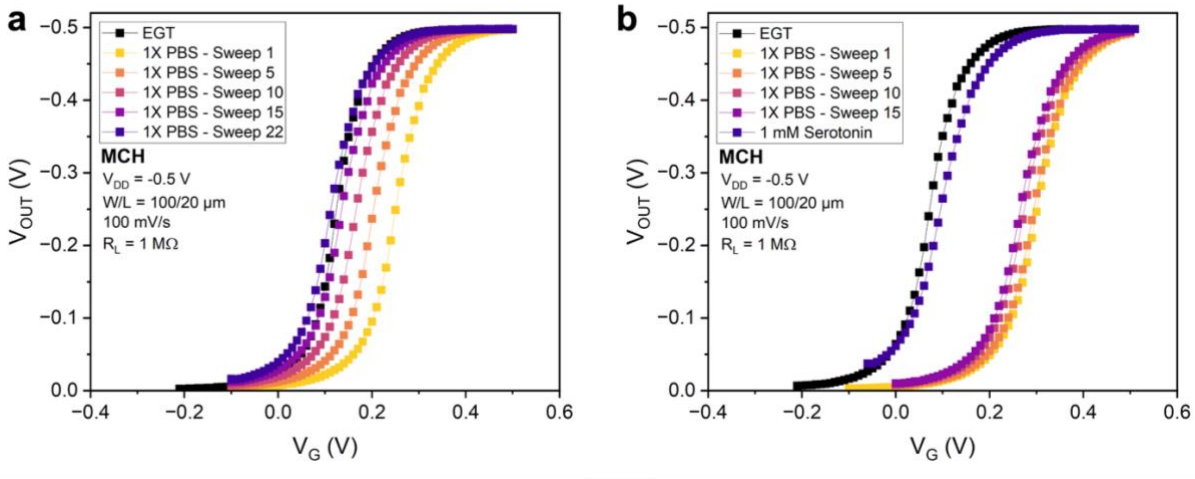

Figure 5.7. MCH FGTs stabilized in 1X PBS and subsequent exposure to 1 mM serotonin. (a) Stabilization of an MCH FGT, leading to FGT and EGT-subunit inverter curve overlap. (b) Stabilization of a second MCH FGT, where subsequent 1 mM serotonin exposure leads to near FGT and EGT-subunit inverter curve overlap. Despite having the same functionalization protocol, one FGT is unstable while the other is fairly stable for ≥ 15 sweeps. Inverter curves are of the backward sweep.

The inverter curves measured before XPS characterization for both devices are shown in Fig 5.7. Each device was measured over 15 min in 1X PBS. The PBS-stabilized device underwent 22 FGT scans and 4 EGT scans. The potential windows used for EGT and FGT inverters did not exceed ±0.5 V. The serotonin-dosed FGT measurements underwent 20 FGT scans and 5 EGT scans. FGT and EGT inverter curve overlap was evident after PBS stabilization for the first device and after 1 mM serotonin dosing for the second device (peak ΔV_{OUT} = –359 mV). The two devices exhibited differences in stabilization despite similar potential windows and number of scans, where the first device drifted more negatively in V_G (~150 mV) than the second device (~50 mV). The differences in FGT stability are not well understood, but we expect they stem from the FG2 sensing interface.

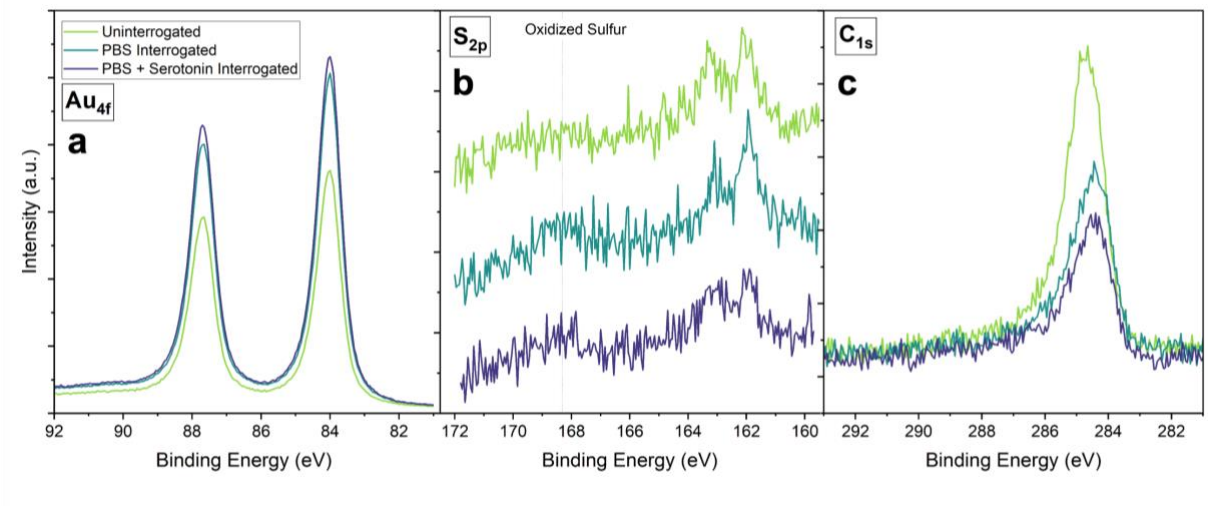

Figure 5.8. XPS of interrogated MCH-functionalized FG2 electrodes. XPS spectra of MCH-functionalized FG2 electrodes after functionalization (green), stabilization in 1X PBS (blue), and stabilization in 1X PBS and 5 min of 1 mM serotonin FGT measurements (purple). High-resolution spectra of (a) Au_{4f}, (b) S_{2p}, and (c) C_{1s} orbitals. Decreases in intensity of C_{1s} and increases in Au_{4f} peaks after interrogation indicate losses of MCH.

Evidence of MCH monolayer formation is shown in Fig 5.8 (green), the uninterrogated MCH-functionalized FG2 electrode. A high intensity C_{1s} peak at 284.7 eV is assigned to aliphatic carbon (C–C and C–H). The broad shoulder at 286.0 eV is characteristic of C–O and C–S bonds.[157] Monolayer formation is indicated by the S–Au characteristic doublet at 162.0 eV. Fig 5.8 also displays the high-resolution XPS spectra of MCH electrodes stabilized in 1X PBS (teal) and stabilized in 1X PBS followed with 1 mM serotonin introduction and sensing (purple). Opposing evidence of polyserotonin formation, the Au_{4f} doublet for interrogated electrodes had a larger intensity compared to the uninterrogated electrode. The 1X PBS interrogated electrode has a 44.7% increase in doublet area while the 1X PBS and serotonin interrogated electrode had a 52.9% increase in area, proposing a loss of thiol from both surfaces. This finding is corroborated with the lower intensity S–Au doublet in the S_{2p} spectra (–18.5%, –41.6%) and a lower intensity of all carbon in the C_{1s} spectra (–38.1%, –47.2%). In the S_{2p} spectra, there is also a low intensity peak

near 168 eV indicative of oxidized sulfur for both interrogated electrodes.[158] Finally, there is no observation of N_{1s} on the surface after serotonin interrogation, reducing the likelihood of polyserotonin formation at the interface.

These findings indicate that our observed stabilization period within 1X PBS was likely arising from a loss of surface-bound thiols as we continue to sweep the device. Because there are still characteristic S_{2p} and C_{1s} signals for MCH, there was not a complete loss of thiol. The XPS spectra of the 1X PBS- and serotonin-interrogated FG2 electrode pointed toward even higher losses, suggesting that the electrochemical nature of serotonin may have an impact on the stability of the functionalized surface. As bare gold FGTs exhibited EGT and FGT overlap, the directionality of the signals from serotonin are also suggestive of loss of surface-bound thiols. Additionally, as the stabilization of the second device did not lead to EGT and FGT overlap, but the introduction and interrogation with 1 mM serotonin did, we further evidence the loss of surface-bound thiols to stem from serotonin dosing.

We deduce the loss of thiols during stabilization to be the result of electrochemical interrogation where both the buffer and small molecule analyte, serotonin, can be variables, in addition to the potential, that elicit thiol reduction and/or oxidation. SAMs have reportedly undergone oxidative and/or reductive desorption at ~1.0 V and below –0.5 V, respectively.[63,159] The extent at which the electrolyte, surface density, and other electroactive molecules play a role in electrochemical desorption of thiols has not been well studied, as it can vary from one electrolyte/thiol system to another.[60] Vogiazi et al. find that the experimental conditions for electrochemical sensors (e.g., AC vs quasi-static DC potentials, concentration of redox reporter, buffer concentration) can lead to electrochemically-induced aptamer loss and, thus, signal losses that vary on a case-to-case basis.[68] EIS interrogation led to significantly more perturbation at the

surface than CV interrogation. Leung et al. narrow the potential window for EAB sensors operating in 1X PBS at 37 °C to –0.2 to –0.4 V based on changes in signal after 1500 scans using square wave voltammetry.[69]

To further rationalize our results, we consider the interactions serotonin and dopamine have with the sensing surface in both neutral and electrochemically-interrogated environments. Dopamine is one of many neurological catecholamines found to adsorb to gold surfaces.[160,161] Serotonin and dopamine have been measured with SERS where they adsorbed to gold substrates, producing characteristic Raman vibrational bands.[162–164] Serotonin has been reported as an electroactive molecule, producing faradaic currents from oxidation near 0.40 V in 0.2 M PBS and 0.22 – 0.23 V in Dulbecco's modified Eagle's medium (DMEM)[165,166] with gold working electrodes. Like other catecholamines,[167] dopamine is a highly electroactive molecule in PBS within the operating potential of ±0.5 V, and this property has been exploited for sensing with gold substrates.[168,169] These results call into question whether electrochemically active, small molecules can be detected with quasi-static DC platforms and gold sensing surfaces, like the FGT, without such nonspecific interactions. With this, we propose that serotonin and its electrochemical activity, that is within the potential bounds of FGT operation, was responsible for the dose-dependent serotonin FGT biosensor responses. This can be extended to the control cocktail, where electrochemically active dopamine may have been responsible for similar sensor responses. To verify this, an electrochemical characterization tool, such as CV, can be used to measure the state of the surface as it is interrogated and exposed to serotonin and other small, electroactive molecules. Loss of thiol can be characterized by the emergence of faradaic current generated by the oxygen reduction reaction in 1X PBS which is suppressed by a SAM on gold.[70]

5.5 Conclusions

Serotonin FGT biosensors were designed for charge-based responses to serotonin capture with a structure-shifting aptamer having a K_D of 360 nM.[153] The sensing surface was characterized with XPS and CV. Functionalization of the sensing electrode was also characterized by inverter curves that turn on at a more positive V_G compared to the EGT of the same device. Serotonin FGTs that do display a functionalization shift have concentration-dependent responses to serotonin (LOD = 2 μM); however, MCH-only and glyphosate aptamer/MCH FGT controls also produced concentration-dependent responses. Random, small responses are measured with bare gold FGTs. Furthermore, serotonin FGT biosensors respond to a cocktail of neurologically-relevant, small molecule analytes, suggesting the same mechanism eliciting responses from serotonin dosing may arise from analytes in the control cocktail. SPR characterizes the selectivity of the aptamer, finding responses toward ADP, dopamine, and histamine at 1 μM concentration that offer an explanation for responses to the control cocktail. XPS was used to characterize an MCH-functionalized FG2 electrode used in an FGT for 1X PBS stabilization and 1 mM serotonin sensing measurements, finding loss of MCH from the surface in both cases compared to an uninterrogated MCH FG2 electrode. Although the serotonin FGT biosensor may in fact relay the potentiometric response from serotonin-aptamer complexing, the evidence of signals from other functionalized FGTs introduces a separate, compounding mechanism that must be understood in order to design aptamer-based FGTs for small molecule detection. Currently, the signals arising from functionalized FGTs after exposure to serotonin are speculated to stem from the electrochemically-induced loss of surface-bound thiols from the surface, as serotonin is an electroactive species. This can be tested by using CV to electrochemically interrogate the various

functionalized surfaces with and without 1 mM serotonin in the 1X PBS electrolyte. This can also be extended toward other small, electroactive analytes, such as dopamine.

Chapter 6: Electrochemical Interrogation of Functionalized Surfaces

6.1 Introduction and Motivation

Electrochemical sensing platforms, such E-AB sensors and EGTs, are on the rise due to their enhanced sensitivity, broad applicability, and potential for portability and in situ sensing. The use of electric fields is key to operating these devices, where signal transduction is a result of changes in current or potential at the recognition interface. Electrochemical interrogation of the sensing surface with a quasi-dynamic potential, even within ± 1V, can enable undesired electrochemical events at the interface, as noted in Section 1.4. The destruction of SAMs has originated from potentials causing reductive (below –0.5 V)[159] or oxidative (~ 1 V) desorption [63] of the thiols within aqueous electrolytes. These potentials vary on a case-to-case basis, as the electrolyte solution (pH, composition),[60,63] thiol type,[63,159,170] and interrogation method[67,68] can affect the stability of the monolayer. Considering both the stabilization period and nonspecific FGT signals observed in Chapter 5, it is worth considering if reductive and oxidative desorption are occurring during FGT sensing, as depicted in Fig 6.1.

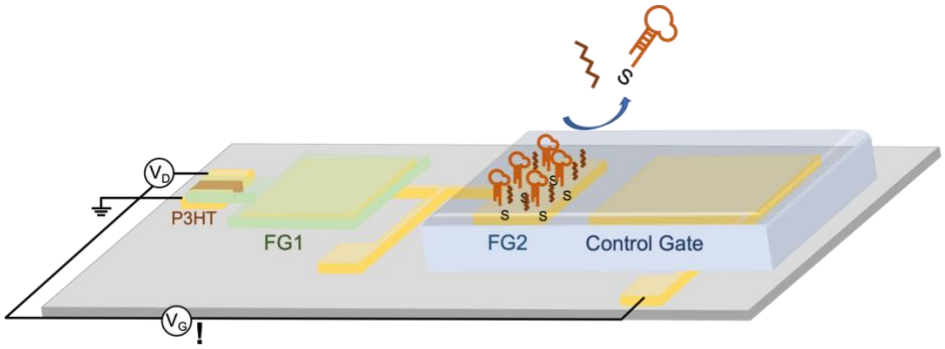

Figure 6.1. Schematic representation of electrochemically-induced thiol desorption in an FGT. Desorption of surface-bound aptamers and other thiols from the sensing surface, FG2, as a result of electrochemical interrogation (V_G) in an aqueous electrolyte.

In this chapter, we discover the potential windows that electrochemically disrupt common sensing surfaces: antibody- and aptamer-based. This chapter is mainly focused on aptamer/MCH-functionalized electrodes. Cyclic voltammetry is used to apply and sweep quasi-static potentials to the functionalized gold substrates. Functionalized gold electrodes were electrochemically interrogated, tuning parameters such as the potential window and sweep rate to observe effects on characteristic peak potentials from faradaic reactions. One of the commonly-used buffers for biosensing, 1X PBS, was used as the electrolyte to better translate these processes to the sensing surface of the FGT biosensor. Studies were conducted with the redox active chemical, $[Fe(CN)_3]_6^{3-/4-}$, where changes in peak potentials from redox events at the surface, E_p, allow for ease in tracking surface destabilization. Redox-active moieties, typically conjugated to aptamers for EAB sensors, have reportedly caused changes in signal with electrochemical interrogation using square-wave voltammetry (SWV).[66] Furthermore, 1X PBS with and without $[Fe(CN)_3]_6^{3-/4-}$ have exhibited different effects on the stability of the aptamer surface for reasons not yet understood.[68] As such, electrochemical interrogation experiments were replicated in 1X PBS only to determine whether $[Fe(CN)_3]_6^{3-/4-}$ interacts unfavorably with the sensing interface. Each surface exhibits different stability, and we find aptamer/MCH surfaces have more narrow safe operating potential windows than 11-MUA and antibody surfaces.

These estimated safe operating potential windows can be translated to the potential felt at FG2 of the FGT, prompting future work to examine the electrochemical stability of the sensing interface prior to its integration in an FGT biosensor. It is important to note that the sensing surface, FG2, experiences the opposite polarity of the potential applied at the control gate, V_G. Both negative and positive polarities are explored in order to set parameters for both p-type and n-type transistors and to collect information on both reductive and oxidative desorption. Furthermore,

p-type FGTs have operated within ±1 V and not exclusively at negative potentials. With this, it is also crucial to set boundaries for potentials that can electrochemically alter and damage the surface, and thus alter the gating of the FGT, producing false signals or stabilization periods.

6.2 Experiments

All aptamer/MCH-functionalized electrodes were photolithographically patterned with the same protocol as Section 2.1. The area of the working electrode immersed in the electrolyte was 0.25 mm x 0.25 mm. Functionalization was carried out in a PDMS well as described in Section 5.2 for serotonin FGT biosensors, where aptamer-only and MCH-only self-assembly were overnight (16-18 h) and 1 h, respectively. All 11-MUA and antibody-functionalized electrodes were e-beam evaporated, as described in Section 2.1. Functionalization was carried out as described in Section 4.2 for glyphosate FGT biosensors. The area of the electrode was ~1 cm x 1 cm with ~1/3 of the electrode immersed into the electrolyte. Both types of electrodes were used for MCH-only and aptamer-only functionalized electrodes. All electrodes were dried with N_2 after functionalization and stored under negative pressure (–30 in Hg) in a dark antechamber before immediate use.

CV was conducted as described in Section 2.10. The electroactive species was 10 mM $K_3[Fe(CN)_6]$. The electrolyte was 1X PBS (pH = 7.4, 0.2 µm filtered). The working electrode was the functionalized electrode. Working electrodes were electrochemically interrogated by applying a sweeping working potential (vs Ag/AgCl) over a potential window, including a forward and backward sweep for each scan, for a total of 20 subsequent scans having a sweep rate of 25 mV/s. To test positive potential bounds, the sweeps started at –0.2 V and reached +0.4 V before sweeping back, where the positive potential was extended by +0.1 V until reaching +0.9 V. To test negative

potential bounds, the sweeps started at +0.2 V and reached at –0.4 V before sweeping back, where the positive window was extended by –0.1 V until reaching –0.9 V. Portions of the aptamer-only and MCH-only work were conducted by J.H.

6.3 Results and Discussion

To realize whether potentials used for gating with 1X PBS cause reconstruction and/or destruction of our functionalized surfaces, CV was used to interrogate the aptamer/MCH surface for different potential windows, mirroring similar studies for EAB sensors.[68,69] CV was used based on its ability to replicate the quasi-static sweep rates and potential windows used for FGT sensing while using the faradaic currents measured from electrochemical reactions to monitor the state of the working electrode surface. These studies were conducted with and without 10 mM $K_3[Fe(CN)_6]$ in solution, as $[Fe(CN)_6]^{3-/4-}$ has reportedly caused gold etching at positive potentials and interference with electrochemical detection methods.[171–174] Free CN^- and the oxidation of metallic Au to Au^+ can lead to the formation of soluble $Au(CN)_2^-$, as laid out by the Elsner reaction:[171]

$$4\ Au + 8\ CN^- + 2\ H_2O + O_2 \rightarrow 4\ Au(CN)_2^- + 4\ OH^- \qquad (6.1)$$

The reason to use $K_3[Fe(CN)_6]$ is to track characteristic reduction and oxidation potentials of $[Fe(CN)_6]^{3-/4-}$ in order to grasp how the surface is changing with interrogation. Compared to bare gold, charge transfer is impeded when the surface is functionalized with molecules, like thiols. The denser and thicker the functionalized layer, the more difficult it is for charge transfer between gold and $[Fe(CN)_6]^{3-/4-}$ to occur, either necessitating larger potentials to achieve charge transfer or charge transfer not occurring at all.

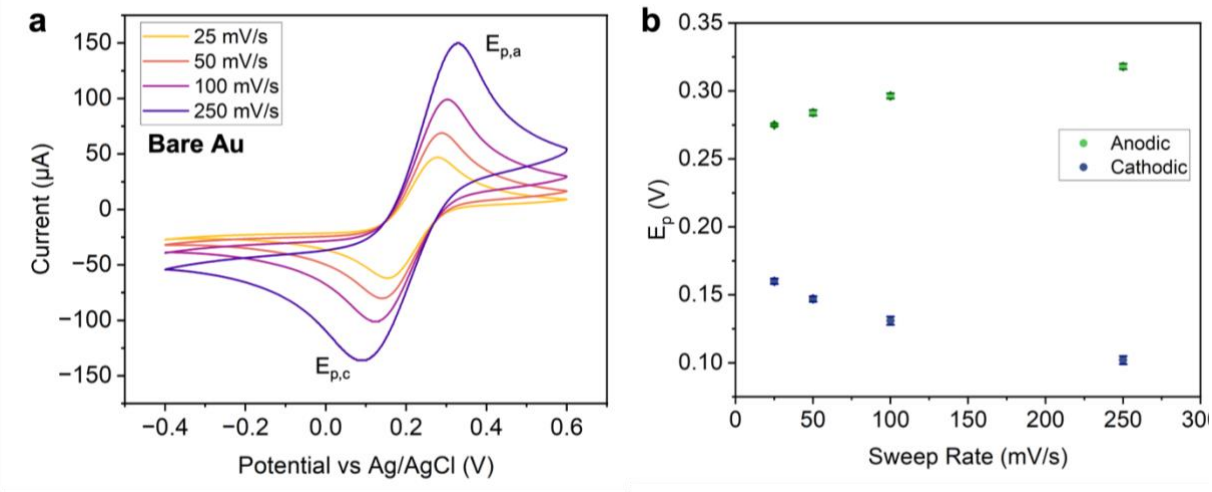

Figure 6.2. CV of bare gold electrodes with 10 mM $[Fe(CN)_6]^{3-/4-}$. (a) Voltammograms from 25 mV/s to 250 mV/s, showing changes in the characteristic E_p and current. (b) E_p for the anodic and cathodic peaks for bare gold electrodes. The error represents the standard deviation of three samples.

Initially, bare gold working electrodes were measured to characterize the redox potentials of 10 mM $[Fe(CN)_6]^{3-/4-}$ in 1X PBS. This was done from 25 mV/s to 250 mV/s, as shown in Fig 6.2. As expected, the peak-to-peak separation, ΔE_p, increases with increasing sweep rate. Among four gold samples measured with a sweep rate of 25 mV/s, the average anodic peak ($E_{p,a}$) was 276 ± 2 mV, and the average cathodic peak ($E_{p,c}$) was 159 ± 2 mV. These characteristic potentials can be used as a reference to rationalize whether thiol desorption has occurred, leaving bare gold sites. The characteristic peak potentials were also determined for aptamer/MCH surfaces. Among 36 samples measured with a sweep rate of 25 mV/s, the average $E_{p,a}$ and $E_{p,c}$ were 593 ± 29 mV and –245 ± 39 mV, respectively. The following electrochemical interrogation studies used a sweep rate of 25 mV/s and a total of 20 scans for all interrogation runs, as this provides a relevant sweep rate for FGTs[21,45] and relevant number of scans for FGT sensing.

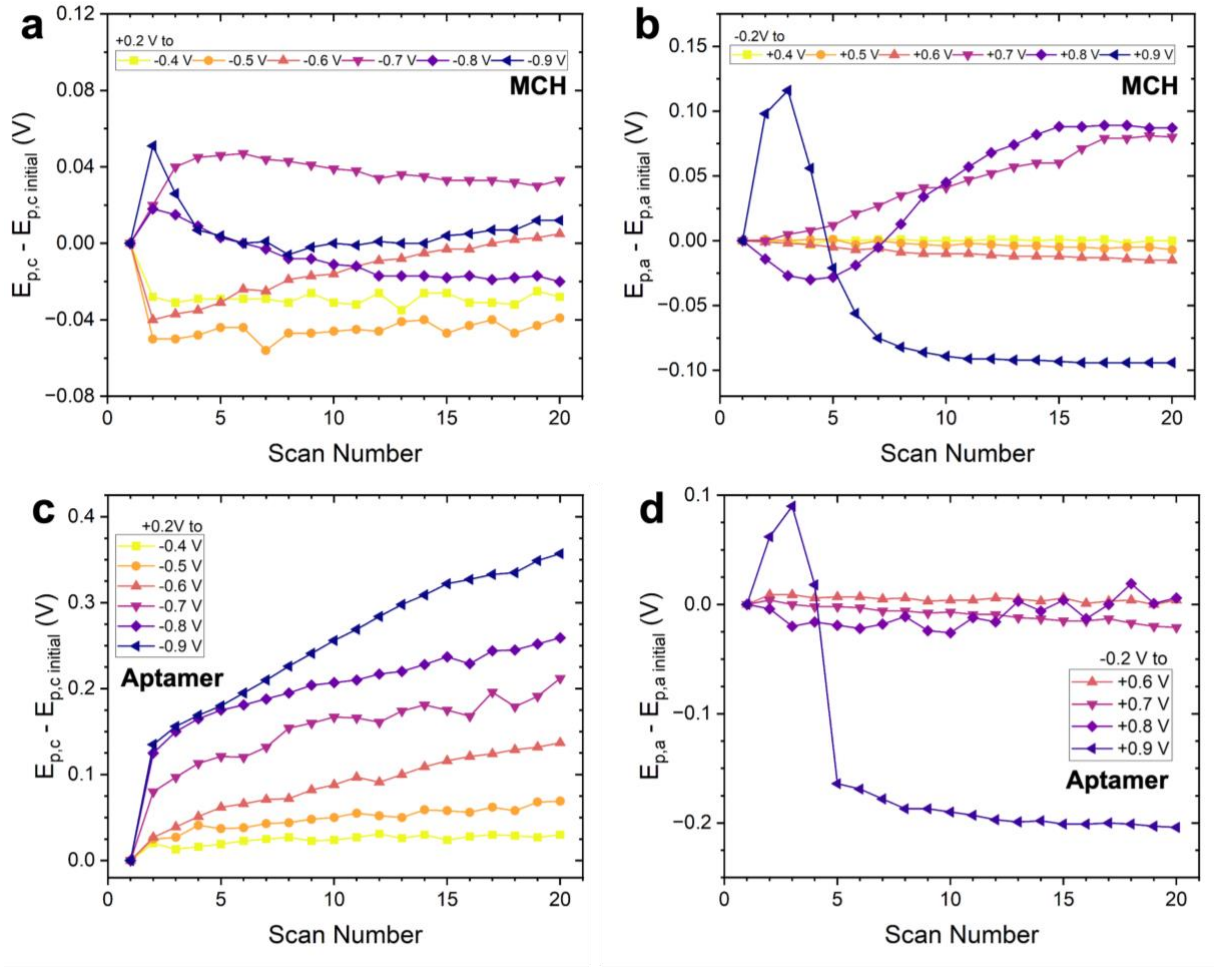

Figure 6.3. Electrochemical stability of MCH-only and aptamer-only functionalized gold electrodes in 1X PBS with the redox reporter. The stability of MCH electrodes interrogated with extending (a) negative and (b) positive potential windows. The stability of aptamer electrodes interrogated with extending (c) negative and (d) positive potential windows. The electrodes were interrogated over 20 scans, and the change in E_p was measured with respect to the first scan. The sweep rate was 25 mV/s, the electrolyte was 1X PBS, and the redox reporter was 10 mM $[Fe(CN)_6]^{3-/4-}$.

The results of MCH-only and aptamer-only functionalized gold electrodes are included in Fig 6.3. The trends observed with MCH electrodes and aptamer electrodes were reflected in aptamer/MCH electrodes, serving as another indication of both molecules being bound to the surface. As E_p for MCH electrodes were near that of bare gold (Fig 5.3), changes in $E_{p,c}$ were

smaller (Fig. 6.3a and b). Interestingly, this observation also indicates that the two molecules were undergoing independent phenomena under electrochemical interrogation in 1X PBS with $[Fe(CN)_6]^{3-/4-}$, meaning that the electrochemical interactions occurring in solution are not totally generalizable to surface-bound thiols, consistent with the literature.[63,159,170]

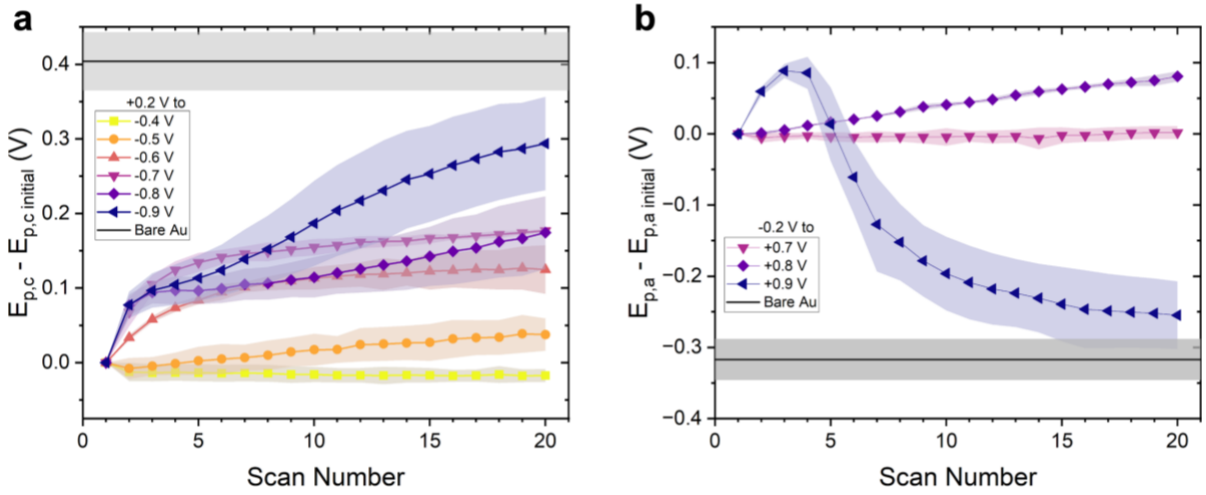

Figure 6.4. Electrochemical stability of aptamer/MCH-functionalized gold electrodes in 1X PBS with the redox reporter. The stability of aptamer/MCH electrodes interrogated with extending (a) negative and (b) positive potential windows. The sweep rate was 25 mV/s, the electrolyte was 1X PBS, and the redox reporter was 10 mM $[Fe(CN)_6]^{3-/4-}$. The electrodes were interrogated over 20 scans, and the change in E_p was measured with respect to the first scan. Error is the standard deviation among three electrodes. The bare Au lines represents the E_p difference between aptamer/MCH and bare Au electrodes.

Fig 6.4a follows the change in $E_{p,c}$ with sweeping and extending the negative end of the potential window. At negative potentials, we expect the reductive desorption of thiols. With the –0.4 V bound, there was little change in $E_{p,c}$ over 20 scans. Up to the –0.5 V bound for MCH electrodes, $E_{p,c}$ became more negative. For the –0.6 V and –0.7 V bounds, $E_{p,c}$ shifted positively with scanning; whereas, $E_{p,c}$ for –0.8 V and –0.9 V bounds remained near the initial $E_{p,c}$ with scanning. This perhaps explains why the –0.8 V data for aptamer/MCH electrodes overlaps with –0.6 V and –0.7 V data rather than showing more positive shifts in $E_{p,c}$ with extending the negative

potential window, as observed with aptamer electrodes (Fig 6.3c and d). As the potential window becomes increasingly negative, the $E_{p,c}$ shifts positively toward that of bare gold (black). With this, electrochemical interrogation with potentials beyond –0.4 V, where $E_{p,c}$ decreases, destabilize the aptamer/MCH interface likely in the form of thiol desorption.

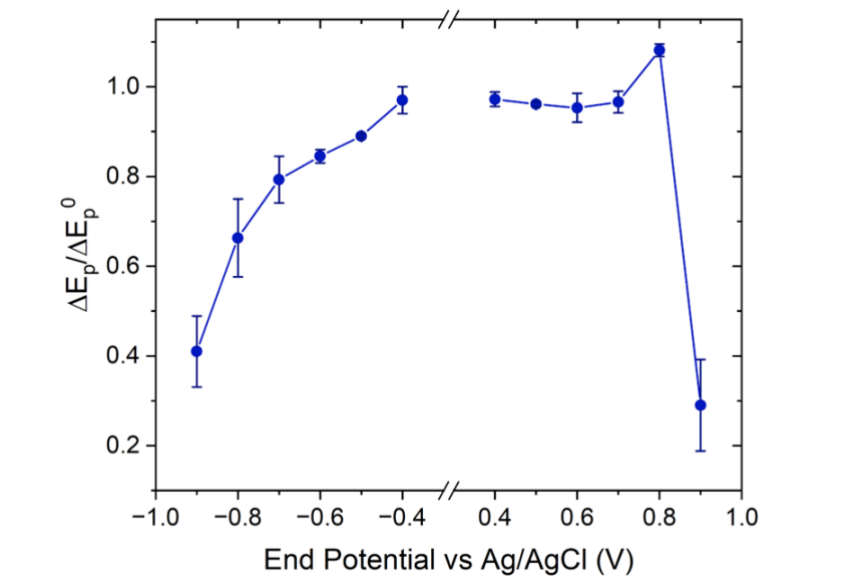

Figure 6.5. Changes in ΔE_p after the interrogation of aptamer/MCH electrodes for each potential window. The change in ΔE_p of the full voltammogram (+0.4 to –0.7 V) before and after electrochemically interrogating over 20 scans. The end potential was the extended positive or negative potential bound. The error represents the standard deviation of three electrodes.

For the positive potential windows in Fig 6.4b, $E_{p,a}$ cannot be tracked until extending the window to –0.7 V. As such, voltammograms from –0.4 V to +0.7 V were measured before and after the 20 scan interrogation in order to identify changes in ΔE_p for potential windows that do not contain either anodic or cathodic peaks (Fig 6.5). The change in ΔE_p among the negative potentials corroborate results in Fig. 6.3a, where the aptamer/MCH surface destabilized beyond the –0.4 V bound. For positive potential bounds with unmeasurable $E_{p,a}$ (+0.4 to +0.6 V), the

change in ΔE_p before and after interrogation was steady with an average –5 ± 3% decrease after interrogation with the +0.6 V bound.

Beyond +0.6 V in Fig 6.4b, aptamer/MCH electrodes followed similar trends observed with MCH electrodes in Fig 6.3a and b. Interestingly, MCH electrodes exhibited negative shifts in $E_{p,a}$ up to the +0.6 V bound. At the +0.8 V bound, $E_{p,a}$ shifts positively ~100 mV over 20 scans for aptamer/MCH and MCH electrodes, increasing ΔE_p. This observation persisted three scans into interrogation with the +0.9 V bound for aptamer/MCH, aptamer, and MCH electrodes. This observation cannot be a result gold etching since the increase in electrode area would result in facilitated charge transfer, decreasing ΔE_p. A past report finds aptamer/MCH SAMs undergo time-dependent reorganization after self-assembly, increasing charge transfer resistance as measured by EIS.[175] An increase in ΔE_p may have risen from potential-induced reconstruction of the thiols[176] or interactions between $[Fe(CN)_6]^{3-/4-}$ and the surface that are not well understood. The positive shifts in $E_{p,a}$ were also ~100 mV before continued interrogation led to an approximate –300 mV $E_{p,a}$ shift, nearing bare gold. Similarly, aptamer electrodes experienced rapid negative shifts in $E_{p,a}$ at the +0.9 V bound, reaching approximately –200 mV. As such, the aptamer/MCH surface was considered unstable beyond +0.7 V, also reflected in Fig 6.5, where thiol desorption and/or gold etching are likely responsible for ΔE_p decreasing beyond the +0.8 V bound.

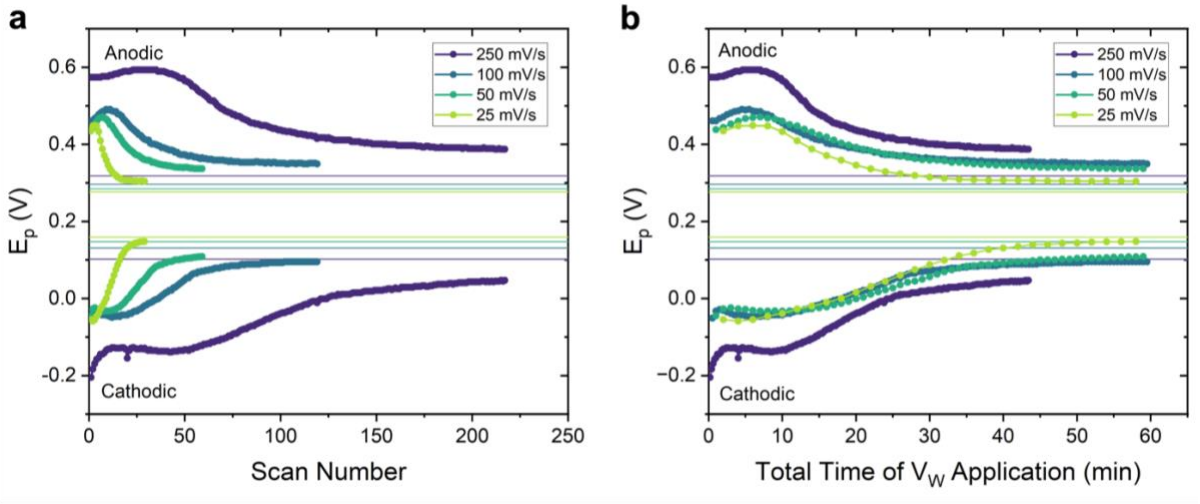

Figure 6.6. Electrochemical stability of aptamer-functionalized gold electrodes with varied sweep rate. The sweep rate was varied from 25 mV/s to 250 mV/s, the electrolyte was 1X PBS, and the redox reporter was 10 mM $[Fe(CN)_6]^{3-/4-}$. The potential window was –0.7 V to +0.8 V. The lines represent the characteristic E_p for bare gold electrodes for each sweep rate. Changes in E_p versus (a) number of scans and (b) total time the working voltage (V_w) was applied. Each sweep rate represents a single sample.

Sweep rate dependent measurements were done with aptamer-only electrodes using a potential window of –0.7 V to +0.8 V, shown in Fig 6.6. Interestingly, ΔE_p increases initially for scans with sweep rates faster than 25 mV/s, also suggesting structural reorganization. With sustained scanning, the change in ΔE_p for each scan is smaller for faster sweep rates. As such, higher sweep rates are able to sustain more sweeps before ΔE_p decreases. When the change in ΔE_p is plotted against the time exposed to the electric field rather than the scan number, the effects are the same among all sweep rates. As such, the rate of thiol loss is dependent on the amount of time the potential is applied. For FGT sensing purposes, this provides insight into limiting the potential-induced surface destruction. As shown earlier in Fig 3.8, EGTs can operate from 25 mV/s to 150 mV/s. As such, we expect that FGT sensors can tolerate a higher number of sweeps before inducing changes in the surface at higher sweep rates.

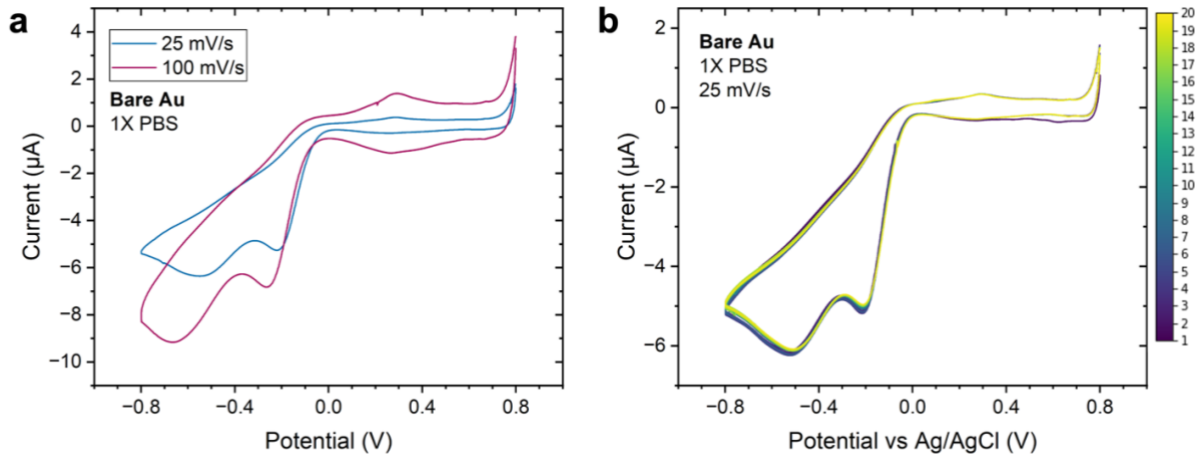

Figure 6.7. Interrogation of bare gold working electrode with CV in 1X PBS. (a) Voltammograms of bare gold electrode with a sweep rate of 25 mV/s and 100 mV/s. (b) Interrogation of bare gold electrode over 20 scans with a sweep rate of 25 mV/s. The electrolyte was 1X PBS.

Experiments were replicated in 1X PBS without $K_3[Fe(CN)_6]$ for aptamer/MCH-functionalized gold electrodes. Fig 6.7a shows the full voltammogram for bare gold working electrodes with sweep rates of 25 mV/s and 100 mV/s. Here, there are two characteristic peaks to identify faradaic reactions between bare gold and 1X PBS near –0.2 V and –0.6 V. The reaction near –0.2 V is the electrochemical reduction of O_2 to H_2O_2 catalyzed by gold:[70,170]

$$O_2 + 2H^+ + 2e^- \rightleftharpoons H_2O_2 \qquad (6.2)$$

Among four bare gold samples, the characteristic potentials for the peak near –0.2 V at sweep rates of 25 mV/s and 100 mV/s are –225 ± 4 mV and –270 ± 5 mV, respectively. The characteristic potential for the peak near –0.6 V at sweep rates of 25 mV/s and 100 mV/s are –569 ± 23 mV and –686 ± 15 mV, respectively.

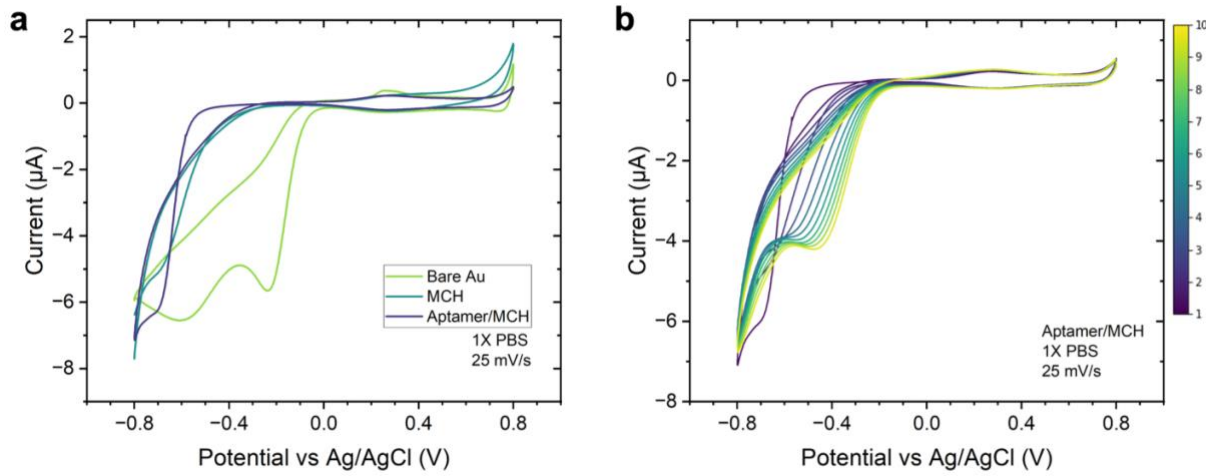

Figure 6.8. CV of functionalized electrodes in 1X PBS. (a) Bare gold (green), MCH, and aptamer/MCH electrode voltammograms. (b) Ten consecutive voltammograms of an aptamer/MCH electrode. The voltammogram evolves to include a local peak near –0.4 V that is characteristic in the bare gold voltammogram.

In Figure 6.8a, both the MCH and aptamer/MCH electrodes showed suppression of the oxygen reduction reaction (ORR), with a minor observable emergent peak near –0.7 V. Fig 6.8b demonstrates that aptamer/MCH-functionalized gold electrodes were unstable for sweeps from ±0.8 V in 1X PBS, where there was an emergence and growth of the ORR peak after 10 scans with a sweep rate of 25 mV/s. With knowledge that interrogation in 1X PBS in itself can induce changes in the aptamer/MCH surface that are observable within the voltammogram, we proceeded with electrochemical interrogation at the various potential windows.

Because the two peaks are not observable within most of the potential windows used and are also suppressed by the functionalized surface, current was instead tracked as a function of scan number. Instead of searching for a local maximum, we instead characterized stability by an increase in current between –0.2 and –0.6 V, similar to past work on monitoring electrochemical desorption of thiols in biological fluids.[70] For the positive potential windows, the current at –0.2 V

was tracked; whereas, for the negative potential windows, the current at –0.4 V was tracked. As monolayer desorption continues, more electrocatalytic sites are available for oxidation reduction. Increases in faradaic current indicate the emergence of a peak, serving as an identifier for surface instability.

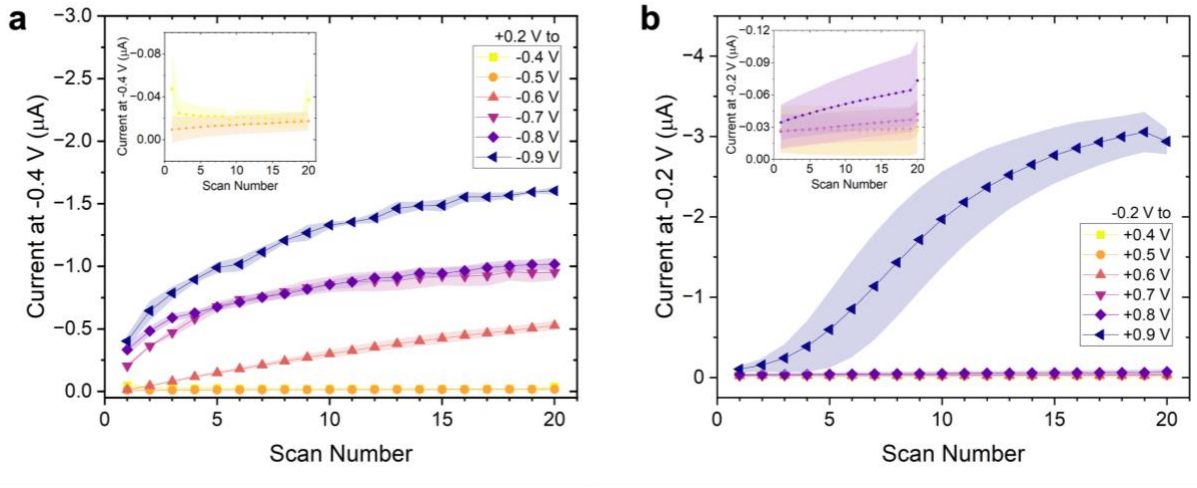

Figure 6.9. Electrochemical stability of aptamer/MCH-functionalized gold electrodes in 1X PBS. The sweep rate was 25 mV/s, and the electrolyte was 1X PBS without a redox reporter. (a) Changes in current measured at –0.4 V for negative potential windows. (b) Changes in current measured at –0.2 V for positive potential windows. The inset enlarges the lower current data from –0.4 to +0.8 V. The error represents that standard deviation of 3-4 samples.

As indicated in Fig 6.9, the current becomes increasingly negative beyond –0.5 V and +0.8 V bounds over 20 scans for aptamer/MCH electrodes. Notably, the current on the first sweep was more negative as the potential becomes increasingly negative beyond –0.6 V, indicating that even the first forward scan had a significant impact on the surface. The full voltammogram (+0.8 V to –0.8 V) was measured after interrogation to further demonstrate changes in the surface for potential windows not containing the characteristic peaks (Fig 6.10), especially for the positive potential windows. After interrogation with each potential window, the changes of the full voltammogram were compared to uninterrogated aptamer/MCH. Potentials windows beyond

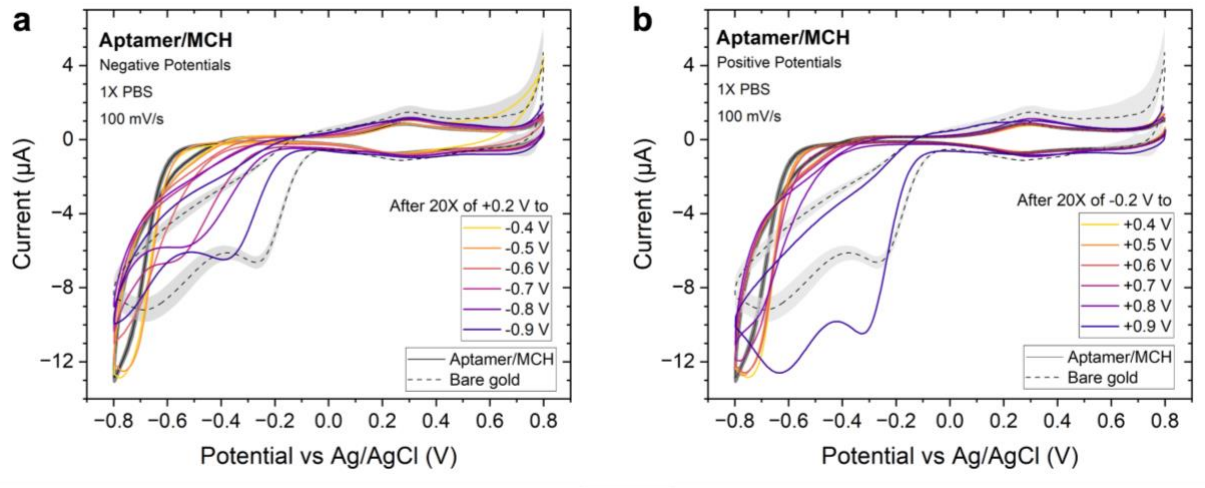

Figure 6.10. Full voltammograms of aptamer/MCH-functionalized electrodes before and after electrochemical interrogation in 1X PBS. Full voltammograms after interrogating at various (a) negative and (b) positive potential windows over 20 scans. The sweep rate was 100 mV/s, and the electrolyte was 1X PBS. The error of the aptamer/MCH and bare gold voltammograms represents the standard deviation of 10 and 4 electrodes, respectively. All other voltammograms are each of a single electrode.

–0.5 V and +0.6 V caused significant changes to the full voltammogram wherein the current at –0.8 V decreased and there was emergence of an ORR peak. After interrogation at the +0.9 V bound, the current density of the ORR peak and –0.6 V peak were higher than that of bare gold. In a report by Tencer et al. where the electrochemical stability of 1-dodecanethiol in 1X PBS was studied, Cl^- ions in 1X PBS are proposed to have caused the complex of Au^{3+} as follows,

$$Au + 4\ Cl^- \rightarrow\ [AuCl_4]^- + 3e^- \qquad (6.3)$$

with a potential of +0.78 V vs Ag/AgCl, leading to a total loss of Au when the applied potential was +0.8 V over 5 min.[60] Dissolution of Au was not observed in this study; however, further characterization should be done to confirm whether Au etching occurs at positive potential bounds, such as with atomic force microscopy (AFM).

There were discrepancies between the use of and lack of 10 mM $[Fe(CN)_6]^{3-/4-}$ in solution with 1X PBS for electrochemically interrogating aptamer/MCH electrodes. In extending the positive potential bound, 1X PBS did not capture unusual electrochemical characteristics observed from MCH where ΔE_p increased, suggesting that it stemmed from interactions between $[Fe(CN)_6]^{3-/4-}$ and the surface. In extending the negative potential bound, changes in the surface when observed by tracking $E_{p,c}$ and ΔE_p were more evident with the redox reporter. On this point, the use of a redox reporter can provide additional evidence of surface reconstruction and greater sensitivity through the well-characterized ΔE_p marker that an aqueous buffer itself cannot. On the other hand, electrochemical interrogation with CV in 1X PBS was able to provide information on the stability of aptamer/MCH electrodes that redox reporters may have shielded through their own unfavorable interactions with the surface. Overall, these results revealed that aptamer/MCH electrodes electrochemically interrogated in 1X PBS are unstable, and that potential windows used in this study likely induce thiol desorption in the aptamer/MCH-functionalized electrode after 20 scans at 25 mV/s.

The electrochemical stability of SAMs indicate that highly ordered monolayers exhibit greater stability.[63] To compare the results of the two sensing studies, experiments were also replicated for 11-MUA and glyphosate antibody-functionalized gold electrodes with 1X PBS and 10 mM $[Fe(CN)_6]^{3-/4-}$. Voltammograms of 11-MUA only (Figs E.1 and E.2) and antibody electrodes (Figs E.3 and E.4) interrogated over 20 scans show greater resistance to the potentials affecting aptamer/MCH electrodes. Due to the lack of E_p for most of the potential windows, stability was determined by the emergence of E_p. The approximate safe operating potential window for 11-MUA is –0.6 V to +0.7 V. For antibody electrodes, the surface was stable up to +0.7 V and as low as –1.0 V, even more resistant than 11-MUA. After a few scans reaching the +0.9 V

boundary, voltammograms contained peaks that shift toward those characteristic of bare gold and $[Fe(CN)_6]^{3-/4-}$ for both the antibody and 11-MUA electrodes, suggestive of gold etching. The enhanced stability of these electrodes compared to aptamer/MCH electrodes is rationalized as differences in packing density where longer alkyl chain lengths have enabled greater packing density due to increased van der Waals forces between the alkyl chains, lending less structural disorder.[63] Furthermore, the alcohol end group of MCH has been rationalized to worsen the stability of the interrogated aptamer electrodes in biological fluids compared to using methyl-terminated hexanethiol as a backfilling thiol.[70] However, these experiments, and those done for MCH and aptamer electrodes, should be replicated in 1X PBS only to gain additional insight into the electrochemical stability without compounding, undesirable $[Fe(CN)_6]^{3-/4-}$ interactions.

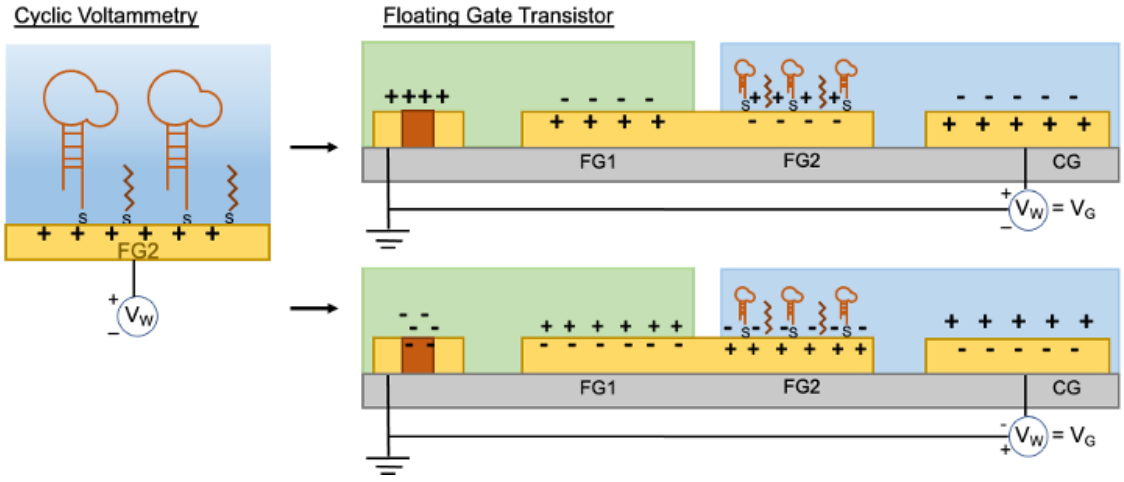

Figure 6.11. Comparing CV to FGT electrochemical interrogation. Translation of the working electrode potential, V_W, to the FG2 interface of a p-type FGT, where the applied potential is applied to the control gate rather than to the sensing surface. The two modes represent the FGT in the (a) OFF state and the (b) ON state.

To roughly translate these potentials to the FG2 interface of an FGT (Fig 6.11), we first consider the application of V_G. As it is applied to CG, the opposite polarity is in turn felt at the FG2 interface as a result of capacitive coupling. Thus, for the case of operating at 25 mV/s with

1X PBS, the potential bounds for safely operating an aptamer/MCH FGT within 20 sweeps is roughly set to –0.7 V to +0.5 V. When operating the EGT of an FGT, V_G is applied directly to the floating gate, so the potential bounds are of the same polarity, –0.5 V to +0.7 V. This consideration should be accounted for when measuring the EGT to determine the extent of functionalization and its stability over the sensing period. It is important to note these potentials are vs Ag/AgCl; whereas, the FGT does not have a reference electrode. Solution resistance between CG and FG2 may alter the potential felt at the sensing interface; however, the bare gold FGT and EGT have good coupling with the design implemented toward glyphosate and serotonin detection, indicating potential losses are minimal.

In the earlier work for FGTs, inverter curves measured with a sweep rate of 25 mV/s with V_G extended as far as ±1.0 V.[21,45] However, inverter curves of glyphosate and serotonin FGTs typically operated with potential windows within ±0.6 V, and the sweep rate used for these studies was 100 mV/s, providing a safer electrochemical environment for sensing. As shown in Section 5.4, interrogation of the FGT and EGT-subunit within ±0.5 V led to losses of MCH at the sensing surface as confirmed by XPS. To better translate CV potentials, the floating gate potential (V_{FG}) can be measured as V_G swept, monitoring how V_{FG} changes with interrogation over the sensing medium. To further characterize and quantify the extent of monolayer loss, XPS can be used to measure the high-resolution spectra of the Au_{4f}, S_{2p}, and C_{1s} orbitals of the FG2 surface after interrogation at each potential window. AFM can be used to determine if there was etching of gold from the surface. A library of different types of backfilling thiols can be explored in order to enhance the electrochemical stability of aptamer/MCH electrodes. Design considerations for the sensing surface include all functionalization conditions: type of thiol(s), solvent, surface cleaning method, and self-assembly time.

CV studies should also be extended to solutions containing electrochemically active target analytes, such as serotonin and dopamine, to gather whether reduction and/or oxidation of these analytes can also damage the functionalized surface by inducing thiol reduction or oxidation.

6.4 Conclusions

Electrochemical interrogation of functionalized interfaces can lead to the structural changes or losses of surface-bound thiols, as made evident by CV. Changes in voltammograms for differing potential windows indicate problematic potentials for both negative and positive voltages in 1X PBS with and without the redox reporter, $[Fe(CN)_6]^{3-/4-}$. The use of the $[Fe(CN)_6]^{3-/4-}$ does play a significant role in the stability of the interface, as the results do not align with those measured in 1X PBS only. Specifically, interactions between $[Fe(CN)_6]^{3-/4-}$ and aptamer/MCH at positive potentials caused an increase in ΔE_p that masked the desorption observed in 1X PBS at these potentials. The safe operating potential window determined by CV in 1X PBS for aptamer/MCH electrodes was roughly –0.5 V to +0.7 V. While these results indicate a general issue of using CV for bio/chemosensing, these potential windows can be translated to the FGT, where the sensing interface experiences the opposite polarity of the applied potential, V_G. As such, we predict that FGT biosensors seemingly necessitating a stabilization period are likely suffering from similar electrochemical losses observed with CV.

To better design future electrochemical stability studies, we can look toward other forms of characterization to validate the safe operating potential windows set by CV and to gain insight into the mechanisms causing surface destruction, such as thiol desorption and gold etching. To validate CV results, surface characterization tools, such as XPS and AFM, can be utilized after FGT interrogation to characterize surface deconstruction, as was done in Section 5.4 for MCH

FGTs examined by XPS. SAMs composed of 11-MUA and antibody-conjugated electrodes exhibited stability at potentials beyond those destructive to aptamer/MCH with 10 mM $[Fe(CN)_6]^{3-/4-}$, providing insight into future sensing surface design considerations to mitigate electrochemical losses.

Chapter 7: Final Remarks and Outlooks

7.1 Summary

The FGT biosensor is a promising platform compared to other transistor-based biosensors due to the physical decoupling and electronic coupling of the signal transducer and biorecognition chamber. The signal transduction element, the EGT, can be easily fabricated through aerosol jet printing, while signals can be translated and amplified sub-1V due to the high transconductance (or gain) of the device. The floating gate enables compartmentalization of the EGT and sensing medium, preventing contamination of the EGT by the aqueous electrolyte and sample. Furthermore, independent engineering of each compartment has allowed us to directly characterize and optimize individual components of the device. In this regard, it is clear the platform is currently stunted by issues within the sensing compartment that have challenged small molecule sensing.

The FGT biosensor has demonstrated its efficacy as a biosensor through the detection of DNA,[42] gluten,[27] and ricin.[28] To further understand the sensing mechanism, FGT models were developed that take the FGT architecture, EGT materials, and inverter components into consideration, paving a path toward signal amplification of charge- and capacitance-based signals.[21,44,45] These models utilized data from FGTs functionalized with self-assembled monolayers (SAMs) whose tailorable lengths dictated capacitance-based sensing and pH sensitive tail groups dictated charge-based sensing. However, limitations in the form of biasing, sensing surface composition, and aqueous electrolyte use present additional variables for consideration when designing the platform, especially toward small molecule detection. Overall, small molecule detection with an FGT biosensor necessitates both strong consideration of the sensing surface and the means of electrochemical interrogation in order to overcome the present sensing limitations.

The first study explored the signal transduction element, the EGT. Past studies found that there are potential losses between the EGT and FGT of the same device, and these losses were thought to be a result of charge lost to a parasitic capacitance between the floating gate and the underlying p-doped Si wafer. It was shown that these losses are amplified when the area of the second floating gate interface (FG2) is decreased on both SiO_2/Si and an insulating substrate (glass), as expected. However, the estimate fraction of charge lost to parasitic capacitance (f) was large for glass substrates. Rather, the source for potential losses stemmed from uncertainties in the specific capacitances of the P3HT/ion gel and ion gel/gold interfaces, allowing us to eliminate f from FGT models.

To further address the practical use of printed EGTs as commercial signal transduction elements, the short- and long-term stability was investigated. EGTs stored in ambient air operated over 30 days but exhibited fluctuations in their mobility and threshold voltage (V_T). When measured in ambient vs N_2 (glove box), the transfer curves of the same EGTs vary dramatically. More so, after exposure to a high humidity environment, the same EGTs also experience reversible changes to their transfer curve characteristics, indicating that environmental factors, such as humidity and light, can impact the day-to-day operation of EGTs. Long-term, EGTs can be stored in the glove box up to 6 months while still operating suitably for signal transduction, allowing for mass fabrication of EGTs without concerns over shelf life. Finally, EGTs can be measured with sweep rates as high as 150 mV/s with minor impacts on hysteresis, decreasing measurement times. These two results thus addressed important issues in device stability and detection time that were not considered in previous experiments on the FGT platform.

The second study aimed to achieve detection of the small charged molecule, glyphosate, using an antibody-based FGT. As the presence of the capture agent, the glyphosate antibody, was

the primary component for biorecognition, the surface chemistry was carefully characterized to ensure the conjugation of the antibody. The mixed monolayer of 11-MUA and PEG thiol was characterized with XPS. Reacting the carboxylic tail group of 11-MUA with a mixture of EDC and NHS (pH = 5.8) led to a NHS ester tail group, whose characteristic vibrational bands and stretches were characterized by RAIRS. The NHS ester group is readily substituted with the lysine residue of the antibody, conjugating the antibody to the SAM through an amide bond. Antibody presence on the surface was characterized with RAIRS and XPS on control substrates and the FG2 electrode, proving that the surface chemistry can be translated to a millimeter sized electrode using a PDMS well as a vessel. The glyphosate FGT biosensor exhibited low and irreproducible signals when exposed to 100 µM glyphosate when compared to controls (bare gold and PEG FGTs) despite its design toward maximized sensitivity to charge-based signals using FGT models. In addition to considering the Debye length (0.7 nm in 1X PBS), the binding affinity of the glyphosate antibody was also considered. Attempts to measure the binding constant (K_D) of the glyphosate antibody with SPR also proved to be a challenge. In varying the antibody density, electrolyte strength, and pH of the antibody solution, a binding curve was still never achieved. As such, the glyphosate FGT biosensor was not successful in detection of glyphosate, which we attribute to the poor quality of the capture agent.

The third study attempted to address the issues with small molecule detection by changing the analyte to serotonin and utilizing a structure-shifting aptamer to overcome enhance charge-based signals near the FG2 interface. The serotonin aptamer has a K_D of 360 nM that was characterized in-house with SPR. The serotonin aptamer, having a C_6-thiol linker, was self-assembled onto gold and backfilled with 6-mercaptohexanol (MCH) in order to displace physisorbed aptamer and densify the monolayer. The surface functionalization was characterized

with XPS and CV. Serotonin FGT biosensors were designed for charge-based sensing based FGT models, and the expected sensing mechanism meant to amplify signal, as the highly negatively charged aptamer rearranges away from the surface upon serotonin capture. Serotonin FGT biosensors required sweeping over 5-20 min to stabilize the device before introducing serotonin. The serotonin FGT biosensor responded as expected to serotonin with concentration-dependent signals; however, the serotonin FGT biosensor also responded to a cocktail of other neurologically relevant small molecules, challenging the sensing mechanism. SPR selectivity data also challenged the selectivity of the serotonin aptamer due to SPR signals from dopamine, ADP, and histamine at 1 μM concentrations. Further, control FGTs having MCH, PEG thiol, hexanethiol, or glyphosate aptamer/MCH functionalization elicited concentration-dependent responses to serotonin. After interrogating an MCH FGT as usual for stabilization and serotonin sensing, the sensing surface was characterized with XPS to compare against an uninterrogated MCH surface. The findings pointed toward electrochemical losses of MCH during interrogation, and further losses after interrogating with 1 mM serotonin in the electrolyte, 1X PBS. Thus, the serotonin FGT biosensor not only suffered from stability issues, leading to electrochemical desorption of thiols, but also raised the question of whether the electrochemical activity of serotonin and other small molecule analytes could promote electrochemical desorption, causing false signals.

In the final study, the electrochemical stability of the sensing surfaces used for the serotonin and glyphosate FGT biosensors are explored using cyclic voltammetry (CV), focusing mainly on the aptamer/MCH functionalization. Functionalized gold electrodes were electrochemically interrogated as the working electrode using CV. The electrolyte was 1X PBS with and without 10 mM $K_3[Fe(CN)]_6$, a redox reporter. The working electrode potential (vs Ag/AgCl) was probed on both the negative and positive bounds up to ±0.9 V, and the sweep rate was 25 mV/s.

Aptamer/MCH electrodes exhibited thiol losses at potentials beyond the –0.5 V to +0.7 V window for 1X PBS interrogation. Faster sweep rates lead to less changes in the voltammogram per sweep. Electrodes functionalized with 11-MUA and electrodes subsequently reacted to conjugate glyphosate antibodies are less resistant to electrochemical damage in 1X PBS with 10 mM $K_3[Fe(CN)]_6$, indicating that perhaps a denser, more uniform, and/or thicker monolayer can suppress electrochemical reactions leading to surface damage. The potential window can be translated to the potential felt at FG2 when operating an FGT by flipping the polarity, roughly setting the bounds to –0.7 V to +0.5 V.

Overall, small molecule detection with an FGT proves to be a challenge, but insights discovered in this work can lead to optimization of parameters other than the FGT architecture. For one, setting experimental limits for interfacial charge sensing with quasi-static FGT inverters, considering the distance of the charge from the electrode and density of charge, can be utilized to predict the charge-based detection of small molecule-capture agent complexes. Future work must also consider how the composition of the sensing surface and quasi-static biasing impact the stability and sensitivity of FGT biosensors.

7.2 Exploring the Limits of Interfacial Charge Sensing

Despite models providing a roadmap for devising the quasi-static FGT inverter for enhanced sensitivity to charge-based and capacitance-based signals, electrolyte strength and biasing must be explored as additional design parameters. Here, we can consider a prior study on the interfacial charge sensitivity of the quasi-static FGT by Thomas et al.[44] Three different SAMs were used to determine the average change in V_T upon altering the pH of the aqueous environment, promoting protonation or deprotonation that altered the interfacial charge near the FG2 interface.

In determining the surface density, the surface potential (φ) was predicted with Grahame's equation, derived from the Guoy–Chapman treatment of an EDL,[44,137]

$$\varphi = \frac{2kT}{e} \sinh^{-1}\left(\frac{\sigma}{\sqrt{8\varepsilon\varepsilon_0 kTN_A C_{ions}}}\right) \quad (7.1)$$

where σ is the surface charge density, T is temperature, k is Boltzmann's constant, N_A is Avogadro's number, and ε_0 is the permittivity of free space. Related to the aqueous electrolyte, ε is the dielectric constant of the medium, and C_{ions} is the concentration of ions in solution. Grahame's equation was used to predict the change in φ for deprotonation of the 11-MUA SAM, providing good agreement with the experimentally determined V_T shift. Additionally, the electrolyte strength was varied for 11-MUA SAMs, where higher electrolyte strength ultimately dampened the response of ionizing the tail group. As charge-screening increases with higher electrolyte strength, this result was expected.

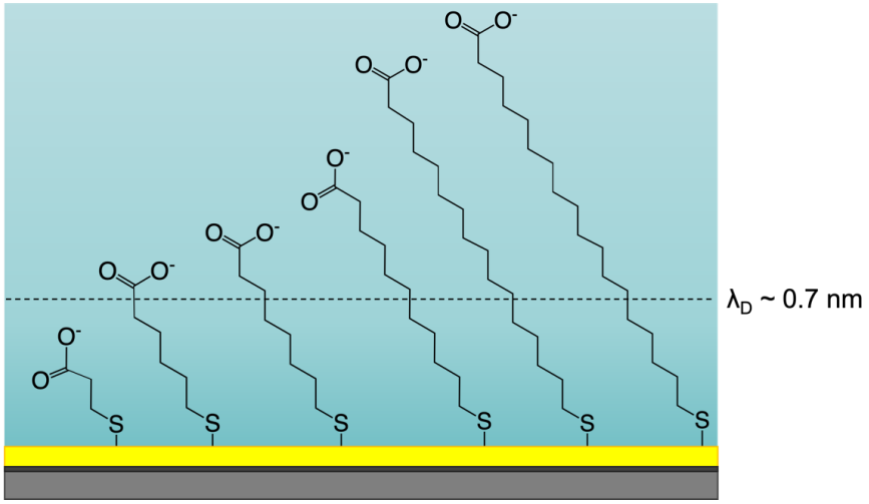

Figure 7.1. Altering the length of carboxylic acid-terminated thiols. The Debye length for 1X PBS (λ_D) is denoted as 0.7 nm.

Because an antibody is a fixed capture agent and small molecules have limited charge density, the studies used to understand interfacial charge sensing with 11-MUA can be extended

to estimate the bounds for charge-based sensing using quasi-static FGTs. A typical IgG antibody has dimensions of 14.5 nm x 8.0 nm x 4.0 nm, with the antigen binding sites located 13.6 nm apart from each other.[139] The area that an antibody occupies on the surface can be estimated as a circle with a diameter of 13.6 nm. In the case of glyphosate (2–) binding at each site, the total, average charge of 4– occupies a 191 nm^2 area. Comparatively, as the density of 11-MUA on the surface was 3.2 molecules/nm^2, and considering 4 molecules (4 COO^- groups), an average charge of 4– occupies a 1.28 nm^2 area, nearly 100-fold lower than the antibody conjugated surface. The proposed study would tune the length of the alkyl chain of a SAM, systematically altering the distance of the fixed, ionizable carboxylic acid group from the electrode interface. Carboxyl-terminated alkanethiols that are commercially available are shown in Fig, 7.1. Similarly, variables such as the electrolyte strength and density of carboxyl-terminated thiols in the monolayer (using a mixed monolayer) can be varied to realize the limits for charge-based sensing for instances of varied charge density at the surface.

For quantification of the number of ionizable groups, the surface density of thiols can be quantified. This must be done for each thiol type, as the density of the SAM may vary due to intermolecular forces. A characterization tool that accomplishes this, without the use of a redox tag, is nuclear reaction analysis (NRA), a variant of Rutherford backscattering spectrometry (RBS), available at the University of Minnesota Characterization Facility.[44,177,178] NRA detects light elements, such as carbon, using an energetic, ion beam to collide with the nuclei within the target surface. An intermediate nuclear state is formed that decays back to the original reactants, emitting a particle that can be counted and correlated to the surface coverage of carbon atoms.[178]

We expect that as the alkyl chain lengthens, Grahame's equation will no longer be able to predict the surface potential. Alternatively, we can look toward the Debye length, commonly

referred to for electrochemical biosensors, derived from the linearized Poisson-Boltzmann model, that considers a flat plane[137,179]

$$\varphi(x) = \varphi_o \exp\left(\frac{-x}{\lambda_D}\right) \text{ and } \lambda_D = \sqrt{\frac{\varepsilon\varepsilon_0 kT}{2e^2 N_A C_i}} \tag{7.2}$$

where φ_o is the potential at the interface, x is the distance away from the plane, and e is the elementary charge. The theoretical value for λ_D can be calculated for each electrolyte strength and compared to the length at which charge is no longer detectable for carboxylic-acid terminated thiols.

In considering the Debye length limitations, work on EGT biosensors have circumvented limitations by the use of high frequency potentials (>1 MHz), where the EDL does not have the time to relax to an equilibrium state that induces charge-screening at the sensing interface.[179,180] Although the capacitance of ionic liquids drop substantially beyond 100 kHz, recent work has enabled stable 1-10 MHz operation with ZnO-based EGTs by minimizing parasitic resistances and capacitances associated with the ion gel.[181] More so, inverter curves can be measured within ± 1 V, so the electrochemical breakdown from water oxidation can be avoided. As EIS has shown to decrease the perturbation of aptamer-functionalized gold electrodes compared CV,[68] the use of a high frequency potential may also improve the electrochemical stability of the sensing interface as compared to quasi-DC operation. As such, we suggest adoption of the ZnO EGT to test the use of high frequency V_G on the amplification of charge-based signals, where the limits determined by the aforementioned study utilizing quasi-static FGT inverters can be tested.

7.3 Tailoring Surface Composition for Enhanced and Stable FGT Sensing

In order to understand the sensing mechanism in Chapter 5, where serotonin interacted with functionalized FGTs with dose-dependent responses, we can look toward electrochemical and spectroscopic surface characterization. To realize if the electrochemical activity of serotonin does in fact play a role in the sensor response, CV can be used with 1 mM serotonin in solution with 1X PBS as the electrolyte. Serotonin aptamer electrodes backfilled with MCH can be used as the working electrode, and bare gold electrodes can be used to characterize peaks perhaps generated by electrochemical events between serotonin and the gold electrode. By sweeping the electrode between ±0.6 V at a sweep rate of 100 mV/s, common conditions used for FGT and EGT measurements, the voltammogram can be monitored over 20 sweeps. The emergence of a peak from the oxygen reduction reaction (ORR) can serve as an indication of thiol desorption from the surface. Electrodes can subsequently be characterized with XPS to observe changes in the C_{1s}, S_{2p}, and N_{1s} high-resolution spectra for evidence of thiol desorption, reduction, and/or oxidation. In the case that serotonin does promote thiol desorption from the surface, experiments can be extended toward other electroactive small molecules, such as dopamine, in order to observe whether this is a general issue for FGT-based (and other transistor-based) detection.

To enable stable sensing with a quasi-static FGT inverter using structure-shifting aptamers, we can look toward designing a sensing interface that is electrochemically stable within the FGT operating potentials. In looking toward other avenues for signal amplification and stability, we find the SAM composing the sensing surface plays a critical role in the sensitivity of both capacitance- and charge-based perturbations generating signals for electrochemical biosensors. For example, Macchia et al. attribute the use of a mixed monolayer of 11-MUA and 3-MPA to the first demonstration of single-molecule detection with a transistor-based biosensor.[182–185] In this

work, it is suggested that capture of a single IgG antibody invokes a slight change in the tilt of the underlying SAM, causing a work function shift that is associated with a shift in the transfer curve. Other strategies utilize mixed monolayers of PEG thiols, enabling detection beyond the Debye length in high electrolyte strength buffers.[86,87,120,179] Recent analytical models propose that a Donnan potential is formed from ions immobilizing in the functionalized surface layer. [87] These analytical models built around the Donnan theory suggest that the length of the PEG thiol must match or be longer than the distance of the target analyte-capture agent complex from the interface in order to detect the charge of the target analyte. A third example finds that altering the terminal functional group of a backfilling SAM from an alcohol to a methoxy group can have a significant impact on the long-term stability of an EAB sensor.[70] All of these examples highlight how crucial the design of the sensing surface beyond the sensitivity and specificity of the capture agent.

As was shown in Chapter 6, the electrochemical stability of individual thiols forming a SAM are unique, and mixed monolayers take on the characteristics of each thiol. With this, the electrochemical stability under quasi-static interrogation of the aptamer-functionalized surface can perhaps be widened to larger potentials windows by surveying various candidates for backfilling, including hexanethiol, PEG thiol, and 1-dodecanethiol to name a few. Studies done in Chapter 6 can be replicated for aptamer-functionalized electrodes surveying a library of backfilling thiols in order to enhance the electrochemical stability of the serotonin aptamer. One previously mentioned means of determining the stability within the FGT biosensor is by monitoring the floating gate potential (V_{FG}) as V_G is swept. As the surface undergoes deconstruction, we anticipate V_{FG} will change, as observed with the inverter curves over the stabilization period for serotonin FGT biosensors. To gain insight into the mechanisms causing instability, XPS and AFM can be used as

tools to measure the surface chemical composition, surface roughness, and electrode thickness after interrogation of FG2.

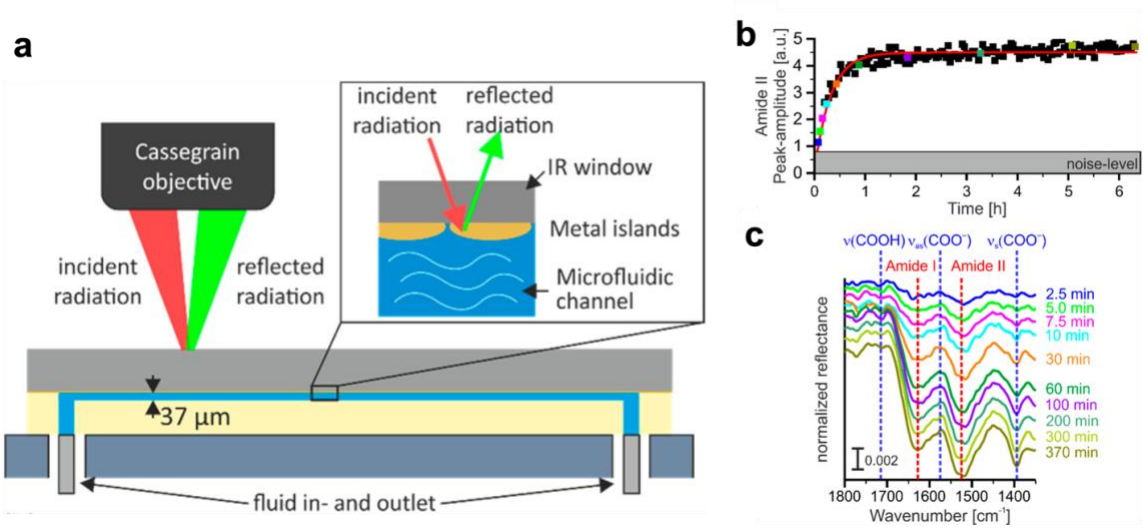

Figure 7.2. In situ infrared spectroscopy under microfluidic flow. (a) A microfluidic cell where incident radiation permeates an IR transparent silicon substrate, interacting with the metal islands. Radiation is reflected, reaching the detector to collect the spectrum. (b) The amide II band peak amplitude as a function of time. (c) Changes in the IR spectra as GSH was flown over the metal interface, conjugating to the surface. Reprinted (adapted) with permission from Kratz, C.; Furchner, A.; Oates, T. W. H.; Janasek, D.; Hinrichs, K. Nanoliter Sensing for Infrared Bioanalytics. *ACS Sens* **2018**, *3* (2), 299–303. Copyright 2021 American Chemical Society.

Aside from using the previously mentioned forms of characterization, we can look toward forms of in situ characterization that can be adapted to resemble the FGT sensing medium. Infrared spectroscopy has been used to monitor the surface as it undergoes transformations or as it is used for its reactivity, such as in the case of monitoring surface functionalization, biomolecular interactions, or catalytic activity in mL flow cells or with microfluidics.[186] An example of a microfluidic cell for in situ monitoring of tripeptide glutathione (GSH) immobilization on gold is shown in Fig 7.2, where an IR spectrum was collected every 2.5 min.[187] The cell utilizes gold metal islands in order to enhance the signal by 10-100 fold over the full mid-IR range.

For electrochemical work, a chip can be designed similarly but with the inclusion of a side gate for voltage application in order to mimic the FGT sensing environment. Electrochemical cells for in situ IR have been designed before to monitor the growth of polypyrrole[189] films at the liquid/solid interface of silicon, but the silicon substrate was the working electrode rather than having a side-gated potential. The optofluidic platform in Fig 7.2 does not necessitate the use of additional optics (e.g., prisms), is not limited by water's strong absorption decreasing the length of the light path, and can be equipped with commercially available microfluidic chip materials.[187] The integration of the microfluidic chamber can flush desorbed thiol from the surface while also enabling introduction of small molecule analytes, such as serotonin, to observe how electrochemical interrogation influences the surface. Vibrational bands characteristic to bonds can be characterized ex situ, as done in Section 4.3, without and after electrochemical interrogation with CV. In situ spectra can be collected in a similar fashion to Fig 7.2; however, the gate voltage can be swept in between spectrum collection. Control spectra can be collected for the chip under flow but without electrochemical interrogation in order to determine the noise level of the system. This platform can also be extended to characterize the surface under microfluidic flow for future surface chemistries, especially to examine whether reaction times can be minimized under microfluidic flow compared to immersion chemistries used with a PDMS well.

Bibliography

(1) Qureshi, A.; Gurbuz, Y.; Niazi, J. H. Biosensors for Cardiac Biomarkers Detection: A Review. *Sens Actuators B Chem* **2012**, *171–172*, 62–76. https://doi.org/10.1016/j.snb.2012.05.077.

(2) Masson, J. F. Surface Plasmon Resonance Clinical Biosensors for Medical Diagnostics. *ACS Sens* **2017**, *2* (1), 16–30. https://doi.org/10.1021/acssensors.6b00763.

(3) Yang, T.; Huang, H.; Zhu, F.; Lin, Q.; Zhang, L.; Liu, J. Recent Progresses in Nanobiosensing for Food Safety Analysis. *Sensors (Switzerland)* **2016**, *16* (7), 1–19. https://doi.org/10.3390/s16071118.

(4) Ge, L.; Liu, Q.; Hao, N.; Wang, Kun. Recent Developments of Photoelectrochemical Biosensors for Food Analysis. *J Mater Chem B* **2019**, *7*, 7283–7300. https://doi.org/10.1039/c9tb01644a.

(5) Justino, C. I. L.; Duarte, A. C.; Rocha-Santos, T. A. P. Recent Progress in Biosensors for Environmental Monitoring: A Review. *Sensors (Switzerland)* **2017**, *17* (12). https://doi.org/10.3390/s17122918.

(6) Domon, B.; Aebersold, R. Mass Spectrometry and Protein Analysis. *Science (1979)* **2006**, *312* (5771), 212–217. https://doi.org/10.1126/science.1124619.

(7) Pan, S.; Aebersold, R.; Chen, R.; Rush, J.; Goodlett, D. R.; McIntosh, M. W.; Zhang, J.; Brentnall, T. A. Mass Spectrometry Based Targeted Protein Quantification: Methods and Applications. *J Proteome Res* **2009**, *8* (2), 787–797. https://doi.org/10.1021/pr800538n.

(8) Kellie, J. F.; Tran, J. C.; Lee, J. E.; Ahlf, D. R.; Thomas, H. M.; Ntai, I.; Catherman, A. D.; Durbin, K. R.; Zamdborg, L.; Vellaichamy, A.; Thomas, M.; Kelleher, N. L. The Emerging Process of Top Down Mass Spectrometry for Protein Analysis: Biomarkers, Protein-Therapeutics, and Achieving High Throughput. *Mol Biosyst.* **2011**, *6* (9), 1532–1539. https://doi.org/10.1039/c000896f.The.

(9) Dahal, U. P.; Jones, J. P.; Davis, J. A.; Rock, D. A. Small Molecule Quantification by Liquid Chromatography-Mass Spectrometry for Metabolites of Drugs and Drug Candidates. *Drug Metabolism and Disposition* **2011**, *39* (12), 2355–2360. https://doi.org/10.1124/dmd.111.040865.

(10) Hayrapetyan, H.; Tran, T.; Tellez-Corrales, E.; Madiraju, C. Enzyme-Linked Immunosorbent Assay: Types and Applications. In *Methods in Molecular Biology*; 2015; Vol. 2612, pp 1–18.

(11) Alvarez-Puebla, R. A.; Liz-Marzán, L. M. SERS-Based Diagnosis and Biodetection. *Small* **2010**, *6* (5), 604–610. https://doi.org/10.1002/smll.200901820.

(12) Wang, X.; Choi, N.; Cheng, Z.; Ko, J.; Chen, L.; Choo, J. Simultaneous Detection of Dual Nucleic Acids Using a SERS-Based Lateral Flow Assay Biosensor. *Anal Chem* **2017**, *89* (2), 1163–1169. https://doi.org/10.1021/acs.analchem.6b03536.

(13) Nguyen, H. H.; Park, J.; Kang, S.; Kim, M. Surface Plasmon Resonance: A Versatile Technique for Biosensor Applications. *Sensors (Switzerland)* **2015**, *15* (5), 10481–10510. https://doi.org/10.3390/s150510481.

(14) Liu, X.; Guo, J.; Li, Y.; Wang, B.; Yang, S.; Chen, W.; Wu, X.; Guo, J.; Ma, X. SERS Substrate Fabrication for Biochemical Sensing: Towards Point-of-Care Diagnostics. *J Mater Chem B* **2021**, *9* (40), 8378–8388. https://doi.org/10.1039/d1tb01299a.

(15) Zeni, L.; Perri, C.; Cennamo, N.; Arcadio, F.; D'Agostino, G.; Salmona, M.; Beeg, M.; Gobbi, M. A Portable Optical-Fibre-Based Surface Plasmon Resonance Biosensor for the Detection of Therapeutic Antibodies in Human Serum. *Sci Rep* **2020**, *10* (1). https://doi.org/10.1038/s41598-020-68050-x.

(16) Bergveld, P. Short Communications: Development of an Ion-Sensitive Solid-State Device for Neurophysiological Measurements. *IEEE Trans Biomed Eng* **1970**, *BME-17* (1), 70–71. https://doi.org/10.1109/TBME.1970.4502688.

(17) Caras, S.; Janata, J. Field Effect Transistor Sensitive to Penicillin. *Anal Chem* **1980**, *52* (12), 1935–1937. https://doi.org/10.1021/ac50062a035.

(18) Torricelli, F.; Adrahtas, D. Z.; Bao, Z.; Berggren, M.; Biscarini, F.; Bonfiglio, A.; Bortolotti, C. A.; Frisbie, C. D. Electrolyte-Gated Transistors for Enhanced Performance Bioelectronics. *Nature Reviews Methods Primers* **2021**, *1* (66). https://doi.org/10.1038/s43586-021-00065-8.

(19) Kim, S. H.; Hong, K.; Xie, W.; Lee, K. H.; Zhang, S.; Lodge, T. P.; Frisbie, C. D. Electrolyte-Gated Transistors for Organic and Printed Electronics. *Advanced Materials* **2013**, *25* (13), 1822–1846. https://doi.org/10.1002/adma.201202790.

(20) Khademi, M.; Barz, D. P. J. Structure of the Electrical Double Layer Revisited: Electrode Capacitance in Aqueous Solutions. *Langmuir* **2020**, *36* (16), 4250–4260. https://doi.org/10.1021/acs.langmuir.0c00024.

(21) Thomas, M. S.; Adrahtas, D. Z.; Frisbie, C. D.; Dorfman, K. D. Modeling of Quasi-Static Floating-Gate Transistor Biosensors. *ACS Sens* **2021**, *6* (5), 1910–1917. https://doi.org/10.1021/ACSSENSORS.1C00261.

(22) Newman, C. R.; Frisbie, C. D.; Da Silva Filho, D. A.; Brédas, J. L.; Ewbank, P. C.; Mann, K. R. Introduction to Organic Thin Film Transistors and Design of N-Channel Organic Semiconductors. *Chemistry of Materials*. November 16, 2004, pp 4436–4451. https://doi.org/10.1021/cm049391x.

(23) Rivnay, J.; Inal, S.; Salleo, A.; Owens, R. M.; Berggren, M.; Malliaras, G. G. Organic Electrochemical Transistors. *Nat Rev Mater* **2018**, *3* (17086). https://doi.org/10.1038/natrevmats.2017.86.

(24) Khodagholy, D.; Rivnay, J.; Sessolo, M.; Gurfinkel, M.; Leleux, P.; Jimison, L. H.; Stavrinidou, E.; Herve, T.; Sanaur, S.; Owens, R. M.; Malliaras, G. G. High Transconductance Organic Electrochemical Transistors. *Nat Commun* **2013**, *4* (1), 2133. https://doi.org/10.1038/ncomms3133.

(25) Leleux, P.; Rivnay, J.; Lonjaret, T.; Badier, J.-M.; Bénar, C.; Hervé, T.; Chauvel, P.; Malliaras, G. G. Organic Electrochemical Transistors for Clinical Applications. *Adv Healthc Mater* **2015**, *4* (1), 142–147. https://doi.org/https://doi.org/10.1002/adhm.201400356.

(26) Bergveld, P. Development of an Ion-Sensitive Solid-State Device for Neurophysiological Measurements. *IEEE Trans Biomed Eng* **1970**, *BME-17* (1), 70–71. https://doi.org/10.1109/TBME.1970.4502688.

(27) White, S. P.; Frisbie, C. D.; Dorfman, K. D. Detection and Sourcing of Gluten in Grain with Multiple Floating-Gate Transistor Biosensors. *ACS Sens* **2018**, *3* (2), 395–402. https://doi.org/10.1021/acssensors.7b00810.

(28) White, S. P.; Sreevatsan, S.; Frisbie, C. D.; Dorfman, K. D. Rapid, Selective, Label-Free Aptameric Capture and Detection of Ricin in Potable Liquids Using a Printed Floating Gate Transistor. *ACS Sens* **2016**, *1* (10), 1213–1216. https://doi.org/10.1021/acssensors.6b00481.

(29) Spyropoulos, G. D.; Gelinas, J. N.; Khodagholy, D. Internal Ion-Gated Organic Electrochemical Transistor: A Building Block for Integrated Bioelectronics. *Sci Adv* **2020**, *5* (2). https://doi.org/10.1126/SCIADV.AAU7378.

(30) Cea, C.; Spyropoulos, G. D.; Jastrzebska-Perfect, P.; Ferrero, J. J.; Gelinas, J. N.; Khodagholy, D. Enhancement-Mode Ion-Based Transistor as a Comprehensive Interface and Real-Time Processing Unit for in Vivo Electrophysiology. *Nat Mater* **2020**, *19* (6), 679–686. https://doi.org/10.1038/s41563-020-0638-3.

(31) Cho, J. H.; Lee, J.; Xia, Y.; Kim, B.; He, Y.; Renn, M. J.; Lodge, T. P.; Daniel Frisbie, C. Printable Ion-Gel Gate Dielectrics for Low-Voltage Polymer Thin-Film Transistors on Plastic. *Nat Mater* **2008**, *7* (11), 900–906. https://doi.org/10.1038/nmat2291.

(32) Hong, K.; Kim, Y. H.; Kim, S. H.; Xie, W.; Xu, W. D.; Kim, C. H.; Frisbie, C. D. Aerosol Jet Printed, Sub-2 v Complementary Circuits Constructed from P-and N-Type Electrolyte Gated Transistors. *Advanced Materials* **2014**, *26* (41), 7032–7037. https://doi.org/10.1002/adma.201401330.

(33) Kim, S. H.; Hong, K.; Lee, K. H.; Frisbie, C. D. Performance and Stability of Aerosol-Jet-Printed Electrolyte-Gated Transistors Based on Poly(3-Hexylthiophene). *ACS Appl Mater Interfaces* **2013**, *5* (14), 6580–6585. https://doi.org/10.1021/am401200y.

(34) Schmoltner, K.; Kofler, J.; Klug, A.; List-Kratochvil, E. J. W. Electrolyte-Gated Organic Field-Effect Transistor for Selective Reversible Ion Detection. *Advanced Materials* **2013**, *25* (47), 6895–6899. https://doi.org/10.1002/adma.201303281.

(35) Ferro, M. P.; Leclerc, L.; Sleiman, M.; Marchiori, B.; Pourchez, J.; Owens, R. M.; Ramuz, M. Effect of E Cigarette Emissions on Tracheal Cells Monitored at the Air–Liquid Interface Using an Organic Electrochemical Transistor. *Adv Biosyst* **2019**, *3* (3), 1800249. https://doi.org/https://doi.org/10.1002/adbi.201800249.

(36) Jimison, L. H.; Tria, S. A.; Khodagholy, D.; Gurfinkel, M.; Lanzarini, E.; Hama, A.; Malliaras, G. G.; Owens, R. M. Measurement of Barrier Tissue Integrity with an Organic

Electrochemical Transistor. *Advanced Materials* **2012**, *24* (44), 5919–5923. https://doi.org/https://doi.org/10.1002/adma.201202612.

(37) van der Spiegel, J.; Lauks, I.; Chan, P.; Babic, D. The Extended Gate Chemically Sensitive Field Effect Transistor as Multi-Species Microprobe. *Sensors and Actuators* **1983**, *4*, 291–298.

(38) Spanu, A.; Lai, S.; Cosseddu, P.; Tedesco, M.; Martinoia, S.; Bonfiglio, A. An Organic Transistor-Based System for Reference-Less Electrophysiological Monitoring of Excitable Cells. *Sci Rep* **2015**, *5*, 1–7. https://doi.org/10.1038/srep08807.

(39) Spanu, A.; Tedesco, M. T.; Martines, L.; Martinoia, S.; Bonfiglio, A. An Organic Neurophysiological Tool for Neuronal Metabolic Activity Monitoring. *APL Bioeng* **2018**, *2* (4). https://doi.org/10.1063/1.5050170.

(40) Spanu, A.; Viola, F.; Lai, S.; Cosseddu, P.; Ricci, P. C.; Bonfiglio, A. A Reference-Less PH Sensor Based on an Organic Field Effect Transistor with Tunable Sensitivity. *Org Electron* **2017**, *48*, 188–193. https://doi.org/10.1016/j.orgel.2017.06.010.

(41) White, S. P.; Dorfman, K. D.; Frisbie, C. D. Operating and Sensing Mechanism of Electrolyte-Gated Transistors with Floating Gates: Building a Platform for Amplified Biodetection. *Journal of Physical Chemistry C* **2016**, *120* (1), 108–117. https://doi.org/10.1021/acs.jpcc.5b10694.

(42) White, S. P.; Dorfman, K. D.; Frisbie, C. D. Label-Free DNA Sensing Platform with Low-Voltage Electrolyte-Gated Transistors. *Anal Chem* **2015**, *87* (3), 1861–1866. https://doi.org/10.1021/ac503914x.

(43) Wink, T.; Van Zuilen, S. J.; Bult, A.; Van Bennekom, W. P. Self-Assembled Monolayers for Biosensors. *Analyst* **1997**, *122* (4), 43–50. https://doi.org/10.1039/a606964i.

(44) Thomas, M. S.; White, S. P.; Dorfman, K. D.; Frisbie, C. D. Interfacial Charge Contributions to Chemical Sensing by Electrolyte-Gated Transistors with Floating Gates. *Journal of Physical Chemistry Letters* **2018**, *9* (6), 1335–1339. https://doi.org/10.1021/acs.jpclett.8b00285.

(45) Thomas, M. S.; Dorfman, K. D.; Frisbie, C. D. Detection and Amplification of Capacitance- and Charge-Based Signals Using Printed Electrolyte Gated Transistors with Floating Gates. *Flexi. Print. Electron.* **2019**, *4*, 044001.

(46) Fan, C.; Plaxco, K. W.; Heeger, A. J. Electrochemical Interrogation of Conformational Changes as a Reagentless Method for the Sequence-Specific Detection of DNA. *Proc Natl Acad Sci U S A* **2003**, *100* (16), 9134–9137. https://doi.org/10.1073/pnas.1633515100.

(47) Ferguson, B. S.; Hoggarth, D. A.; Maliniak, D.; Ploense, K.; White, R. J.; Woodward, N.; Hsieh, K.; Bonham, A. J.; Eisenstein, M.; Kippin, T. E.; Plaxco, K. W.; Soh, H. T. Real-Time, Aptamer-Based Tracking of Circulating Therapeutic Agents in Living Animals. *Sci Transl Med* **2013**, *5* (213). https://doi.org/10.1126/scitranslmed.3007095.

(48) Li, H.; Dauphin-Ducharme, P.; Ortega, G.; Plaxco, K. W. Calibration-Free Electrochemical Biosensors Supporting Accurate Molecular Measurements Directly in Undiluted Whole

Blood. *J Am Chem Soc* **2017**, *139* (32), 11207–11213. https://doi.org/10.1021/jacs.7b05412.

(49) Li, H.; Arroyo-Currás, N.; Kang, D.; Ricci, F.; Plaxco, K. W. Dual-Reporter Drift Correction To Enhance the Performance of Electrochemical Aptamer-Based Sensors in Whole Blood. *J Am Chem Soc* **2016**, *138* (49), 15809–15812. https://doi.org/10.1021/jacs.6b08671.

(50) Arroyo-Currás, N.; Somerson, J.; Vieira, P. A.; Ploense, K. L.; Kippin, T. E.; Plaxco, K. W. Real-Time Measurement of Small Molecules Directly in Awake, Ambulatory Animals. *Proc Natl Acad Sci U S A* **2017**, *114* (4), 645–650. https://doi.org/10.1073/pnas.1613458114.

(51) Santos-Cancel, M.; Simpson, L. W.; Leach, J. B.; White, R. J. Direct, Real-Time Detection of Adenosine Triphosphate Release from Astrocytes in Three-Dimensional Culture Using an Integrated Electrochemical Aptamer-Based Sensor. *ACS Chem Neurosci* **2019**, *10* (4), 2070–2079. https://doi.org/10.1021/acschemneuro.9b00033.

(52) Stoltenburg, R.; Reinemann, C.; Strehlitz, B. SELEX-A (r)Evolutionary Method to Generate High-Affinity Nucleic Acid Ligands. *Biomolecular Engineering*. October 2007, pp 381–403. https://doi.org/10.1016/j.bioeng.2007.06.001.

(53) Morales, M. A.; Halpern, J. M. Guide to Selecting a Biorecognition Element for Biosensors. *Bioconjug Chem* **2018**, *29* (10), 3231–3239. https://doi.org/10.1021/acs.bioconjchem.8b00592.

(54) Feagin, T. A.; Maganzini, N.; Soh, H. T. Strategies for Creating Structure-Switching Aptamers. *ACS Sens* **2018**, *3* (9), 1611–1615. https://doi.org/10.1021/acssensors.8b00516.

(55) Yoshikawa, A. M.; Rangel, A. E.; Zheng, L.; Wan, L.; Hein, L. A.; Hariri, A. A.; Eisenstein, M.; Soh, H. T. A Massively Parallel Screening Platform for Converting Aptamers into Molecular Switches. *Nat Commun* **2023**, *14* (1). https://doi.org/10.1038/s41467-023-38105-4.

(56) Shepherd, J. L.; Kell, A.; Chung, E.; Sinclar, C. W.; Workentin, M. S.; Bizzotto, D. Selective Reductive Desorption of a SAM-Coated Gold Electrode Revealed Using Fluorescence Microscopy. *J Am Chem Soc* **2004**, *126* (26), 8329–8335. https://doi.org/10.1021/ja0494095.

(57) Walczak, M. M.; Popenoe, D. D.; Deinhammer, R. S.; Lamp, B. D.; Chung, C.; Porter, M. D. Reductive Desorption of Alkanethiolate Monolayers at Gold: A Measure of Surface Coverage. *Langmuir* **1991**, *7* (11), 2687–2693.

(58) Tencer, M.; Nie, H. Y.; Berini, P. Formation and Electrochemical Desorption of Self-Assembled Monolayers as Studied by ToF-SIMS. *Surface and Interface Analysis* **2011**, *43* (6), 993–997. https://doi.org/10.1002/sia.3682.

(59) Schneider, T. W.; Buttry, D. A. Electrochemical Quartz Crystal Microbalance Studies of Adsorption and Desorption of Self-Assembled Monolayers of Alkyl Thiols on Gold. *J. Am. Chem. Soc* **1993**, *115* (26), 12391–12397.

(60) Tencer, M.; Berini, P. Toposelective Electrochemical Desorption of Thiol SAMs from Neighboring Polycrystalline Gold Surfaces. *Langmuir* **2008**, *24* (21), 12097–12101. https://doi.org/10.1021/la801443y.

(61) Vinokurov, I. A.; Morin, M.; Kankare, J. Mechanism of Reductive Desorption of Self-Assembled Monolayers on the Basis of Avrami Theorem and Diffusion. *Journal of Physical Chemistry B* **2000**, *104* (24), 5790–5796. https://doi.org/10.1021/jp0002502.

(62) Tencer, M.; Krupin, O.; Tezel, B.; Berini, P. Electrochemistry of Au-SAM-Protein Stacks. *J Electrochem Soc* **2013**, *160* (1), H22–H27. https://doi.org/10.1149/2.034301jes.

(63) Widrig, C. A.; Chung, C.; Porter, M. D. The Electrochemical Desorption of N-Alkanethiol Monolayers from Polycrystalline Au and Ag Electrodes. *J. Electroanal. Chem* **1991**, *310*, 335–359.

(64) Sheridan, A. K.; Ngamukot, P.; Bartlett, P. N.; Wilkinson, J. S. Waveguide Surface Plasmon Resonance Sensing: Electrochemical Desorption of Alkane Thiol Monolayers. *Sens Actuators B Chem* **2006**, *117* (1), 253–260. https://doi.org/10.1016/j.snb.2005.11.047.

(65) Jacob, J. D. C.; Lee, T. R.; Baldelli, S. In Situ Vibrational Study of the Reductive Desorption of Alkanethiol Monolayers on Gold by Sum Frequency Generation Spectroscopy. *Journal of Physical Chemistry C* **2014**, *118* (50), 29126–29134. https://doi.org/10.1021/jp504463z.

(66) Kang, D.; Ricci, F.; White, R. J.; Plaxco, K. W. Survey of Redox-Active Moieties for Application in Multiplexed Electrochemical Biosensors. *Anal Chem* **2016**, *88* (21), 10452–10458. https://doi.org/10.1021/acs.analchem.6b02376.

(67) Watkins, Z.; Karajic, A.; Young, T.; White, R.; Heikenfeld, J. Week-Long Operation of Electrochemical Aptamer Sensors: New Insights into Self-Assembled Monolayer Degradation Mechanisms and Solutions for Stability in Serum at Body Temperature. *ACS Sens* **2023**, *8* (3), 1119–1131. https://doi.org/10.1021/acssensors.2c02403.

(68) Vogiazi, V.; De La Cruz, A.; Heineman, W. R.; White, R. J.; Dionysiou, D. D. Effects of Experimental Conditions on the Signaling Fidelity of Impedance-Based Nucleic Acid Sensors. *Anal Chem* **2021**, *93* (2), 812–819. https://doi.org/10.1021/acs.analchem.0c03269.

(69) Leung, K. K.; Downs, A. M.; Ortega, G.; Kurnik, M.; Plaxco, K. W. Elucidating the Mechanisms Underlying the Signal Drift of Electrochemical Aptamer-Based Sensors in Whole Blood. *ACS Sens* **2021**, *6* (9), 3340–3347. https://doi.org/10.1021/acssensors.1c01183.

(70) Shaver, A.; Curtis, S. D.; Arroyo-Currás, N. Alkanethiol Monolayer End Groups Affect the Long-Term Operational Stability and Signaling of Electrochemical, Aptamer-Based Sensors in Biological Fluids. *ACS Appl Mater Interfaces* **2020**, *12* (9), 11214–11223. https://doi.org/10.1021/acsami.9b22385.

(71) Bidinger, S. L.; Keene, S. T.; Han, S.; Plaxco, K. W.; Malliaras, G. G.; Hasan, T. Pulsed Transistor Operation Enables Miniaturization of Electrochemical Aptamer-Based Sensors. *Sci. Adv* **2022**, *8* (46).

(72) Nakatsuka, N.; Yang, K.-A.; Abendroth, J. M.; Cheung, K. M.; Xu, X.; Yang, H.; Zhao, C.; Zhu, B.; Rim, Y. S.; Yang, Y.; Weiss, P. S.; Stojanović, M. N.; Andrews, A. M. Aptamer–Field-Effect Transistors Overcome Debye Length Limitations for Small-Molecule Sensing. *Science (1979)* **2018**, *362* (6412), 319–324. https://doi.org/10.1126/science.aao6750.

(73) Annett, R.; Habibi, H. R.; Hontela, A. Impact of Glyphosate and Glyphosate-Based Herbicides on the Freshwater Environment. *Journal of Applied Toxicology* **2014**, *34* (5), 458–479. https://doi.org/10.1002/jat.2997.

(74) Van Bruggen, A. H. C.; He, M. M.; Shin, K.; Mai, V.; Jeong, K. C.; Finckh, M. R.; Morris, J. G. Environmental and Health Effects of the Herbicide Glyphosate. *Science of the Total Environment* **2018**, *616–617*, 255–268. https://doi.org/10.1016/j.scitotenv.2017.10.309.

(75) vom Saal, F. S.; Hughes, C. An Extensive New Literature Concerning Low-Dose Effects of Bisphenol A Shows the Need for a New Risk Assessment. *Environ Health Perspect* **2005**, *113* (8), 926–933. https://doi.org/10.1289/ehp.7713.

(76) Almeida, S.; Raposo, A.; Almeida-González, M.; Carrascosa, C. Bisphenol A: Food Exposure and Impact on Human Health. *Compr Rev Food Sci Food Saf* **2018**, *17* (6), 1503–1517. https://doi.org/10.1111/1541-4337.12388.

(77) Fenton, S. E.; Ducatman, A.; Boobis, A.; DeWitt, J. C.; Lau, C.; Ng, C.; Smith, J. S.; Roberts, S. M. Per- and Polyfluoroalkyl Substance Toxicity and Human Health Review: Current State of Knowledge and Strategies for Informing Future Research. *Environ Toxicol Chem* **2021**, *40* (3), 606–630. https://doi.org/10.1002/etc.4890.

(78) Sunderland, E. M.; Hu, X. C.; Dassuncao, C.; Tokranov, A. K.; Wagner, C. C.; Allen, J. G. A Review of the Pathways of Human Exposure to Poly- and Perfluoroalkyl Substances (PFASs) and Present Understanding of Health Effects. *J Expo Sci Environ Epidemiol* **2019**, *29* (2), 131–147. https://doi.org/10.1038/s41370-018-0094-1.

(79) Valle, A. L.; Mello, F. C. C.; Alves-Balvedi, R. P.; Rodrigues, L. P.; Goulart, L. R. Glyphosate Detection: Methods, Needs and Challenges. *Environ Chem Lett* **2019**, *17* (1), 291–317. https://doi.org/10.1007/s10311-018-0789-5.

(80) Menger, R. F.; Funk, E.; Henry, C. S.; Borch, T. Sensors for Detecting Per- and Polyfluoroalkyl Substances (PFAS): A Critical Review of Development Challenges, Current Sensors, and Commercialization Obstacles. *Chemical Engineering Journal* **2021**, *417* (129133). https://doi.org/10.1016/j.cej.2021.129133.

(81) Sofen, L. E.; Furst, A. L. Perspective — Electrochemical Sensors to Monitor Endocrine Disrupting Pollutants. *J Electrochem Soc* **2020**, *167* (037524). https://doi.org/10.1149/2.0242003JES.

(82) Piccinini, E.; Alberti, S.; Longo, G. S.; Berninger, T.; Breu, J.; Dostalek, J.; Azzaroni, O.; Knoll, W. Pushing the Boundaries of Interfacial Sensitivity in Graphene FET Sensors: Polyelectrolyte Multilayers Strongly Increase the Debye Screening Length. *Journal of Physical Chemistry C* **2018**, *122* (18), 10181–10188. https://doi.org/10.1021/acs.jpcc.7b11128.

(83) Jang, H. J.; Lee, T.; Song, J.; Russell, L.; Li, H.; Dailey, J.; Searson, P. C.; Katz, H. E. Electronic Cortisol Detection Using an Antibody-Embedded Polymer Coupled to a Field-Effect Transistor. *ACS Appl Mater Interfaces* **2018**, *10* (19), 16233–16237. https://doi.org/10.1021/acsami.7b18855.

(84) Sabaté del Río, J.; Henry, O. Y. F.; Jolly, P.; Ingber, D. E. An Antifouling Coating That Enables Affinity-Based Electrochemical Biosensing in Complex Biological Fluids. *Nat Nanotechnol* **2019**, *14*, 1143–1149. https://doi.org/10.1038/s41565-019-0566-z.

(85) Zhang, J.; Lao, R.; Song, S.; Yan, Z.; Fan, C. Design of an Oligonucleotide-Incorporated Nonfouling Surface and Its Application in Electrochemical DNA Sensors for Highly Sensitive and Sequence-Specific Detection of Target DNA. *Anal Chem* **2008**, *80* (23), 9029–9033. https://doi.org/10.1021/ac801424y.

(86) Gao, N.; Zhou, W.; Jiang, X.; Hong, G.; Fu, T. M.; Lieber, C. M. General Strategy for Biodetection in High Ionic Strength Solutions Using Transistor-Based Nanoelectronic Sensors. *Nano Lett* **2015**, *15* (3), 2143–2148. https://doi.org/10.1021/acs.nanolett.5b00133.

(87) Haustein, N.; Gutiérrez-Sanz, Ó.; Tarasov, A. Analytical Model to Describe the Effect of Polyethylene Glycol on Ionic Screening of Analyte Charges in Transistor-Based Immunosensing. *ACS Sens* **2019**, *4* (4), 874–882. https://doi.org/10.1021/acssensors.8b01515.

(88) Kulkarni, G. S.; Zhong, Z. Detection beyond the Debye Screening Length in a High-Frequency Nanoelectronic Biosensor. *Nano Lett* **2012**, *12* (2), 719–723. https://doi.org/10.1021/nl203666a.

(89) Zhang, S.; Xia, J.; Li, X. Electrochemical Biosensor for Detection of Adenosine Based on Structure-Switching Aptamer and Amplification with Reporter Probe DNA Modified Au Nanoparticles. *Anal Chem* **2008**, *80* (22), 8382–8388. https://doi.org/10.1021/ac800857p.

(90) Nishitani, S.; Sakata, T. Potentiometric Adsorption Isotherm Analysis of a Molecularly Imprinted Polymer Interface for Small-Biomolecule Recognition. *ACS Omega* **2018**, *3* (5), 5382–5389. https://doi.org/10.1021/acsomega.8b00627.

(91) Sakata, T.; Nishitani, S.; Kajisa, T. Molecularly Imprinted Polymer-Based Bioelectrical Interfaces with Intrinsic Molecular Charges. *RSC Adv* **2020**, *10* (29), 16999–17013. https://doi.org/10.1039/d0ra02793f.

(92) Parlak, O.; Keene, S. T.; Marais, A.; Curto, V. F.; Salleo, A. Molecularly Selective Nanoporous Membrane-Based Wearable Organic Electrochemical Device for Noninvasive Cortisol Sensing. *Sci Adv* **2018**, *4* (7). https://doi.org/10.1126/sciadv.aar2904.

(93) Tang, K.; Turner, C.; Case, L.; Mehrehjedy, A.; He, X.; Miao, W.; Guo, S. Organic Electrochemical Transistor with Molecularly Imprinted Polymer-Modified Gate for the Real-Time Selective Detection of Dopamine. *ACS Appl Polym Mater* **2022**, *4* (4), 2337–2345. https://doi.org/10.1021/acsapm.1c01563.

(94) Bottari, F.; Daems, E.; De Vries, A. M.; Van Wielendaele, P.; Trashin, S.; Blust, R.; Sobott, F.; Madder, A.; Martins, J. C.; De Wael, K. Do Aptamers Always Bind? The Need for a

Multifaceted Analytical Approach When Demonstrating Binding Affinity between Aptamer and Low Molecular Weight Compounds. *J Am Chem Soc* **2020**, *142* (46), 19622–19630. https://doi.org/10.1021/jacs.0c08691.

(95) Tang, B.; White, S. P.; Frisbie, C. D.; Lodge, T. P. Synergistic Increase in Ionic Conductivity and Modulus of Triblock Copolymer Ion Gels. *Macromolecules* **2015**, *48* (14), 4942–4950. https://doi.org/10.1021/acs.macromol.5b00882.

(96) Kaindl, R.; Gupta, T.; Blümel, A.; Pei, S.; Hou, P. X.; Du, J.; Liu, C.; Patter, P.; Popovic, K.; Dergez, D.; Elibol, K.; Schafler, E.; Liu, J.; Eder, D.; Kieslinger, D.; Ren, W.; Hartmann, P.; Waldhauser, W.; Bayer, B. C. Aerosol Jet Printing of Graphene and Carbon Nanotube Patterns on Realistically Rugged Substrates. *ACS Omega* **2021**, *6* (50), 34301–34313. https://doi.org/10.1021/acsomega.1c03871.

(97) Tarabella, G.; Vurro, D.; Lai, S.; D'Angelo, P.; Ascari, L.; Iannotta, S. Aerosol Jet Printing of PEDOT:PSS for Large Area Flexible Electronics. *Flexible and Printed Electronics* **2020**, *5* (1). https://doi.org/10.1088/2058-8585/ab61c4.

(98) Mahajan, A.; Frisbie, C. D.; Francis, L. F. Optimization of Aerosol Jet Printing for High-Resolution, High-Aspect Ratio Silver Lines. *ACS Appl Mater Interfaces* **2013**, *5* (11), 4856–4864. https://doi.org/10.1021/am400606y.

(99) Zare Bidoky, F.; Hyun, W. J.; Song, D.; Frisbie, C. D. Printed, 1 V Electrolyte-Gated Transistors Based on Poly(3-Hexylthiophene) Operating at >10 KHz on Plastic. *Appl Phys Lett* **2018**, *113* (5). https://doi.org/10.1063/1.5025475.

(100) Xie, W.; Frisbie, C. D. Organic Electrical Double Layer Transistors Based on Rubrene Single Crystals: Examining Transport at High Surface Charge Densities above 10 13 Cm-2. *Journal of Physical Chemistry C* **2011**, *115* (29), 14360–14368. https://doi.org/10.1021/jp204152y.

(101) Marques, G. C.; Von Seggern, F.; Dehm, S.; Breitung, B.; Hahn, H.; Dasgupta, S.; Tahoori, M. B.; Aghassi-Hagmann, J. Influence of Humidity on the Performance of Composite Polymer Electrolyte-Gated Field-Effect Transistors and Circuits. *IEEE Trans Electron Devices* **2019**, *66* (5), 2202–2207. https://doi.org/10.1109/TED.2019.2903456.

(102) Lücke, A.; Schmidt, W. G.; Rauls, E.; Ortmann, F.; Gerstmann, U. Influence of Structural Defects and Oxidation onto Hole Conductivity in P3HT. *Journal of Physical Chemistry B* **2015**, *119* (21), 6481–6491. https://doi.org/10.1021/acs.jpcb.5b03615.

(103) Li, D.; Borkent, E. J.; Nortrup, R.; Moon, H.; Katz, H.; Bao, Z. Humidity Effect on Electrical Performance of Organic Thin-Film Transistors. *Appl Phys Lett* **2005**, *86* (4). https://doi.org/10.1063/1.1852708.

(104) Peixoto, M. M.; Bauerfeldt, G. F.; Herbst, M. H.; Pereira, M. S.; Da Silva, C. O. Study of the Stepwise Deprotonation Reactions of Glyphosate and the Corresponding p K a Values in Aqueous Solution. *Journal of Physical Chemistry A* **2015**, *119* (21), 5241–5249. https://doi.org/10.1021/jp5099552.

(105) Benbrook, C. M. How Did the US EPA and IARC Reach Diametrically Opposed Conclusions on the Genotoxicity of Glyphosate-Based Herbicides? *Environ Sci Eur* **2019**, *31* (2). https://doi.org/10.1186/s12302-018-0184-7.

(106) Snyder, A. Environmental Protection Agency 40 CFR Ch.1 (7-1-19 Edition). *180.364 Glyphosate; tolerances for residues*. 2019, pp 565–566.

(107) Lee, E. H.; Lim, H. J.; Lee, S. D.; Son, A. Highly Sensitive Detection of Bisphenol A by NanoAptamer Assay with Truncated Aptamer. *ACS Appl Mater Interfaces* **2017**, *9* (17), 14889–14898. https://doi.org/10.1021/acsami.7b02377.

(108) Dhamu, V. N.; Prasad, S. ElectrochemSENSE: A Platform towards Field Deployable Direct on-Produce Glyphosate Detection. *Biosens Bioelectron* **2020**, *170* (112609). https://doi.org/10.1016/j.bios.2020.112609.

(109) Dhamu, V. N.; Poudyal, D. C.; Muthukumar, S.; Prasad, S. A Highly Sensitive Electrochemical Sensor System to Detect and Distinguish Between Glyphosate and Glufosinate. *J Electrochem Soc* **2021**, *168* (5), 057531. https://doi.org/10.1149/1945-7111/ac00f7.

(110) Poudyal, D. C.; Dhamu, V. N.; Samson, M.; Muthukumar, S.; Prasad, S. Portable Pesticide Electrochem-Sensor: A Label-Free Detection of Glyphosate in Human Urine. *Langmuir* **2022**, *38* (5), 1781–1790. https://doi.org/10.1021/acs.langmuir.1c02877.

(111) Chergui, S.; Rhili, K.; Abrego-Martinez, J. C.; Jiménez, G. C.; Siaj, M. Selection of Highly Specific Aptamers by Graphene Oxide-SELEX to Ultrasensitive Label-Free Impedimetric Biosensor Development for Glyphosate Detection. *ACS Agricultural Science and Technology* **2021**, *1* (6), 655–663. https://doi.org/10.1021/acsagscitech.1c00147.

(112) Snow, A. W.; Jernigan, G. G.; Ancona, M. G. Packing Density of HS(CH2)NCOOH Self-Assembled Monolayers. *Analyst* **2011**, *136* (23), 4935–4949. https://doi.org/10.1039/c1an15664k.

(113) Holzer, B.; Manoli, K.; Ditaranto, N.; Macchia, E.; Tiwari, A.; Di Franco, C.; Scamarcio, G.; Palazzo, G.; Torsi, L. Characterization of Covalently Bound Anti-Human Immunoglobulins on Self-Assembled Monolayer Modified Gold Electrodes. *Adv Biosyst* **2017**, *1* (11). https://doi.org/10.1002/adbi.201700055.

(114) Sam, S.; Touahir, L.; Salvador Andresa, J.; Allongue, P.; Chazalviel, J. N.; Gouget-Laemmel, A. C.; De Villeneuve, C. H.; Moraillon, A.; Ozanam, F.; Gabouze, N.; Djebbar, S. Semiquantitative Study of the EDC/NHS Activation of Acid Terminal Groups at Modified Porous Silicon Surfaces. *Langmuir* **2010**, *26* (2), 809–814. https://doi.org/10.1021/la902220a.

(115) Tsai, T. C.; Liu, C. W.; Wu, Y. C.; Ondevilla, N. A. P.; Osawa, M.; Chang, H. C. In Situ Study of EDC/NHS Immobilization on Gold Surface Based on Attenuated Total Reflection Surface-Enhanced Infrared Absorption Spectroscopy (ATR-SEIRAS). *Colloids Surf B Biointerfaces* **2019**, *175*, 300–305. https://doi.org/10.1016/j.colsurfb.2018.12.009.

(116) Palazon, F.; Montenegro Benavides, C.; Léonard, D.; Souteyrand, É.; Chevolot, Y.; Cloarec, J. P. Carbodiimide/NHS Derivatization of COOH-Terminated SAMs: Activation or Byproduct Formation? *Langmuir* **2014**, *30* (16), 4545–4550. https://doi.org/10.1021/la5004269.

(117) Sun, Y.; Du, H.; Feng, C.; Lan, Y. Oriented Immobilization of Antibody through Carbodiimide Reaction and Controlling Electric Field. *Journal of Solid State Electrochemistry* **2015**, *19* (10), 3035–3043. https://doi.org/10.1007/s10008-015-2912-x.

(118) Menz, B.; Knerr, R.; Göpferich, A.; Steinem, C. Impedance and QCM Analysis of the Protein Resistance of Self-Assembled PEGylated Alkanethiol Layers on Gold. *Biomaterials* **2005**, *26* (20), 4237–4243. https://doi.org/10.1016/j.biomaterials.2004.10.038.

(119) Gao, N.; Gao, T.; Yang, X.; Dai, X.; Zhou, W.; Zhang, A.; Lieber, C. M. Specific Detection of Biomolecules in Physiological Solutions Using Graphene Transistor Biosensors. *Proc Natl Acad Sci U S A* **2016**, *113* (51), 14633–14638. https://doi.org/10.1073/pnas.1625010114.

(120) Gutiérrez-Sanz, Ó.; Andoy, N. M.; Filipiak, M. S.; Haustein, N.; Tarasov, A. Direct, Label-Free, and Rapid Transistor-Based Immunodetection in Whole Serum. *ACS Sens* **2017**, *2* (9), 1278–1286. https://doi.org/10.1021/acssensors.7b00187.

(121) García-Chamé, M. Á.; Gutiérrez-Sanz, Ó.; Ercan-Herbst, E.; Haustein, N.; Filipiak, M. S.; Ehrnhöfer, D. E.; Tarasov, A. A Transistor-Based Label-Free Immunosensor for Rapid Detection of Tau Protein. *Biosens Bioelectron* **2020**, *159* (112129). https://doi.org/10.1016/j.bios.2020.112129.

(122) Krishna, D. N. G.; Philip, J. Review on Surface-Characterization Applications of X-Ray Photoelectron Spectroscopy (XPS): Recent Developments and Challenges. *Applied Surface Science Advances*. Elsevier B.V. December 1, 2022. https://doi.org/10.1016/j.apsadv.2022.100332.

(123) Lee, C. Y.; Gong, P.; Harbers, G. M.; Grainger, D. W.; Castner, D. G.; Gamble, L. J. Surface Coverage and Structure of Mixed DNA/Alkylthiol Monolayers on Gold: Characterization by XPS, NEXAFS, and Fluorescence Intensity Measurements. *Anal Chem* **2006**, *78* (10), 3316–3325. https://doi.org/10.1021/ac052137j.

(124) Stettner, J.; Frank, P.; Griesser, T.; Trimmel, G.; Schennach, R.; Gilli, E.; Winkler, A. A Study on the Formation and Thermal Stability of 11-MUA SAMs on Au(111)/Mica and on Polycrystalline Gold Foils. *Langmuir* **2009**, *25* (3), 1427–1433. https://doi.org/10.1021/la802534q.

(125) Cecchet, F.; Marcaccio, M.; Margotti, M.; Paolucci, F.; Rapino, S.; Rudolf, P. Redox Mediation at 11-Mercaptoundecanoic Acid Self-Assembled Monolayers on Gold. *Journal of Physical Chemistry B* **2006**, *110* (5), 2241–2248. https://doi.org/10.1021/jp054290n.

(126) Cecchet, F.; Fioravanti, G.; Marcaccio, M.; Margotti, M.; Mattiello, L.; Paolucci, F.; Rapino, S.; Rudolf, P. Electrode Surface Modification by a Spirobifluorene Derivative. An

XPS and Electrochemical Investigation. *Journal of Physical Chemistry B* **2005**, *109* (39), 18427–18432. https://doi.org/10.1021/jp051786w.

(127) López, G. P.; Castner, D. G.; Ratner, B. D. XPS O 1s Binding Energies for Polymers Containing Hydroxyl, Ether, Ketone and Ester Groups. *Surface and Interface Analysis* **1991**, *17* (5), 267–272. https://doi.org/10.1002/sia.740170508.

(128) Cerruti, M.; Fissolo, S.; Carraro, C.; Ricciardi, C.; Majumdar, A.; Maboudian, R. Poly(Ethylene Glycol) Monolayer Formation and Stability on Gold and Silicon Nitride Substrates. *Langmuir* **2008**, *24* (19), 10646–10653. https://doi.org/10.1021/la801357v.

(129) Ranjan, R.; Trenary, M. Reflection Absorption Infrared Spectroscopy. In *Springer Handbook of Advanced Catalyst Characterization*; 2023; Vol. 1, pp 53–71.

(130) Touahir, L.; Chazalviel, J. N.; Sam, S.; Moraillon, A.; Henry De Villeneuve, C.; Allongue, P.; Ozanam, F.; Gouget-Laemmel, A. C. Kinetics of Activation of Carboxyls to Succinimidyl Ester Groups in Monolayers Grafted on Silicon: An in Situ Real-Time Infrared Spectroscopy Study. *Journal of Physical Chemistry C* **2011**, *115* (14), 6782–6787. https://doi.org/10.1021/jp200150m.

(131) Lim, C. Y.; Owens, N. A.; Wampler, R. D.; Ying, Y.; Granger, J. H.; Porter, M. D.; Takahashi, M.; Shimazu, K. Succinimidyl Ester Surface Chemistry: Implications of the Competition between Aminolysis and Hydrolysis on Covalent Protein Immobilization. *Langmuir* **2014**, *30* (43), 12868–12878. https://doi.org/10.1021/la503439g.

(132) Sadat, A.; Joye, I. J. Peak Fitting Applied to Fourier Transform Infrared and Raman Spectroscopic Analysis of Proteins. *Applied Sciences (Switzerland)* **2020**, *10* (17). https://doi.org/10.3390/app10175918.

(133) Krimm, S.; Bandekar, J. Vibrational Spectroscopy and Conformation of Peptides, Polypeptides, and Proteins. In *Advances in Protein Chemistry*; 1986; Vol. 38, pp 181–364.

(134) Fischer, L. M.; Tenje, M.; Heiskanen, A. R.; Masuda, N.; Castillo, J.; Bentien, A.; Émneus, J.; Jakobsen, M. H.; Boisen, A. Gold Cleaning Methods for Electrochemical Detection Applications. *Microelectron Eng* **2009**, *86* (4–6), 1282–1285. https://doi.org/10.1016/j.mee.2008.11.045.

(135) Alloway, D. M.; Hofmann, M.; Smith, D. L.; Gruhn, N. E.; Graham, A. L.; Colorado, R.; Wysocki, V. H.; Lee, T. R.; Lee, P. A.; Armstrong, N. R. Interface Dipoles Arising from Self-Assembled Monolayers on Gold: UV-Photoemission Studies of Alkanethiols and Partially Fluorinated Alkanethiols. *J. Phys. Chem. B* **2003**, *107* (42), 11690–11699. https://doi.org/10.1021/jp034665.

(136) Kim, J.; Gulans, A.; Draxl, C. Work-Function Modification of PEG(Thiol) Adsorbed on the Au(111) Surface: A First-Principles Study. *Phys Rev Mater* **2020**, *4* (11). https://doi.org/10.1103/PhysRevMaterials.4.116001.

(137) Bard, A. J.; Faulkner, L. R. *Electrochemical Methods: Fundamentals and Applications*; John Wiley, 2001.

(138) Bakhtiar, R. Surface Plasmon Resonance Spectroscopy: A Versatile Technique in a Biochemist's Toolbox. *J Chem Educ* **2013**, *90* (2), 203–209. https://doi.org/10.1021/ed200549g.
(139) Tan, Y. H.; Liu, M.; Nolting, B.; Go, J. G.; Gervay-Hague, J.; Liu, G. Y. A Nanoengineering Approach for Investigation and Regulation of Protein Immobilization. *ACS Nano* **2008**, *2* (11), 2374–2384. https://doi.org/10.1021/nn800508f.
(140) Jin, B. K.; Odongo, S.; Radwanska, M.; Magez, S. Nanobodies: A Review of Generation, Diagnostics and Therapeutics. *International Journal of Molecular Sciences*. MDPI March 1, 2023. https://doi.org/10.3390/ijms24065994.
(141) Stuber, A.; Douaki, A.; Hengsteler, J.; Buckingham, D.; Momotenko, D.; Garoli, D.; Nakatsuka, N. Aptamer Conformational Dynamics Modulate Neurotransmitter Sensing in Nanopores. *bioRxiv* **2023**, No. preprint. https://doi.org/10.1101/2023.03.10.532011.
(142) Güell, A. G.; Meadows, K. E.; Unwin, P. R.; MacPherson, J. V. Trace Voltammetric Detection of Serotonin at Carbon Electrodes: Comparison of Glassy Carbon, Boron Doped Diamond and Carbon Nanotube Network Electrodes. *Phys Chem Chem Phys* **2010**, *12* (34), 10108–10114. https://doi.org/10.1039/C0CP00675K.
(143) Abdalla, A.; Atcherley, C. W.; Pathirathna, P.; Samaranayake, S.; Qiang, B.; Peña, E.; Morgan, S. L.; Heien, M. L.; Hashemi, P. In Vivo Ambient Serotonin Measurements at Carbon-Fiber Microelectrodes. *Anal Chem* **2017**, *89* (18), 9703–9711. https://doi.org/10.1021/acs.analchem.7b01257.
(144) Al-Graiti, W.; Foroughi, J.; Liu, Y.; Chen, J. Hybrid Graphene/Conducting Polymer Strip Sensors for Sensitive and Selective Electrochemical Detection of Serotonin. *ACS Omega* **2019**, *4* (26), 22169–22177. https://doi.org/10.1021/acsomega.9b03456.
(145) Li, R.; Li, X.; Su, L.; Qi, H.; Yue, X.; Qi, H. Label-Free Electrochemical Aptasensor for the Determination of Serotonin. *Electroanalysis* **2022**, *34* (6), 1048–1053. https://doi.org/10.1002/elan.202100373.
(146) Nakatsuka, N.; Faillétaz, A.; Eggemann, D.; Forró, C.; Vörös, J.; Momotenko, D. Aptamer Conformational Change Enables Serotonin Biosensing with Nanopipettes. *Anal Chem* **2021**, *93* (8), 4033–4041. https://doi.org/10.1021/acs.analchem.0c05038.
(147) Nakatsuka, N.; Heard, K. J.; Faillétaz, A.; Momotenko, D.; Vörös, J.; Gage, F. H.; Vadodaria, K. C. Sensing Serotonin Secreted from Human Serotonergic Neurons Using Aptamer-Modified Nanopipettes. *Mol Psychiatry* **2021**, *26* (7), 2753–2763. https://doi.org/10.1038/s41380-021-01066-5.
(148) Nakatsuka, N.; Abendroth, J. M.; Yang, K. A.; Andrews, A. M. Divalent Cation Dependence Enhances Dopamine Aptamer Biosensing. *ACS Appl Mater Interfaces* **2021**, *13* (8), 9425–9435. https://doi.org/10.1021/acsami.0c17535.
(149) Zhao, C.; Cheung, K. M.; Huang, I. W.; Yang, H.; Nakatsuka, N.; Liu, W.; Cao, Y.; Man, T.; Weiss, P. S.; Monbouquette, H. G.; Andrews, A. M. Implantable Aptamer-Field-Effect

Transistor Neuroprobes for in Vivo Neurotransmitter Monitoring. *Sci Adv* **2021**, *7* (48), 25–27. https://doi.org/10.1126/sciadv.abj7422.

(150) Zhao, C.; Man, T.; Cao, Y.; Weiss, P. S.; Monbouquette, H. G.; Andrews, A. M. Flexible and Implantable Polyimide Aptamer-Field-Effect Transistor Biosensors. *ACS Sens* **2022**, *7* (12), 3644–3653. https://doi.org/10.1021/acssensors.2c01909.

(151) Wang, B.; Zhao, C.; Wang, Z.; Yang, K.-A.; Cheng, X.; Liu, W.; Yu, W.; Lin, S.; Zhao, Y.; Cheung, K. M.; Lin, H.; Hojaiji, H.; Weiss, P. S.; Stojanović, M. N.; Tomiyama, A. J.; Andrews, A. M.; Emaminejad, S. Wearable Aptamer-Field-Effect Transistor Sensing System for Noninvasive Cortisol Monitoring. *Sci. Adv.* **2022**, *8* (1).

(152) Chavan, S. G.; Yagati, A. K.; Koyappayil, A.; Go, A.; Yeon, S.; Lee, T.; Lee, M. H. Conformationally Flexible Dimeric-Serotonin-Based Sensitive and Selective Electrochemical Biosensing Strategy for Serotonin Recognition. *Anal Chem* **2022**. https://doi.org/10.1021/acs.analchem.2c02747.

(153) Froehlich, C. E.; He, J.; Haynes, C. L. Investigation of Charged Small Molecule-Aptamer Interactions with Surface Plasmon Resonance. *Anal Chem* **2023**, *95* (5), 2639–2644. https://doi.org/doi.org/10.1021/acs.analchem.2c04192.

(154) Cao, H. H.; Nakatsuka, N.; Serino, A. C.; Liao, W. S.; Cheunkar, S.; Yang, H.; Weiss, P. S.; Andrews, A. M. Controlled DNA Patterning by Chemical Lift-Off Lithography: Matrix Matters. *ACS Nano* **2015**, *9* (11), 11439–11454. https://doi.org/10.1021/acsnano.5b05546.

(155) Dejeu, J.; Bonnet, H.; Coche-Guérente, L.; Defrancq, E.; Spinelli, N.; van der Heyden, A. Negative SPR Signals during Low Molecular Weight Analyte Recognition. *Anal Chem* **2021**, *93* (8), 4134–4140. https://doi.org/10.1021/acs.analchem.1c00071.

(156) Ishino, K.; Nishitani, S.; Man, Y.; Saito, A.; Sakata, T. Surface Characteristics and Formation of Polyserotonin Thin Films for Bioelectrical and Biocompatible Interfaces. *Langmuir* **2022**, *38* (28), 8633–8642. https://doi.org/10.1021/acs.langmuir.2c01045.

(157) Kummer, K.; Vyalikh, D. V.; Gavrila, G.; Kade, A.; Weigel-Jech, M.; Mertig, M.; Molodtsov, S. L. High-Resolution Photoelectron Spectroscopy of Self-Assembled Mercaptohexanol Monolayers on Gold Surfaces. *J Electron Spectros Relat Phenomena* **2008**, *163* (1–3), 59–64. https://doi.org/10.1016/j.elspec.2008.02.005.

(158) Schoenfisch, M. H.; Pemberton, J. E. Air Stability of Alkanethiol Self-Assembled Monolayers on Silver and Gold Surfaces. *J Am Chem Soc* **1998**, *120* (18), 4502–5413. https://doi.org/10.1021/ja974301t.

(159) Wackerbarth, H.; Grubb, M.; Zhang, J.; Hansen, A. G.; Ulstrup, J. Long-Range Order of Organized Oligonucleotide Monolayers on Au(111) Electrodes. *Langmuir* **2004**, *20* (5), 1647–1655. https://doi.org/10.1021/la035547g.

(160) Liu, X.; He, F.; Zhang, F.; Zhang, Z.; Huang, Z.; Liu, J. Dopamine and Melamine Binding to Gold Nanoparticles Dominates Their Aptamer-Based Label-Free Colorimetric Sensing. *Anal Chem* **2020**, *92* (13), 9370–9378. https://doi.org/10.1021/acs.analchem.0c01773.

(161) Li, J.; Sun, C. L.; An, P.; Liu, X.; Dong, R.; Sun, J.; Zhang, X.; Xie, Y.; Qin, C.; Zheng, W.; Zhang, H. L.; Jiang, X. Construction of Dopamine-Releasing Gold Surfaces Mimicking Presynaptic Membrane by On-Chip Electrochemistry. *J Am Chem Soc* **2019**, *141* (22), 8816–8824. https://doi.org/10.1021/jacs.9b01003.

(162) Do, P. Q. T.; Huong, V. T.; Phuong, N. T. T.; Nguyen, T. H.; Ta, H. K. T.; Ju, H.; Phan, T. B.; Phung, V. D.; Trinh, K. T. L.; Tran, N. H. T. The Highly Sensitive Determination of Serotonin by Using Gold Nanoparticles (Au NPs) with a Localized Surface Plasmon Resonance (LSPR) Absorption Wavelength in the Visible Region. *RSC Adv* **2020**, *10* (51), 30858–30869. https://doi.org/10.1039/d0ra05271j.

(163) Wang, P.; Xia, M.; Liang, O.; Sun, K.; Cipriano, A. F.; Schroeder, T.; Liu, H.; Xie, Y. H. Label-Free SERS Selective Detection of Dopamine and Serotonin Using Graphene-Au Nanopyramid Heterostructure. *Anal Chem* **2015**, *87* (20), 10255–10261. https://doi.org/10.1021/acs.analchem.5b01560.

(164) Lee, W.; Kang, B. H.; Yang, H.; Park, M.; Kwak, J. H.; Chung, T.; Jeong, Y.; Kim, B. K.; Jeong, K. H. Spread Spectrum SERS Allows Label-Free Detection of Attomolar Neurotransmitters. *Nat Commun* **2021**, *12* (1). https://doi.org/10.1038/s41467-020-20413-8.

(165) Wei, X.; Wang, F.; Yin, Y.; Liu, Q.; Zou, L.; Ye, B. Selective Detection of Neurotransmitter Serotonin by a Gold Nanoparticle-Modified Glassy Carbon Electrode. *Analyst* **2010**, *135* (9), 2286–2290. https://doi.org/10.1039/c0an00256a.

(166) Chapin, A. A.; Rajasekaran, P. R.; Quan, D. N.; Hu, L.; Herberholz, J.; Bentley, W. E.; Ghodssi, R. Electrochemical Measurement of Serotonin by Au-CNT Electrodes Fabricated on Microporous Cell Culture Membranes. *Microsyst Nanoeng* **2020**, *6* (1). https://doi.org/10.1038/s41378-020-00184-4.

(167) Lane, R. F.; Blaha, C. D. Detection of Catecholamines in Brain Tissue: Surface-Modified Electrodes Enabling in Vivo Investigations of Dopamine Function. *Langmuir* **1990**, *6* (1), 56–65. https://doi.org/https://doi.org/10.1021/la00091a009.

(168) Kim, D. S.; Kang, E. S.; Baek, S.; Choo, S. S.; Chung, Y. H.; Lee, D.; Min, J.; Kim, T. H. Electrochemical Detection of Dopamine Using Periodic Cylindrical Gold Nanoelectrode Arrays. *Sci Rep* **2018**, *8* (1), 1–10. https://doi.org/10.1038/s41598-018-32477-0.

(169) Tortolini, C.; Cass, A. E. G.; Pofi, R.; Lenzi, A.; Antiochia, R. Microneedle-Based Nanoporous Gold Electrochemical Sensor for Real-Time Catecholamine Detection. *Microchimica Acta* **2022**, *189* (5). https://doi.org/10.1007/s00604-022-05260-2.

(170) Muglali, M. I.; Bashir, A.; Rohwerder, M. A Study on Oxygen Reduction Inhibition at Pyridine-Terminated Self Assembled Monolayer Modified Au(111) Electrodes. *Physica Status Solidi (A) Applications and Materials Science* **2010**, *207* (4), 793–800. https://doi.org/10.1002/pssa.200983321.

(171) Lin, H. K.; Chen, X. Electrochemical Study of Gold Dissolution in Cyanide Solution. *Minerals & Metallurgical Processing* **2001**, *18* (3), 147–153.

(172) Hua, X.; Xia, H. L.; Long, Y. T. Revisiting a Classical Redox Process on a Gold Electrode by Operando ToF-SIMS: Where Does the Gold Go? *Chem Sci* **2019**, *10* (24), 6215–6219. https://doi.org/10.1039/c9sc00956f.

(173) Vogt, S.; Su, Q.; Gutiérrez-Sánchez, C.; Nöll, G. Critical View on Electrochemical Impedance Spectroscopy Using the Ferri/Ferrocyanide Redox Couple at Gold Electrodes. *Anal Chem* **2016**, *88* (8), 4383–4390. https://doi.org/10.1021/acs.analchem.5b04814.

(174) Dijksma, M.; Boukamp, B. A.; Kamp, B.; Van Bennekom, W. P. Effect of Hexacyanoferrate(II/III) on Self-Assembled Monolayers of Thioctic Acid and 11-Mercaptoundecanoic Acid on Gold. *Langmuir* **2002**, *18* (8), 3105–3112. https://doi.org/10.1021/la010898l.

(175) Xu, X.; Makaraviciute, A.; Kumar, S.; Wen, C.; Sjödin, M.; Abdurakhmanov, E.; Danielson, U. H.; Nyholm, L.; Zhang, Z. Structural Changes of Mercaptohexanol Self-Assembled Monolayers on Gold and Their Influence on Impedimetric Aptamer Sensors. *Anal Chem* **2019**. https://doi.org/10.1021/acs.analchem.9b03946.

(176) Seo, K.; Borguet, E. Potential-Induced Structural Change in a Self-Assembled Monolayer of 4-Methylbenzenethiol on Au(111). *Journal of Physical Chemistry C* **2007**, *111* (17), 6335–6342. https://doi.org/10.1021/jp064493r.

(177) Demissie, A. T.; Haugstad, G.; Frisbie, C. D. Quantitative Surface Coverage Measurements of Self-Assembled Monolayers by Nuclear Reaction Analysis of Carbon-12. *Journal of Physical Chemistry Letters* **2016**, *7* (17), 3477–3481. https://doi.org/10.1021/acs.jpclett.6b01363.

(178) Demissie, A. T.; Haugstad, G.; Frisbie, C. D. Growth of Thin, Anisotropic, π-Conjugated Molecular Films by Stepwise "Click" Assembly of Molecular Building Blocks: Characterizing Reaction Yield, Surface Coverage, and Film Thickness versus Addition Step Number. *J Am Chem Soc* **2015**, *137* (27), 8819–8828. https://doi.org/10.1021/jacs.5b04512.

(179) Kesler, V.; Murmann, B.; Soh, H. T. Going beyond the Debye Length: Overcoming Charge Screening Limitations in Next-Generation Bioelectronic Sensors. *ACS Nano* **2020**, *14* (12), 16194–16201. https://doi.org/10.1021/acsnano.0c08622.

(180) Kulkarni, G. S.; Zhong, Z. Detection beyond the Debye Screening Length in a High-Frequency Nanoelectronic Biosensor. *Nano Lett* **2012**, *12* (2), 719–723. https://doi.org/10.1021/nl203666a.

(181) Zare Bidoky, F.; Frisbie, C. D. Sub-3 V, MHz-Class Electrolyte-Gated Transistors and Inverters. *ACS Appl Mater Interfaces* **2022**. https://doi.org/10.1021/acsami.2c01585.

(182) Macchia, E.; Manoli, K.; Di Franco, C.; Scamarcio, G.; Torsi, L. New Trends in Single-Molecule Bioanalytical Detection. *Anal Bioanal Chem* **2020**, *412* (21), 5005–5014. https://doi.org/10.1007/s00216-020-02540-9.

(183) Macchia, E.; Manoli, K.; Holzer, B.; Di Franco, C.; Picca, R. A.; Cioffi, N.; Scamarcio, G.; Palazzo, G.; Torsi, L. Selective Single-Molecule Analytical Detection of C-Reactive Protein

in Saliva with an Organic Transistor. *Anal Bioanal Chem* **2019**, *411* (19), 4899–4908. https://doi.org/10.1007/s00216-019-01778-2.

(184) Macchia, E.; Manoli, K.; Holzer, B.; Di Franco, C.; Ghittorelli, M.; Torricelli, F.; Alberga, D.; Mangiatordi, G. F.; Palazzo, G.; Scamarcio, G.; Torsi, L. Single-Molecule Detection with a Millimetre-Sized Transistor. *Nat Commun* **2018**, *9* (1). https://doi.org/10.1038/s41467-018-05235-z.

(185) Macchia, E.; Tiwari, A.; Manoli, K.; Holzer, B.; Ditaranto, N.; Picca, R. A.; Cioffi, N.; Di Franco, C.; Scamarcio, G.; Palazzo, G.; Torsi, L. Label-Free and Selective Single-Molecule Bioelectronic Sensing with a Millimeter-Wide Self-Assembled Monolayer of Anti-Immunoglobulins. *Chemistry of Materials* **2019**, *31* (17), 6476–6483. https://doi.org/10.1021/acs.chemmater.8b04414.

(186) Kratz, C.; Furchner, A.; Sun, G.; Rappich, J.; Hinrichs, K. Sensing and Structure Analysis by in Situ IR Spectroscopy: From ML Flow Cells to Microfluidic Applications. *Journal of Physics Condensed Matter* **2020**, *32* (393002). https://doi.org/10.1088/1361-648X/ab8523.

(187) Kratz, C.; Furchner, A.; Oates, T. W. H.; Janasek, D.; Hinrichs, K. Nanoliter Sensing for Infrared Bioanalytics. *ACS Sens* **2018**, *3* (2), 299–303. https://doi.org/10.1021/acssensors.7b00902.

(188) Sun, G.; Zu, F.; Koch, N.; Rappich, J.; Hinrichs, K. In Situ Infrared Spectroscopic Monitoring and Characterization of the Growth of Polydopamine (PDA) Films. *Phys Status Solidi B Basic Res* **2019**, *256* (1800308). https://doi.org/10.1002/pssb.201800308.

(189) Sun, G.; Zhang, X.; Kaspari, C.; Haberland, K.; Rappich, J.; Hinrichs, K. In-Situ Monitoring the Growth of Polypyrrole Films at Liquid/Solid Interface Using a Combination of Polarized Infrared Spectroscopy and Reflectance Anisotropy Spectroscopy. *J Electrochem Soc* **2012**, *159* (10), H811–H815. https://doi.org/10.1149/2.044210jes.

(190) Mirsky, V. M.; Riepl, M.; Wolfbeis, O. S. Capacitive Monitoring of Protein Immobilization and Antigen-Antibody Reactions on Monomolecular Alkylthiol Films on Gold Electrodes. *Biosens Bioelectron* **1997**, *12* (9–10), 977–989. https://doi.org/10.1016/S0956-5663(97)00053-5.

Appendix A – EGT Studies

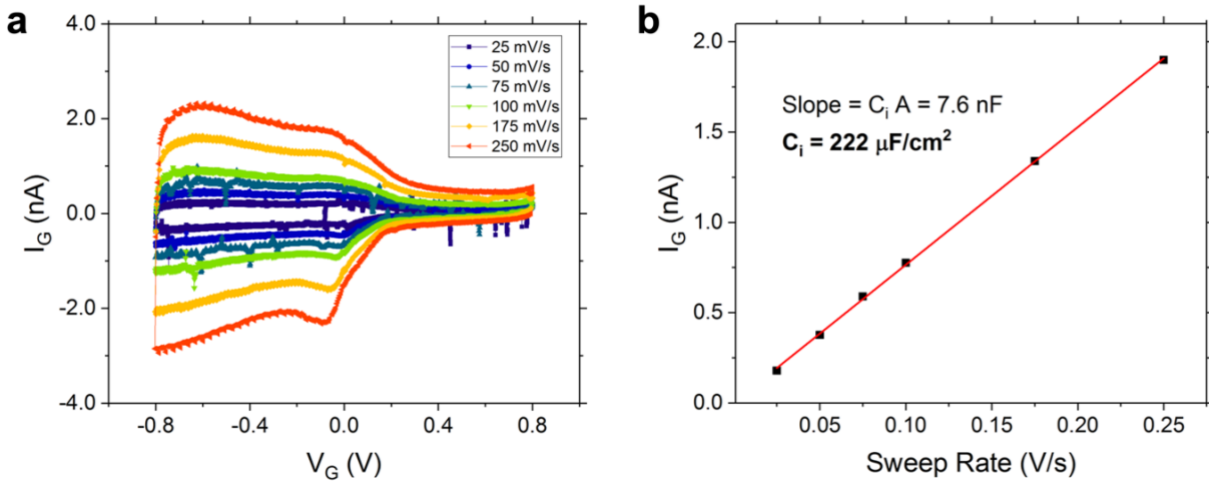

Figure A.1. Capacitance of P3HT/ion gel interface. (a) I_G–V_G characteristics obtained at various gate sweep rates for a 50 nm-thick P3HT EGT (V_D = 0 V) with a channel size of 100 μm x 20 μm. (b) The measured I_G at V_G = –0.3 V against the corresponding sweep rate. The slope of the fit is divided by the channel area to obtain $C_{i,P3HT/ion\ gel}$. Reprinted (adapted) with permission from Thomas, M.S.; Adrahtas, D.Z.; Frisbie, C.D.; and Dorfman K.D. Modeling of Quasi-Static Floating Gate Transistor Biosensors, *ACS Sensors* **2021**, *6* (5), 1910-1917. Copyright 2021 American Chemical Society.

Appendix B – Glyphosate FGT Biosensor Characterization

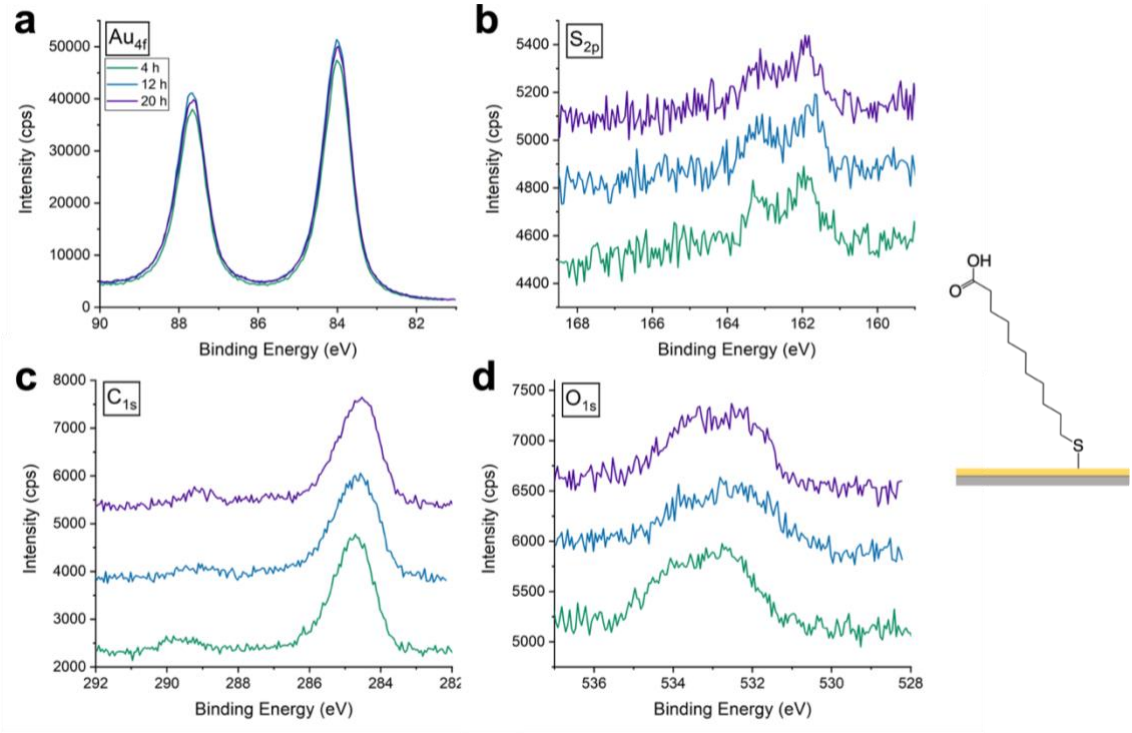

Figure B.1. XPS of time-dependent monolayer formation of 11-MUA. High-resolution XPS spectra of (a) Au_{4f}, (b) S_{2p}, (c) C_{1s}, and (d) O_{1s} orbitals of 1 mM 11-MUA on gold. Self-assembly times were 4 h (green), 8 h (blue), and 20 h (purple).

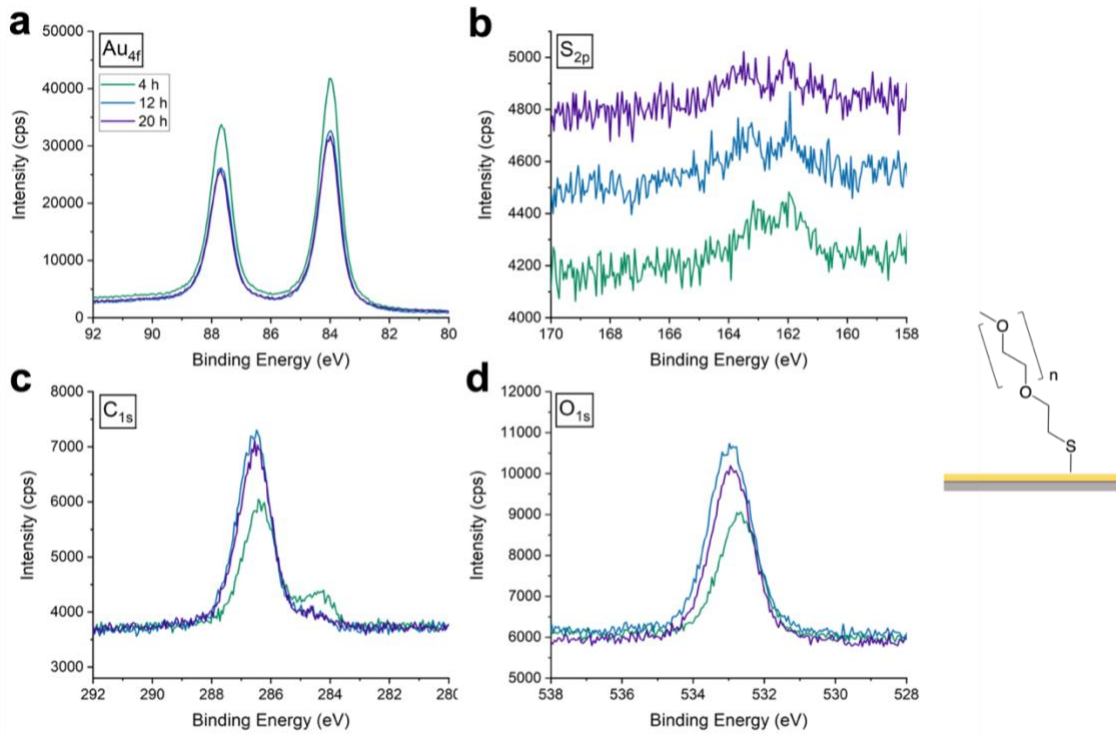

Figure B.2. XPS of time dependent monolayer formation of PEG thiol. High-resolution XPS spectra of (a) Au_{4f}, (b) S_{2p}, (c) C_{1s}, and (d) O_{1s} orbitals of 1 mM PEG methyl ether thiol on gold. Self-assembly times were 4 h (green), 8 h (blue), and 20 h (purple).

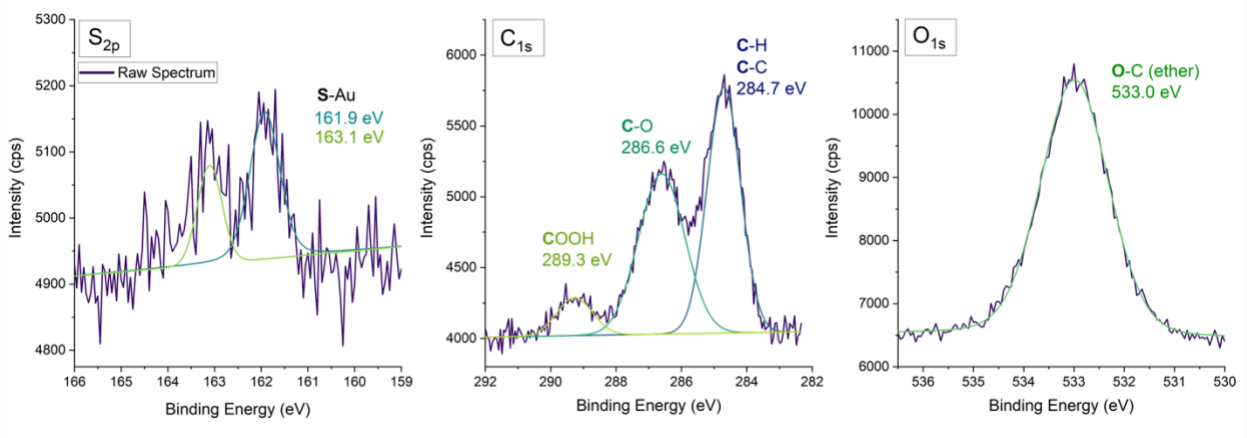

Figure B.3. XPS of 11-MUA and PEG thiol mixed monolayer (1:2 molar ratio). High-resolution XPS spectra of (a) Au_{4f}, (b) S_{2p}, (c) C_{1s}, and (d) O_{1s} orbitals of 1 mM 11-MUA and PEG methyl ether thiol (1:2 molar ratio) self-assembled for 20 h on gold.

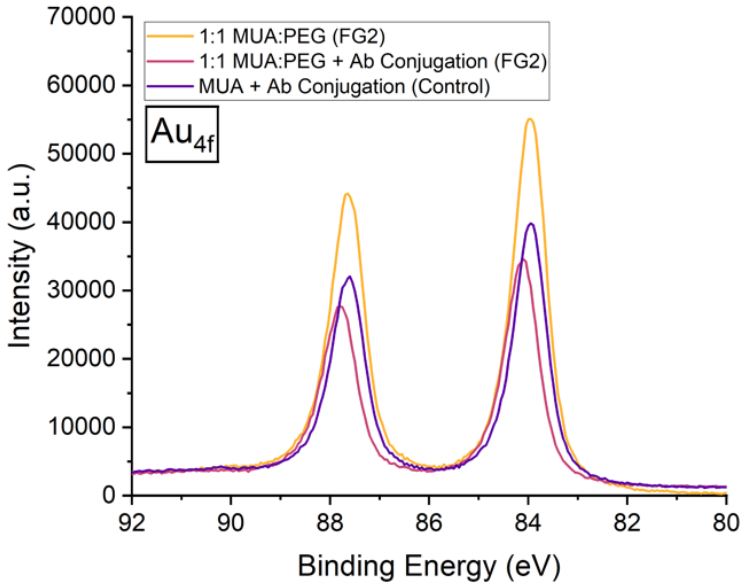

Figure B.4. XPS of Au_{4f} attenuation upon antibody conjugation. The high-resolution XPS spectra for the Au_{4f} orbital shows attenuation of the doublet for both FG2 (pink) and control (purple) electrodes compared to an FG2 electrode only containing the mixed monolayer (yellow).

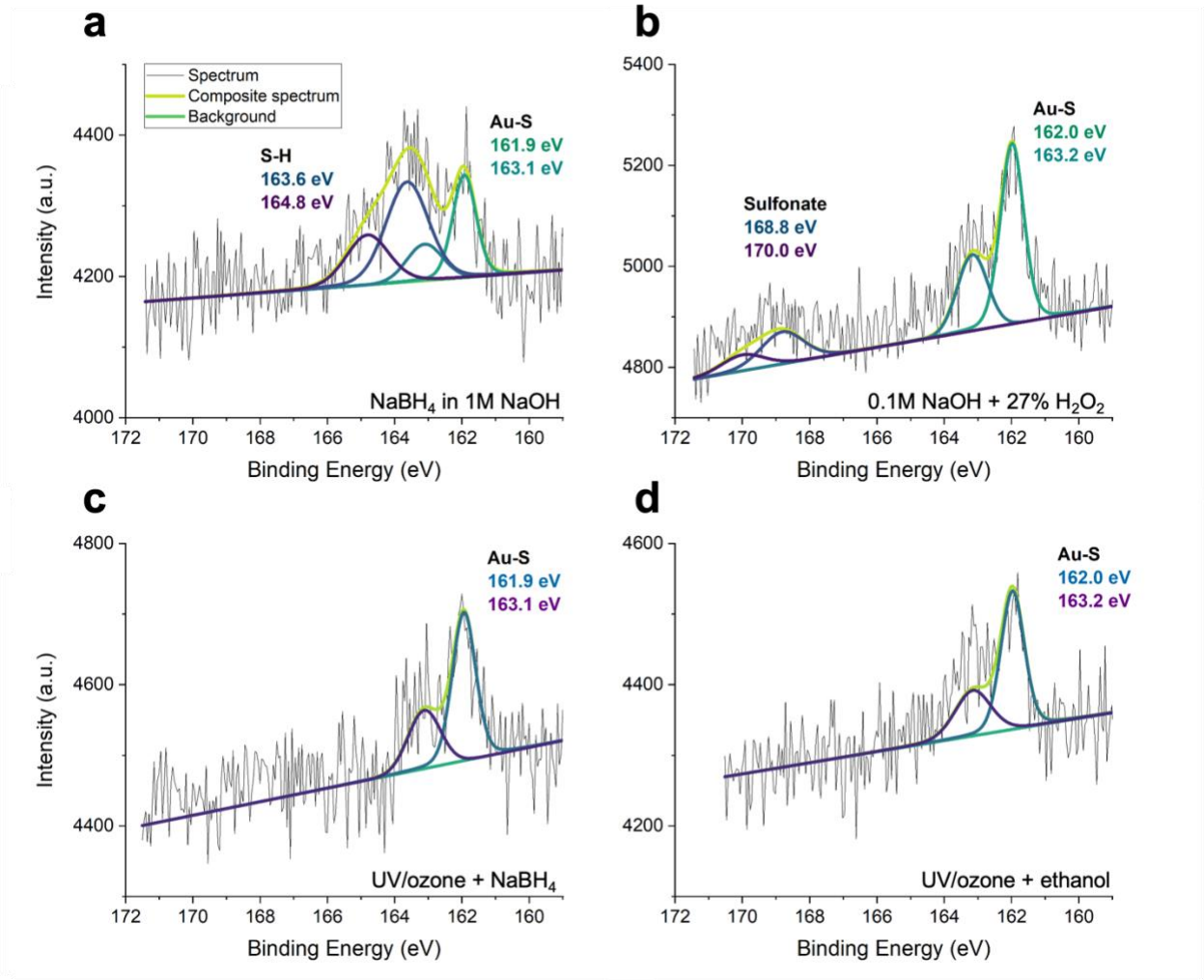

Figure B.5. XPS of self-assembly of 11-MUA with different gold cleaning protocols. High-resolution XPS spectra of S_{2p} orbital for 11-MUA functionalized FG2 electrodes. Cleaning methods prior to self-assembly were (a) $NaBH_4$ in 1M NaOH for 1h, (b) 0.1M NaOH + 27% H_2O_2 for 20 min, (c) UV/ozone for 10 min followed with $NaBH_4$ for 20 min, and (d) UV/ozone for 10 min followed with ethanol for 20 min.

Table B.1. Experimental conditions for glyphosate SPR trials.

Run #	Antibody Conditions	$R_{immobilization}$	Running Buffer
1	0.2 mg/mL in PBS-P+ (pH =7.4)	Poor < 2000 RU	1X PBS-P+
2	0.2 mg/mL in 10 mM sodium acetate (pH = 5.0)	High 11761 RU	1X PBS-P+
3	0.2 mg/mL in 10 mM sodium acetate (pH = 5.0)	High 12737 RU	1X PBS-P+
4	0.2 mg/mL in 10 mM sodium acetate (pH = 5.0)	High 12235 RU	1X PBS-P+
5	0.2 mg/mL in 10 mM sodium acetate (pH = 5.0)	High 16853 RU	1X PBS-P+
6	1.0 mg/mL in 1X PBS (pH = 7.4)	Low 4056 RU	1X PBS
7	0.5 mg/mL in 1X PBS (pH = 6.5)	Low 3053 RU	1X PBS
8	2.0 mg/mL in 1X PBS (pH = 7.4)	Low 4898 RU	1X PBS-P+ with 1M NaCl
9	0.2 mg/mL in 10 mM sodium acetate (pH = 5.0)	High	1X PBS-P+ with 1M NaCl

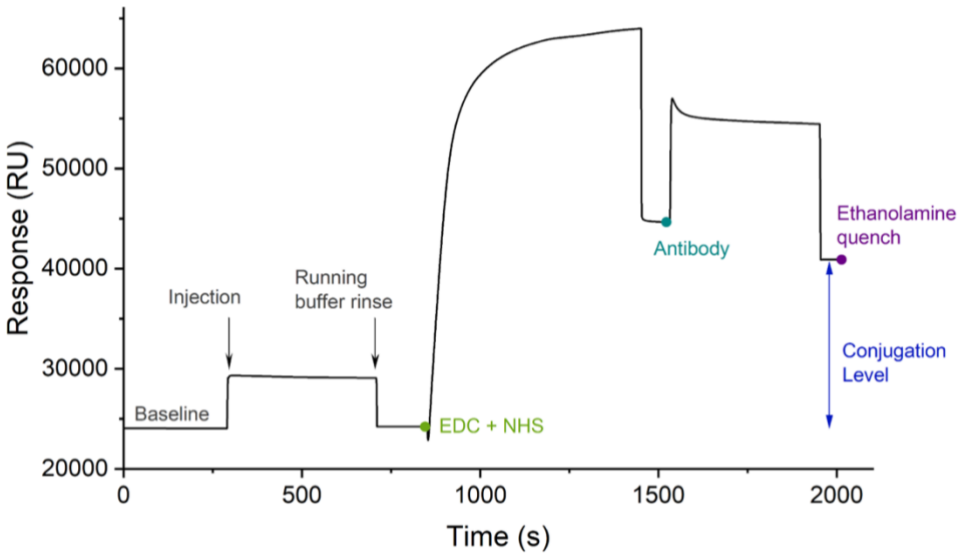

Figure B.6. Glyphosate antibody conjugation onto CM5 chip with SPR. At 0 s, the running buffer is flown over the chip as a baseline. Injection of the reactive species is indicated with the first arrow. The reactive species, EDC + NHS, is flown over the chip for 7 min then running buffer is flown over to rinse the surface and stabilize the response. The green, blue, and purple points indicate stable levels for EDC/NHS activation, antibody conjugation, and ethanolamine quenching. The blue arrow indicates the final antibody conjugation level

Appendix C – FGT Biosensor Design

The FGT biosensor was designed utilizing model predictions,[21] where the goal was to maximize charge-based sensing with both the antibody/PEG- an aptamer/MCH- functionalized surface. The specific capacitances of the P3HT/ion gel, FG1/ion gel, antibody/PEG, aptamer/MCH, and CG/PBS interfaces were estimated as 209 $\mu F/cm^2$,[21] 12.5 $\mu F/cm^2$,[19,95] 3 $\mu F/cm^2$,[118,190] 4 $\mu F/cm^2$,[146] and 10 $\mu F/cm^2$,[20] respectively. Since the capacitance is simply the product of the specific capacitance and area of the interface, the optimal capacitances for charge-based FGT sensing were used to determine the area of each interface. Parameters considered were the amplitude of V_{DD}, size of R_L, and estimated capacitances of each interface. Considering the mobility of P3HT (0.4 cm^2/Vs), the size of R_L (1 MΩ), and the channel dimensions, the value for P was estimated as 0.5 $\mu VF/cm^2$.[21] We settled on a design in which $C_2 \sim 110$ nF and $C_0 \sim 6$ nF to place the sensor in a regime where $C_0/C_2 << 1$ (Eq 1.4) and charge-based signals were dominant and maximized.[21] Additionally, $C_{CG}/C_2 > 10$ and $C_1/C_0 > 100$ in order to minimize potential losses over the sensing medium and ion gel electrolyte (i.e improve coupling). The control gate (CG) was 3.36 mm x 3.36 mm. The upper end of the floating gate (FG2) was 2.8 mm x 1.0 mm. The lower end of the floating gate (FG1) was 3.0 x 2.0 mm. The source and drain electrodes were 100 µm x 10 µm, leading to a channel of 100 µm x 20 µm. The dimensions of the printed P3HT channel was estimated as 100 x 30 µm.

Appendix D – Serotonin FGT Biosensor Characterization

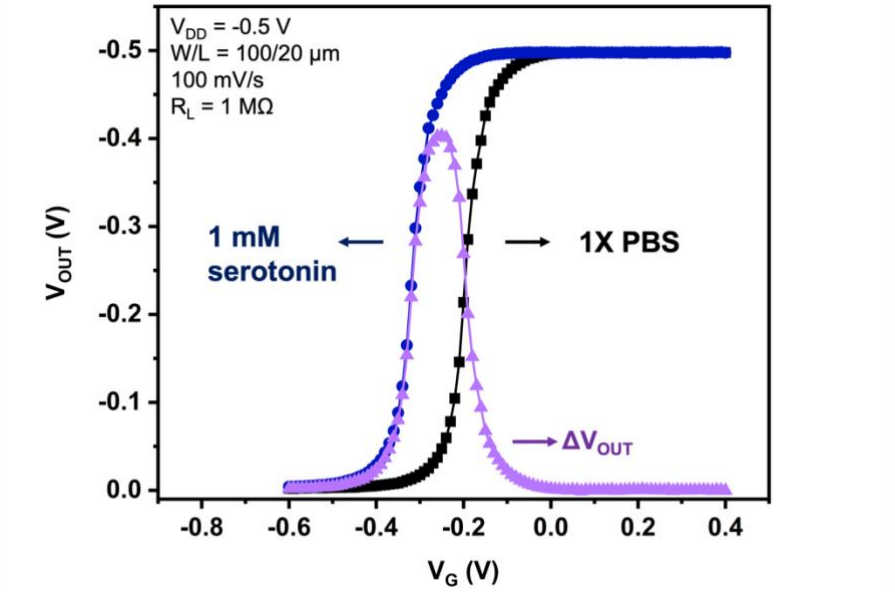

Figure D.1. Serotonin FGT inverter curve shift after serotonin dosing. The serotonin FGT inverter curves after stabilization in 1X PBS (black) and dosing in 1 mM serotonin (blue). The subtraction of the 1X PBS curve from the serotonin curve produces the signal readout, ΔV_{OUT} (purple). The maximum value of ΔV_{OUT} is the signal. Inverter curves are of the backward sweep.

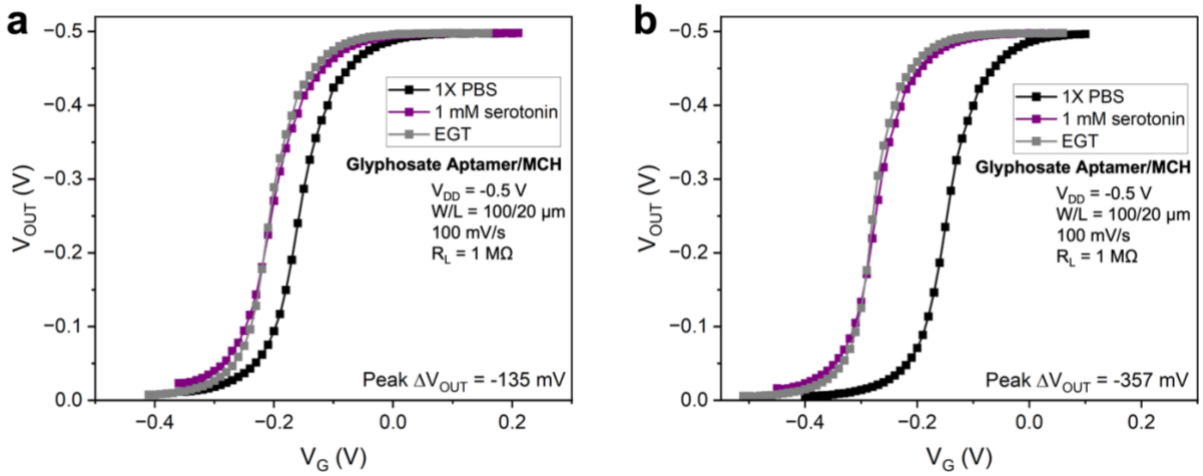

Figure D.2. Response to serotonin depends on the functionalization response. (a) Small shift and (b) large shift of the FGT with respect to the EGT-subunit is proportional to the response to 1 mM serotonin. Inverter curves are of the backward sweep.

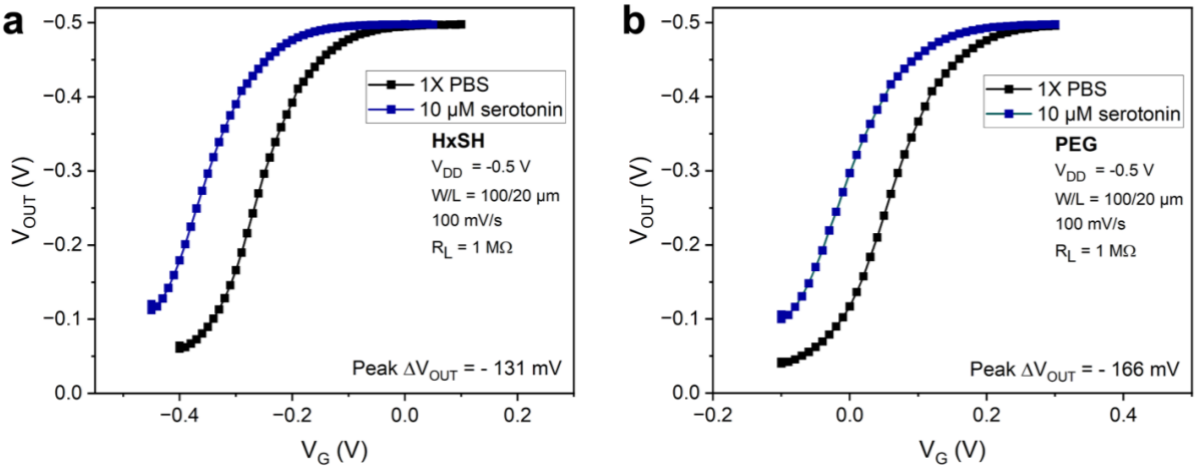

Figure D.3. HxSH and PEG FGTs response to 10 µM serotonin. Additional controls where FG2 is functionalized only with (a) 1-hexanethiol and (b) PEG thiol shift to a more negative V_G from before (black) to after (blue) 10 µM serotonin dosing over 5 min. The average signal over 5 min for each device was –131 mV and –166 mV, respectively. Inverter curves are of the backward sweep.

Appendix E – Electrochemical Stability of 11-MUA and Antibody-Conjugated Electrodes

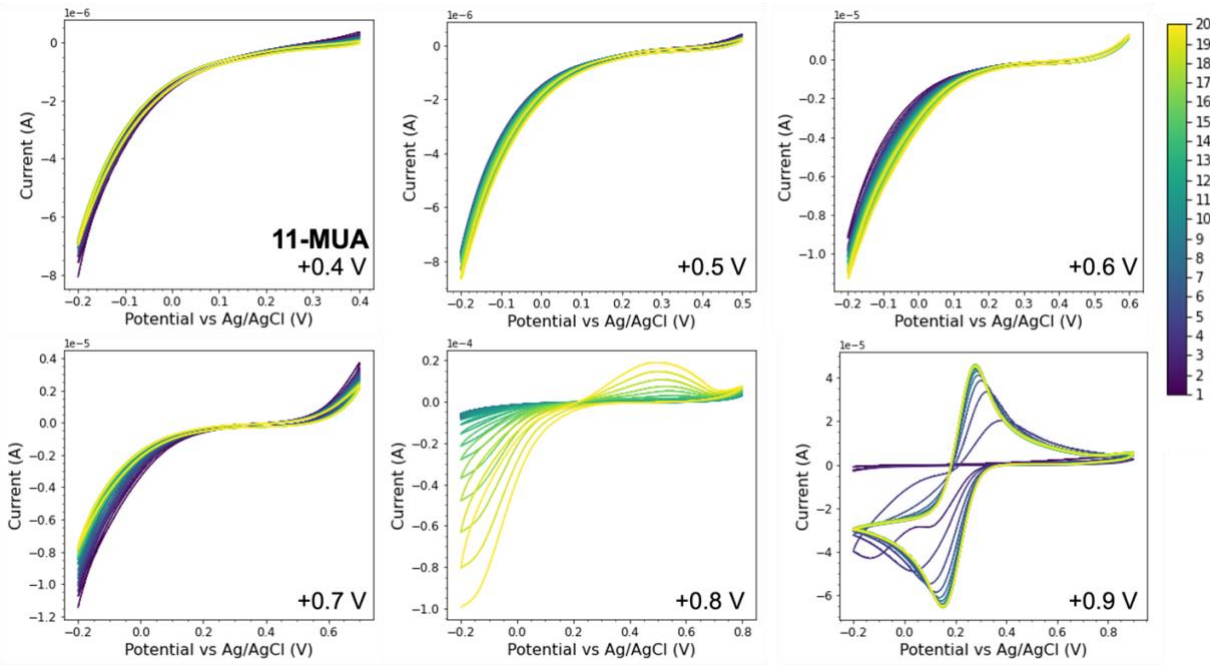

Figure E.1. Electrochemical stability of 11-MUA functionalized gold electrodes with varying positive potentials. The electrolyte was 1X PBS, the redox reporter was 10 mM $[Fe(CN)_6]^{3-/4-}$, and the sweep rate was 25 mV/s. All starting potentials were –0.2 V with end potentials in the inset. The color bar indicates the sweep number. All potential windows used the same sample until +0.8 V. A new sample was used for +0.9 V.

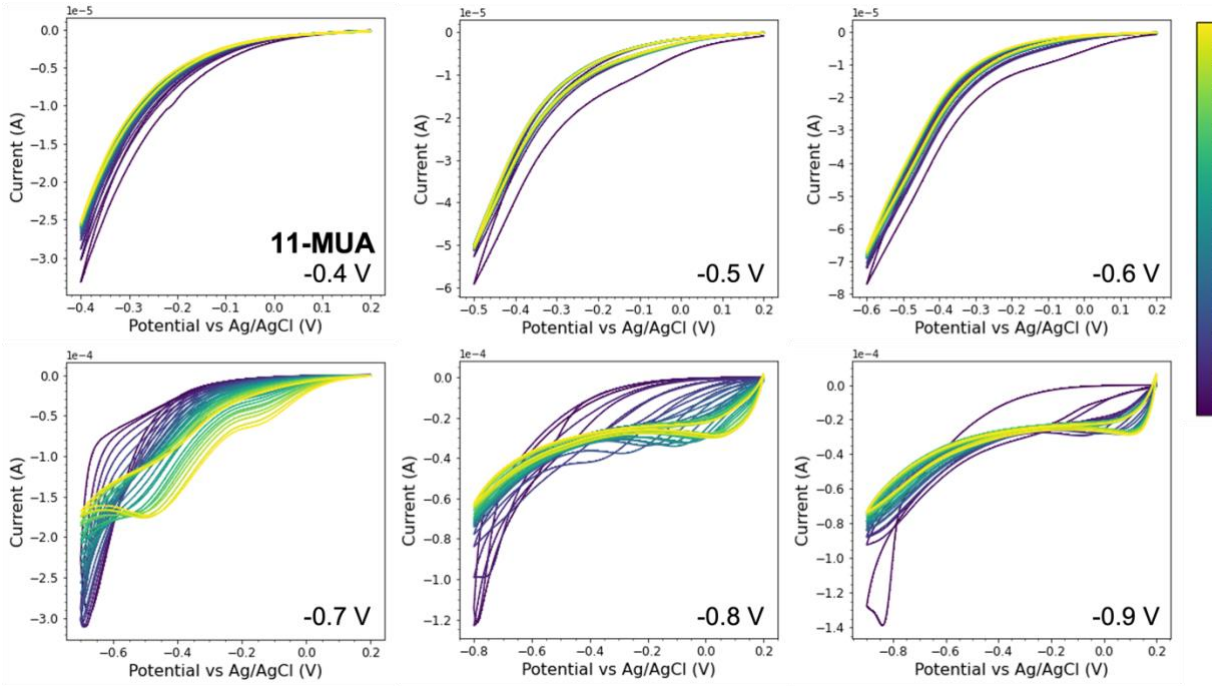

Figure E.2. Electrochemical stability of 11-MUA functionalized gold electrodes with varying negative potentials. The electrolyte was 1X PBS, the redox reporter was 10 mM $[Fe(CN)_6]^{3-/4-}$, and the sweep rate was 25 mV/s. All starting potentials were +0.2 V with end potentials in the inset. The color bar indicates the sweep number. All potential windows use the same sample until –0.7 V. New samples are used for –0.8 V and –0.9 V.

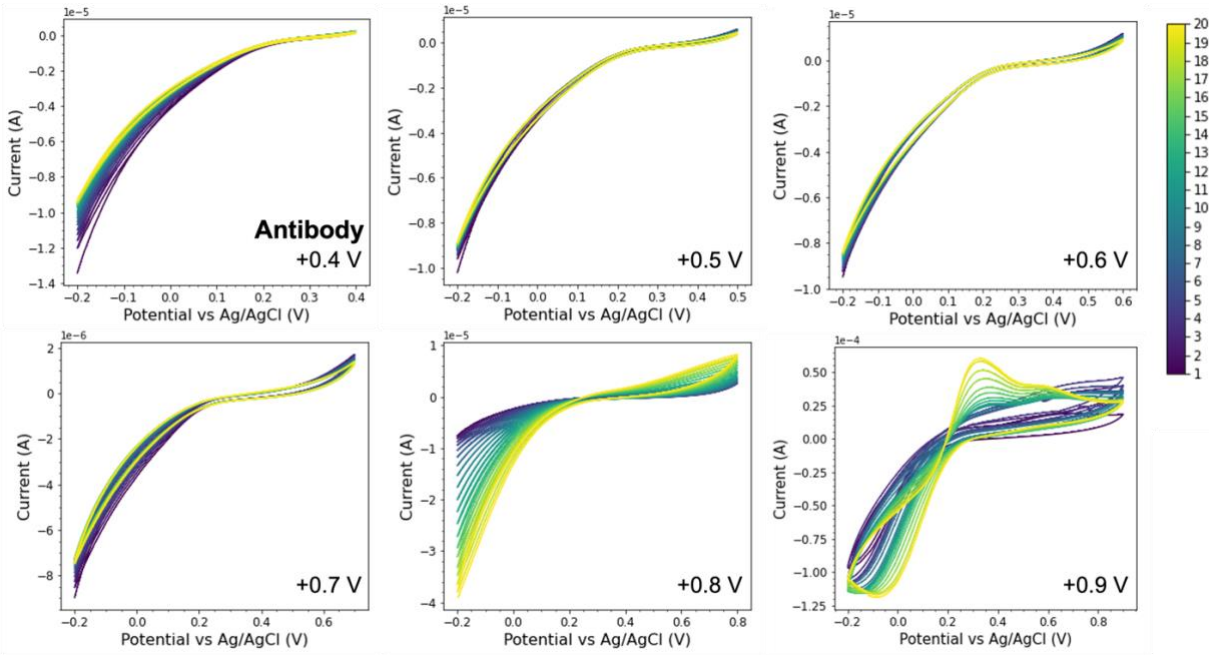

Figure E.3. Electrochemical stability of antibody-functionalized gold electrodes with varying positive potentials. The electrolyte was 1X PBS, the redox reporter was 10 mM $[Fe(CN)_6]^{3-/4-}$, and the sweep rate was 25 mV/s. All starting potentials were –0.2 V with end potentials in the inset. The color bar indicates the sweep number. One sample was used for all potential windows.

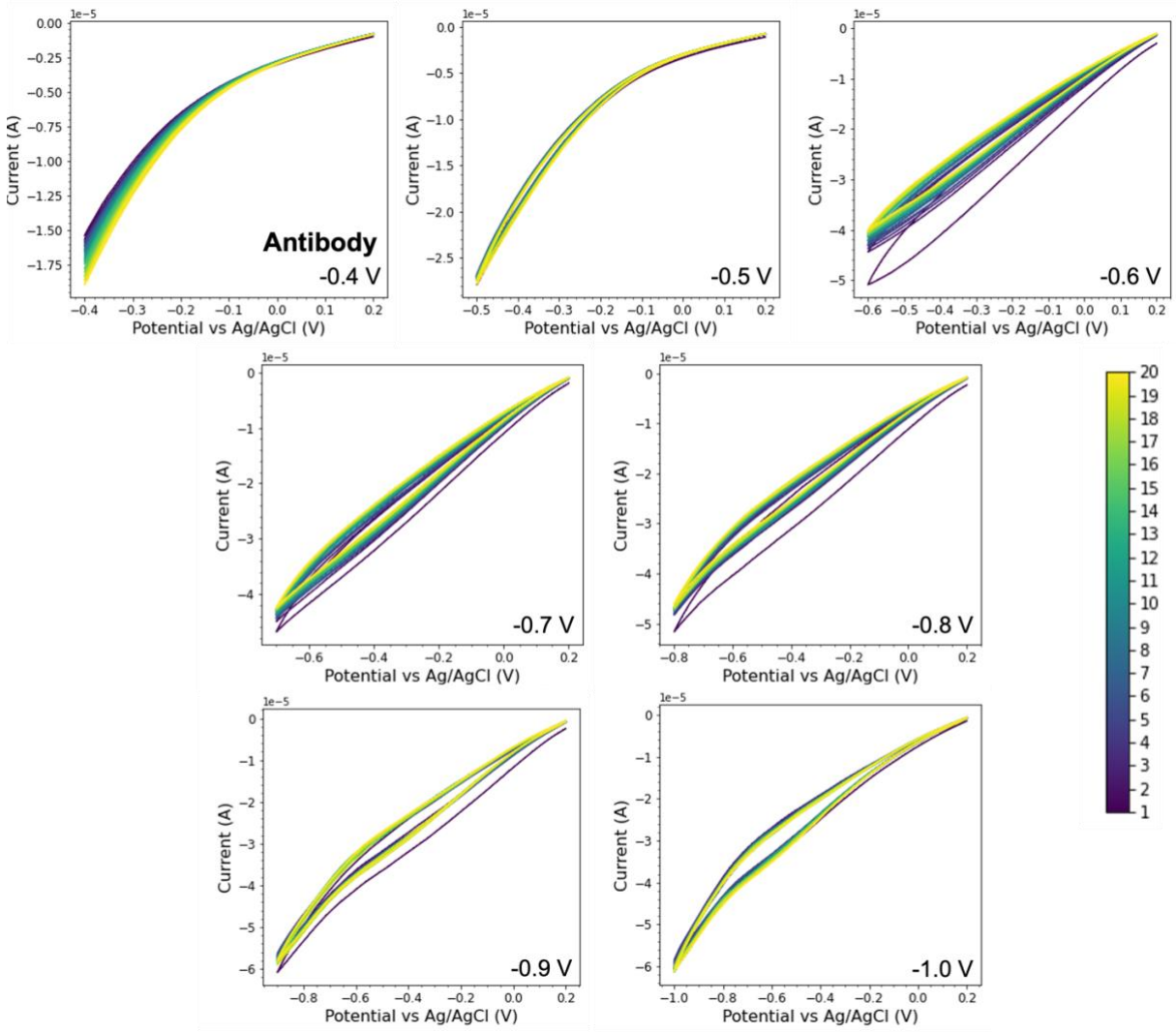

Figure E.4. Electrochemical stability of antibody-functionalized gold electrodes with varying negative potentials. The electrolyte was 1X PBS, the redox reporter was 10 mM $[Fe(CN)_6]^{3-/4-}$, and the sweep rate was 25 mV/s. All starting potentials were +0.2 V with end potentials in the inset. The color bar indicates the sweep number. One sample was used for all potential windows.